

712 | September 2019

**SCHRIFTENREIHE SCHIFFBAU**

Svenja Schubert

**Analysis of Coupling Techniques for  
Overset-Grid Finite-Volume Methods**

**TUHH**

*Technische Universität Hamburg*

# **Analysis of Coupling Techniques for Overset-Grid Finite-Volume Methods**

Vom Promotionsausschuss der  
Technischen Universität Hamburg  
zur Erlangung des akademischen Grades

Doktor-Ingenieurin (Dr.-Ing.)

genehmigte Dissertation

von  
Svenja Schubert  
aus Hamburg

2019

**Gutachter:**

1. Gutachter: Prof. Dr.-Ing. Thomas Rung
2. Gutachter: Prof. Ph.D. Rainald Löhner

**Tag der mündlichen Prüfung:**

09. Juli 2019

**Vorsitzender des Prüfungsausschusses:**

Prof. Dr.-Ing. Otto von Estorff

© Technische Universität Hamburg  
Schriftenreihe Schiffbau  
Am Schwarzenberg-Campus 4 (C)  
21073 Hamburg

<https://www.tuhh.de/vss>

Bericht Nr. 712  
ISBN 978-3-89220-712-2

# Abstract

This thesis addresses coupling techniques for overset-grid finite-volume methods focussing on non-conservative inter-grid coupling effects and a dynamic body contact. The first challenge arises from using an overset-grid approach when simulating incompressible flows with a cell-centred finite-volume solver. The coupling approach for unstructured three-dimensional grids is usually based on a local interpolation of field values, which is insufficient to guarantee that the global sum of the mass fluxes across the overlapping interfaces vanishes. Since incompressible finite-volume solvers directly use the mass defect when solving for the pressure, severe pressure fluctuations may be provoked by the violation of the inherent mass conservation. The conducted sensitivity study of the residual mass defect on overlapping grids and the related pressure fluctuations reveals that especially transient flows and simulations with relative grid motion are subject to significant mass and pressure fluctuations. High-order interpolation and grid refinement prove beneficial, but can still be afflicted with severe disturbances, particularly when the resolution properties of the overlapping grids differ. Two-phase flows with a high density ratio show a distinct compensating behaviour, while the introduction of mass conservation practices leads to notable improvements for single-phase flows in homogeneous as well as heterogeneous resolution conditions.

The second topic of the thesis reports on modifications to the overset-grid coupling strategy for the simulation of fluid flow around moving bodies in direct proximity. The interpolation-based grid coupling of overlapping grids requires a sufficient overlap of the wetted domain for the interpolation of field values, which is not ensured for bodies in direct proximity or even in contact. The suggested modification is based upon three steps embedded into the existing overset-grid procedure, i.e. a detection of critical coupling areas, a subsequent introduction of artificial boundary conditions to substitute unresolved coupling issues and a simple module to account for the mechanical contact of rigid bodies. The complete procedure is verified and successfully applied to the simulation of a landslide and the numerical examination of an external gear pump including gear contact, where zero-gap capabilities are essential to model the flow.

A final analysis of the thesis refers to the hydrodynamic interplay of rigid bodies in direct proximity. The examples included are confined to contact simulations between a circular cylinder and a sphere with a plane external wall. The results reveal a significant increase of the additional inertia and resistance forces when reducing the distance to the wall and indicate that the proximity influence on the added mass and added resistance is coupled. While previous studies in literature have not been able to capture the observed high-order influences, the derived formulae provide simple corrections of the baseline values that can easily be transferred to wetted structural simulations.



# Acknowledgements

I am very grateful to everyone who accompanied me throughout the last few years. My research work at the Institute for Fluid Dynamics and Ship Theory at the Hamburg University of Technology was characterised by many challenging ups and downs. Thanks to your support and company, I was able to get through all of them not only successfully but also having a great time.

I would like to express my sincere gratitude to my supervisor Prof. Dr.-Ing. Thomas Rung. He provided the opportunity to join his research group and supported my research with many ideas, lots of valuable feedback and an infectious enthusiasm. I also thank Prof. Phd Rainald Löhner for the review and the interest in this thesis as well as Prof. Dr.-Ing. Otto von Estorff for chairing the examination board.

I would like to express my appreciation to my colleagues at deck five. Especially, I thank my two office mates for the great time. I gladly remember the jovial, but also productive, atmosphere with Dr.-Ing. Christian Janßen. I would like to thank Torben Mühlbach, with whom I shared not only the office, but also a research project, for the numerous, pleasant hours we spent together. I had a good time programming and evaluating with him and I also enjoyed our off-topic chats during the Frescolino-breaks. I thank Niklas Kühl for the fruitful exchange about (computational) fluid dynamics and the numerical implementation within FreSCo<sup>+</sup>. I have greatly benefited from Dr.-Ing. Jörn Kröger who shared lots of tips and tricks from his research experience.

Special thanks go to Dieke Hafermann with whom I spent a lot of time (partly on the telephone) discussing possible implementation strategies, parallelising the code, looking for bugs and also sharing excitement about new features.

Last but not least, I would like to thank my friends and my family. I am particularly thankful to Dr.-Ing. Evelyn Heins for proofreading this thesis. My mother Conny has been extraordinary supportive during the finalisation of this thesis by taking care of my son Vincent from time to time. Finally, I feel deeply grateful to my husband Lars for all the support, the encouragement and his never-ending patience.



# Contents

|   |            |
|---|------------|
| <b>Abstract</b>   | <b>ii</b>  |
| <b>Acknowledgements</b>   | <b>iii</b> |
| <b>Nomenclature</b>   | <b>ix</b>  |
| <b>1 Introduction</b>   | <b>1</b>   |
| 1.1 Background and Motivation . . . . .                               | 1          |
| 1.2 Previous Related Studies . . . . .                                | 3          |
| 1.2.1 Conservative Inter-Grid Coupling . . . . .                      | 3          |
| 1.2.2 Dynamic Body Contact . . . . .                                  | 4          |
| 1.3 Starting Point and Goals of the Thesis . . . . .                  | 5          |
| 1.4 Present Contributions . . . . .                                   | 5          |
| 1.5 Outline of the Thesis . . . . .                                   | 6          |
| <b>2 Mathematical Model</b>   | <b>7</b>   |
| 2.1 Governing Equations . . . . .                                     | 7          |
| 2.1.1 Generic Transport Equation . . . . .                            | 7          |
| 2.1.2 Navier-Stokes Equations . . . . .                               | 8          |
| 2.1.3 Two-Phase Flow . . . . .  | 9          |
| 2.1.4 Turbulence Capturing . . . . .                                  | 10         |
| 2.1.5 Initial and Boundary Conditions . . . . .                       | 12         |
| 2.2 Finite-Volume Method . . . . .                                    | 13         |
| 2.2.1 Spatial Integrals . . . . .                                     | 14         |
| 2.2.2 Time Derivatives . . . . .                                      | 15         |
| 2.2.3 Determination of Gradients . . . . .                            | 15         |
| 2.2.4 Reconstruction of Face Values . . . . .                         | 16         |
| 2.2.5 Boundary Conditions . . . . .                                   | 19         |
| 2.3 Numerical Procedure . . . . .                                     | 20         |
| <b>3 Overset-Grid Approach</b>  | <b>23</b>  |
| 3.1 Interpolation Algorithms & Baseline Inter-Grid Coupling . . . . . | 23         |
| 3.2 Mass Conservation Practices . . . . .                             | 26         |
| 3.2.1 Volume Correction Approach . . . . .                            | 26         |
| 3.2.2 Flux Correction Approaches . . . . .                            | 27         |
| 3.3 Inter-Grid Coupling for Dynamic Body Contact . . . . .            | 28         |
| 3.3.1 Detection of Critical Areas . . . . .                           | 29         |
| 3.3.2 Artificial Boundary Conditions . . . . .                        | 30         |
| 3.3.3 Collision of Rigid Bodies . . . . .                             | 31         |

|          |   |            |
|----------|---|------------|
| <b>4</b> | <b>Analysis of Non-Conservative Inter-Grid Coupling Effects</b> | <b>33</b>  |
| 4.1      | Verification and Validation for Steady-State Flows . . . . .    | 33         |
| 4.1.1    | DFG Benchmark Case . . . . .                                    | 33         |
| 4.1.2    | Lid-Driven Cavity Case . . . . .                                | 39         |
| 4.2      | Transient Flow Studies . . . . .                                | 41         |
| 4.2.1    | Pitching Hydrofoil . . . . .                                    | 42         |
| 4.2.2    | Body-Force Disturbed Channel Flow . . . . .                     | 53         |
| 4.2.3    | Moving Lid-Driven Cavity Case . . . . .                         | 54         |
| 4.3      | Summary . . . . .   | 56         |
| <b>5</b> | <b>Verification and Application of the Dynamic Body Contact</b> | <b>57</b>  |
| 5.1      | Verification of Artificial Boundary Conditions . . . . .        | 57         |
| 5.2      | Verification of the Collision Procedure . . . . .               | 59         |
| 5.3      | External Gear Pump . . . . .                                    | 64         |
| 5.4      | Sliding Wedge . . . . .   | 70         |
| 5.5      | Summary . . . . .   | 72         |
| <b>6</b> | <b>Hydrodynamic Wall-Interference Effects</b>                   | <b>75</b>  |
| 6.1      | Formulation of the Problem . . . . .                            | 75         |
| 6.2      | Wall Influence on Hydrodynamic Forces . . . . .                 | 76         |
| 6.2.1    | Acceleration Force and Added Mass . . . . .                     | 76         |
| 6.2.2    | Resistance Force and Added Resistance . . . . .                 | 78         |
| 6.2.3    | Wall Influence Identification Procedure . . . . .               | 82         |
| 6.3      | Preliminary Studies . . . . .                                   | 82         |
| 6.3.1    | Computational Setup . . . . .                                   | 83         |
| 6.3.2    | Sensitivity Study for Unconfined Flow . . . . .                 | 84         |
| 6.3.3    | Baseline Resistance . . . . .                                   | 86         |
| 6.4      | Wall Influence on a Cylinder . . . . .                          | 87         |
| 6.4.1    | Additional Resistance . . . . .                                 | 88         |
| 6.4.2    | Added Mass . . . . .  | 94         |
| 6.5      | Wall Influence on a Sphere . . . . .                            | 96         |
| 6.5.1    | Additional Resistance . . . . .                                 | 98         |
| 6.5.2    | Added Mass . . . . .  | 99         |
| 6.6      | Summary . . . . .   | 102        |
| <b>7</b> | <b>Conclusions</b>  | <b>105</b> |
|          | <b>Bibliography</b>   | <b>107</b> |

# Nomenclature

In this thesis, vectors and tensors are defined by reference to Cartesian coordinates. Einstein's summation is used over the repeated lower-case Latin indices  $i$ ,  $j$  and  $k$  only, which mark Cartesian tensor coordinates. For readability, indices, special variables or constant model parameters, which just occur once, are not listed within the nomenclature.

## Lower-case Latin

|  |  |
|--|--|
| $a_i$  | Acceleration vector  |
| $c$  | Concentration  |
| $c_A, c_D, c_L, c_p$                                 | Added mass / Drag / Lift / Pressure coefficient            |
| $d_i, d$   | Distance vector / norm                                     |
| $e$  | Collision number   |
| $f$  | Frequency  |
| $f_i$  | Volume-specific force vector                               |
| $g$  | Gravity acceleration constant                              |
| $h$  | Wall-normal distance                                       |
| $k$  | Turbulent kinetic energy                                   |
| $l$  | Control variable   |
| $m$  | Mass   |
| $\dot{m}$  | Mass flux  |
| $m_A, m_{\mathcal{F}}$                               | Added / Displaced mass                                     |
| $n_{\mathcal{D}}, n_{\mathcal{F}}, n_{C_A}, n_{C_S}$ | Number of donor cells / faces / active cells / solve cells |
| $n_i, n$   | Normal vector / direction                                  |
| $p$  | Pressure   |
| $p', p^*$  | Pressure correction / initial value                        |
| $q_\phi$   | Volume-specific source                                     |
| $s_{ij}$   | Strain-rate tensor   |
| $t$  | Time   |
| $t_i$  | Tangent vector   |

|                 |  |
|-----------------|--|
| $u_i$           | Fluid velocity vector                              |
| $\tilde{u}_i$   | Fluid velocity vector relative to a control volume |
| $\dot{v}$       | Volume flux  |
| $v_i$           | Body velocity vector                               |
| $w$             | Weight   |
| $x_i (x, y, z)$ | Cartesian coordinates                              |

### Upper-case Latin

|               |   |
|---------------|---|
| $B$           | Edge length   |
| $Co$          | Courant number                                      |
| $D$           | Diameter / Depth                                    |
| $E_{kin}$     | Kinetic energy                                      |
| $F_i$         | Force vector  |
| $F_{A_i}$     | Acceleration dependent force vector                 |
| $F_{H_i}$     | Hydrostatic force vector                            |
| $F_{V_i}$     | Resistance force vector                             |
| $F_{V_i}^0$   | Baseline resistance force vector in unconfined flow |
| $Fn$          | Froude number                                       |
| $H$           | Height  |
| $L$           | Length  |
| $\mathcal{M}$ | Mass defect parameter                               |
| $P$           | Turbulent production rate                           |
| $\mathcal{P}$ | Pressure defect parameter                           |
| $Q$           | Flow rate   |
| $Q_T$         | Theoretical flow rate                               |
| $R$           | Radius  |
| $Re$          | Reynolds number                                     |
| $S_i, S$      | Surface vector / area                               |
| $St$          | Stokes number                                       |
| $T_G$         | Gearing period                                      |
| $V, \bar{V}$  | Computational domain, Observed volume               |
| $W$           | Width   |
| $W(\delta^*)$ | Wall correction function                            |

### Lower-case Greek

|                  |                             |
|------------------|-----------------------------|
| $\alpha$         | Angle                       |
| $\dot{\alpha}$   | Angular velocity            |
| $\delta\dot{m}$  | Mass flux correction        |
| $\delta$         | Explicit coupling parameter |
| $\delta^*$       | Interstitial gap            |
| $\delta_{ij}$    | Identity tensor             |
| $\epsilon$       | Turbulent dissipation       |
| $\epsilon_{ijk}$ | Levi-Civita-Symbol          |
| $\eta$           | Surface elevation           |
| $\mu, \mu_t$     | Dynamic / Eddy viscosity    |
| $\omega$         | Specific dissipation rate   |
| $\phi$           | Generic variable            |
| $\rho$           | Density                     |
| $\tau_{ij}$      | Stress tensor               |

### Upper-case Greek

|                        |  |
|------------------------|--|
| $\Delta A$             | Cell area  |
| $\Delta F_{V_i}$       | Additional resistance force vector in wall-proximity |
| $\Delta S_i, \Delta S$ | Face vector / area                                   |
| $\Delta V$             | Control volume                                       |
| $\Delta \dot{M}_O$     | Mass defect of the overset-grid approach             |
| $\Delta c_D$           | Added drag coefficient                               |
| $\Delta t$             | Time step  |
| $\Delta x$             | Cell edge length                                     |
| $\Delta z$             | Vertical distance                                    |
| $\Gamma$               | Diffusion coefficient                                |

### Subscripts

|               |            |
|---------------|------------|
| $\mathcal{B}$ | Body       |
| $Bd$          | Boundary   |
| $\mathcal{D}$ | Donor cell |

|                     |   |
|---------------------|---|
| $F$                 | Face centre                                     |
| $F'$                | Piercing point                                  |
| $\mathcal{F}$       | Fluid   |
| $I$                 | Interpolation cell                              |
| $L, R$              | Interfering bodies                              |
| $P, N_f$            | Observed cell centre and neighbour cell centres |
| $P_A, P_{DA}$       | Centre of the active and the deactivated cell   |
| $\beta, \gamma$     | Control variables                               |
| $a, w$              | Air, Water                                      |
| $c, m, f, vf$       | Coarse, Medium, Fine, Very fine                 |
| $i, j, k / x, y, z$ | Cartesian coordinates                           |
| init                | Initial conditions                              |
| limit               | Threshold value                                 |
| max                 | Maximum value                                   |
| ref                 | Reference conditions                            |

### Superscripts

|                    |                       |
|--------------------|-----------------------|
| $(0)$              | Initial conditions    |
| $(n)$              | Current time level    |
| $(n - 1), (n - 2)$ | Previous time levels  |
| $(s)$              | Slip wall conditions  |
| $(t)$              | Turbulent flow        |
| $T$                | Turbulent fluctuation |

### Symbols & Operations

|                      |                |
|----------------------|----------------|
| $\overline{(\cdot)}$ | Mean value     |
| $ \cdot $            | Absolute value |
| $\ \cdot\ $          | Euclidean norm |

### Abbreviations

|            |                               |
|------------|-------------------------------|
| 1D, 2D, 3D | One-, Two-, Three-Dimensional |
| 6DoF       | Six Degrees of Freedom        |
| ALE        | Arbitrary Lagrangian-Eulerian |

|                     |   |
|---------------------|---|
| BiCG                | Biconjugate Gradient  |
| CDS                 | Central-Differencing Scheme                                 |
| CFD                 | Computational Fluid Dynamics                                |
| CICSAM              | Compressive Interface Capturing Scheme for Arbitrary Meshes |
| DNS                 | Direct Numerical Simulation                                 |
| EoS                 | Equation of State   |
| FreSCo <sup>+</sup> | Free Surface Code (in-house RANS solver)                    |
| H.o.                | High order  |
| HRIC                | High-Resolution Interface Capturing                         |
| IB                  | Immersed Boundary   |
| L.o.                | Low order   |
| LES                 | Large Eddy Simulation                                       |
| MPI                 | Message Passing Interface                                   |
| MUSCL               | Monotonic Upwind Scheme for Conservation Laws               |
| QUICK               | Quadratic Upstream Interpolation of Convective Kinematics   |
| RANS                | Reynolds-Averaged Navier-Stokes                             |
| RSM                 | Reynolds Stress Equation Model                              |
| SIMPLE              | Semi-Implicit Method for Pressure-Linked Equations          |
| SST                 | Shear Stress Transport                                      |
| UDS                 | Upwind-Differencing Scheme                                  |
| VoF                 | Volume-of-Fluid   |



# 1 Introduction

## 1.1 Background and Motivation

Multi-body hydrodynamics featuring mutual interaction and contact between rigid or flexible floating bodies is an active area of research for complex marine engineering devices. An example refers to offshore supply vessels, where it is important to consider operations in close proximity of other vessels or structures, e.g. the landing manoeuvre of the vessel at an offshore foundation (Luo-Theilen and Rung 2017). Other examples, which are subject to significant hydrodynamic interaction forces, are the simulation of ship collisions (Rudan and Volarić 2016) and the collision between ice floes and an ice-cruising vessel (Janßen et al. 2017).

Particularly due to safety reasons, it is essential to know and to understand the flow field around moving bodies, the arising hydrodynamic forces and the resulting body behaviour within decisive marine operations already in the design process. While not all aspects can be captured economically within analytical or experimental examinations, numerical simulations are meanwhile established as a reliable design tool. Due to the continuous technological progress of numerical hard- and software, computational fluid dynamics (CFD) nowadays provides the opportunity to investigate complex marine procedures prior to critical incidences. Especially viscous CFD methods give an extensive insight into the occurring physical phenomena. Industrial viscous flow simulations often follow a finite-volume approach. However, fluid dynamic simulations of multiple floating bodies, which feature large relative motion, are still challenging using these grid-based Eulerian methods. In this regard, overset-grid methods offer a versatile approach. They simplify the grid generation by using modular grid components and at the same time often improve the grid quality. The technique comes at the expense of (a) an elaborate priority management and cell blanking for regions covered by multiple grids, (b) a challenging interpolation-based coupling between disjunct grids and (c) complex dynamic load balancing efforts for parallel applications. All these algorithmic challenges require efficient search algorithms used to manage the grid connectivity (Hadžić 2006, Löhner 2008, Brunswig and Rung 2013).

Many industrial CFD applications are based on unstructured-grid finite-volume methods and employ a co-located, cell-centred variable arrangement. A common implicit approach to couple multiple unstructured three-dimensional grids in a cell-centred scheme is to interpolate neighbouring field values onto the partner grids, which creates an implicit link between the grids on the level of the equation system. Since an interpolation-based coupling procedure is restricted to local information, it is insufficient to guarantee that the global sum of the mass fluxes across the overlapping interfaces vanishes. A simple example refers to the exterior surface of a foreground

grid, which is fully embedded in the interior of a background grid, cf. the schematic representation on the left-hand side of Figure 1.1. The arrangement implies that the sum of the mass fluxes along the exterior boundary of the foreground grid must vanish, which cannot be guaranteed by an interpolation-based grid coupling without dedicated corrections. Consequently, such overset-grid approaches violate the inherent mass conservation of finite-volume methods. This issue is of significance for both the global mass balance of the entire simulation as well as the local balance of each domain. In this context, the blanked area within the background domain yields additional boundary fluxes (displayed on the right-hand side of Figure 1.1) which also contribute to the mass balance. Due to the fact that incompressible finite-volume methods directly use the mass defect when solving for the pressure, severe pressure fluctuations can be provoked.

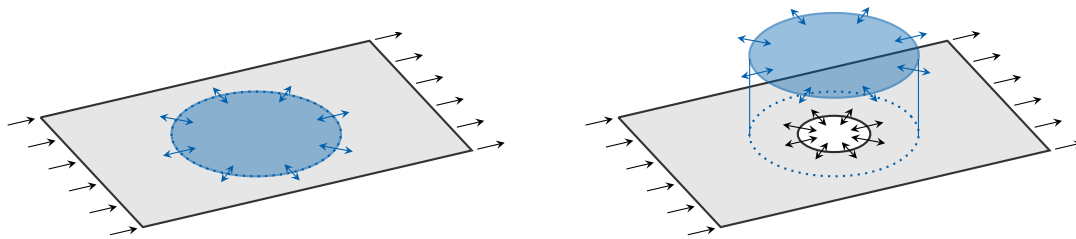


Figure 1.1: Schematic representation of the mass fluxes along the exterior boundaries of a fully embedded circular foreground domain (blue) and of the surrounding background channel domain (black) in an overset-grid arrangement. The blanked area within the background channel yields additional boundary fluxes (displayed on the right-hand side) which also contribute to the mass balance of the background domain.

Another challenge arises from the fact that the interpolation of field values requires a fair amount of overlap between fluid domains to couple the modular computational grids that comprise the respective bodies. The inter-grid coupling thus fails for bodies in close proximity or contact scenarios with an insufficient wetted gap. Procedural restrictions on a minimal gap are associated with an artificial enlargement of distances, resizing and repositioning of the computational model and/or a locally increased cell refinement. Moreover, the introduction of small gaps might lead to difficulties with the cell skewness, increase the computational effort and yields no solution for simulations with body contact. Overcoming the minimal-gap restriction is of interest in the field of fluid-structure interaction, e.g. gear simulations, ship collisions, valve studies or ship/ice-interaction.

The present research aims to deal with the primary challenges that arise from a cell based overset-grid coupling, e.g. non-conservative inter-grid coupling effects and a dynamic body contact. Expanding the capabilities of the overset-grid procedure provides the opportunity to study complex flow phenomena in the field of fluid-structure interaction. Within this context, proximity influences are of interest when investigating a body close to located obstacles, for example in ship collision scenarios. Associated structural investigations often regard the hydrodynamic effects by means of a constant factor

(aka. *added mass*) that mimics the effect of the surrounding fluid. This simplified concept does not consider the confining influence of multiple bodies or a free-surface, although spatial limits are frequently deemed responsible for a significant increase of the added mass (Brennen 1982, Clauss et al. 1988). Therefore, corrections of the baseline value are required if bodies collide or operate in close proximity. The essential investigation of proximity influences on the hydrodynamic forces using the enhanced overset-grid approach is a final aim of this thesis.

## 1.2 Previous Related Studies

A short overview of previously published numerical studies regarding the primary challenges of a conservative inter-grid coupling and a dynamic body contact is given by the following references.

### 1.2.1 Conservative Inter-Grid Coupling

Since the introduction of overset-grid methods in computational fluid dynamics (Atta 1981, Benek et al. 1983), many studies were performed to ensure mass conservation at the overlapping interfaces. Berger (1987) and Pärt-Enander and Sjögreen (1994) introduced the interpolation of fluxes at the grid interfaces for two-dimensional grids. Pärt-Enander and Sjögreen (1994) claimed that the procedure is only weakly stable and an additional filter is needed to remove oscillations. Moreover, this procedure is difficult to implement for unstructured three-dimensional grids and cannot be embedded implicitly in the equation system. Another idea was the implementation of patched grids (Wang 1995), where the basic requirement is the perfect match of the grid interfaces. Hence, the method is impractical for relative grid motion. Chesshire and Henshaw (1994) proposed to determine the interpolation coefficients of two-dimensional overlapping grids by defining constraints which ensure that the interpolation is conservative. Since this results in an additional equation system, which size increases with the overlapping area, the method is cumbersome for complex three-dimensional grids or relative grid motion. Only very few publications on conservative three-dimensional overset-grid methods are reported in the literature. Tang et al. (2003) suggested to implement a conservative interpolation of velocity components with a reconstruction of the mass flux. The huge drawback is that the approach satisfies mass conservation exactly only for zero inter-grid spacing, which is again problematic for relative grid motion. Several other studies stated satisfactory results with non-conservative methods, but they relied on patched grids (Freitas and Runnels 1999), compressible flows (Nakahashi et al. 2000, Basso and Azevedo 2004) or two-phase flows on structured grids (Chung et al. 2007, Carrica et al. 2013). Hadžić (2006) accentuated the importance of mass conservation for the pressure prediction when dealing with incompressible flows. Though he did not explicitly report on non-conservative effects, he was the first to suggest an explicit flux correction at the overlapping interfaces and validated the approach for incompressible single-phase flows on unstructured two-dimensional grids. Still, there exists no detailed

analysis of the effects of a non-conservative grid coupling using an incompressible unstructured-grid finite-volume solver.

### 1.2.2 Dynamic Body Contact

Dynamic contact of wetted bodies is frequently avoided in CFD applications, e.g. by introducing a small additional gap (Strasser 2007, Kim et al. 2007). Kim et al. (2007) analysed the influence of different gap sizes between the gears of an external gear pump and stated an improved agreement with the pump manufacturer's data for a diminishing gap size. Luo-Theilen and Rung (2017) implemented a fender model composed from virtual non-linear springs and dampers to prevent body contact while analysing the hydrodynamic effects during the landing manoeuvre of a catamaran vessel and an offshore foundation. The resulting gap flow between the ship and the offshore structure was proved to be realistic, though for some applications it is essential to model body contact, e.g. the numerical examination of a gear pump, valve studies or ship collision scenarios. Castilla et al. (2010) investigated an external gear pump and depicted large discrepancies between the flow rates computed with and without gear contact. The importance of closing the gap is emphasised and either a small additional wall (Castilla et al. 2010) or an enhanced viscosity between both gears (Del Campo et al. 2012, Castilla et al. 2015) is introduced. The geometry modification was cumbersome captured by a mesh deformation strategy in combination with a periodic mesh replacement method to avoid distorted cells. Immersed boundary approaches or marker and cell methods assign bodies within the fluid domain by marking specific grid points as solid (Robinson-Mosher et al. 2011) and thereby provide an appropriate strategy for fluid-structure interaction simulations (Qiu et al. 2015, Yoon et al. 2017, Janßen et al. 2017). While the procedures simplify the implementation of bodies in contact, challenges arise for bodies in direct proximity, e.g. the reconstruction of boundary conditions and a sudden closure of the fluid grid cells within lubricated gaps. Another challenging aspect for all strategies refers to the reactivation of previously deactivated discrete fluid regions, for instance after a collision. The latter has been handled by Qiu et al. (2015), who introduced additional pressure degrees of freedom on the solid boundaries of two interacting bodies to provide forces within thin gaps or for bodies in contact. Overset-grid methods provide a well-working grid update strategy for multi-body hydrodynamics featuring large relative motion. To overcome the minimal-gap restriction of overlapping grids, Noack et al. (2009) presented an algorithmic cell mark procedure for the identification of coupling problems and notices a subsequent manipulation via immersed boundary methods. Recent publications by Berton et al. (2017) and Al-Azawy et al. (2017) who performed valve studies using commercial CFD codes, allow to seal the valves in their closed position (aka. *zero-gap method*). A simple inter-grid coupling procedure for dynamic body contact has still not been published, although the fluid flow could simply be blocked by no-flux conditions (aka. *artificial boundary conditions*).

## 1.3 Starting Point and Goals of the Thesis

The aim of this thesis is to analyse and enhance the coupling techniques of overset-grid finite-volume methods regarding the primary challenges of a conservative inter-grid coupling and a dynamic body contact.

The finite-volume Navier-Stokes procedure FreSCo<sup>+</sup> (Rung et al. 2009) is employed within this thesis. The work is based on the overset-grid procedure by Brunswig and Rung (2011), which applies a local interpolation of cell-centred field values onto fully unstructured partner grids as coupling procedure. The research within the present thesis is devoted to the following topics:

- Analysis of non-conservative inter-grid coupling effects.
- Development of an inter-grid coupling strategy for bodies in direct proximity.
- Analysis of hydrodynamic wall-interference effects.

## 1.4 Present Contributions

Considering the described goals, the thesis comprises the following contributions to the coupling techniques of overset-grid finite-volume methods:

- The effects of a non-conservative inter-grid coupling are analysed considering that incompressible finite-volume methods are based on a direct link between mass defect and pressure, since the pressure is adapted to compensate mass imbalances within the flow field. Hence, a non-conservative inter-grid coupling can result in severe pressure fluctuations. The examination includes the following aspects:
  - The accuracy of the baseline overset approach is proved by comparison with literature reported and/or single-grid results.
  - Universal global mass conservation practices are formulated to prevent that erroneous fluxes across the overlapping interfaces provoke pressure fluctuations.
  - Means to improve the local accuracy within the mass conservation practices are investigated.
  - A sensitivity study of the residual mass defect on overlapping grids and the related pressure fluctuations is performed for a variety of coupling strategies and mass conservation practices. Emphasis is put on transient influences, the resolution quality of the overlapping grids and multiphase-flow issues.
- An inter-grid coupling for bodies in close proximity is developed to overcome the requirement of a fair amount of overlap, i.e. a minimal wetted gap between the bodies. Specific measures are:
  - Critical cells in the vicinity of the contact zone are dynamically identified in the grid coupling algorithm.

- The computational model is manipulated for the identified contact cells if no valid coupling can be achieved by reducing the interpolation order. Unresolved coupling issues are substituted by a closure of the fluxes affecting the active simulation domain (aka. *artificial boundary conditions*).
- A simple collision procedure is applied to prohibit the penetration of floating bodies.
- The artificial boundary approach and the collision module are verified. Applications refer to the simulation of an external gear box and a generic landslide.
- The enhanced overset-grid approach is used to analyse proximity influences on hydrodynamic forces. The focus is on the additional resistance and inertia forces for a circular cylinder and a sphere approaching a plane wall. The investigation is summarised as follows:
  - Existing suggestions for hydrodynamic force corrections due to walls of nearby located obstacles are outlined. Supplementary to the traditional added mass modification in the vicinity of nearby located bodies, the study reveals significant changes of the resistance force. A link between additional resistance and inertia forces that facilitates their joint derivation is highlighted.
  - The reliability of the computational approach is assured for the determination of additional resistance and inertia forces.
  - Baseline data with respect to the forces in unconfined flow situations are provided.
  - The proximity influence on a circular cylinder and a sphere approaching a plane wall is analysed using numerical and analytical approaches.

## 1.5 Outline of the Thesis

This thesis begins with an introduction to the employed mathematical model, including the governing equations, the numerics of the finite-volume method and an overview of the solution procedure in Chapter 2. Chapter 3 is devoted to coupling techniques of the overset-grid approach. The detailed description refers to the applied interpolation algorithms, provides mass conservation practices and presents an inter-grid coupling strategy for bodies featuring dynamic contact. The analysis of non-conservative inter-grid coupling effects is presented in Chapter 4. Chapter 5 aims to prove the inter-grid coupling for bodies in direct proximity and presents the simulation of an external gear pump and a landslide as related applications. Chapter 6 employs the enhanced overset-grid approach to analyse hydrodynamic wall-interference effects, e.g. proximity influences on the hydrodynamic forces for a circular cylinder and a sphere approaching a plane wall. Final conclusions are drawn in Chapter 7.

## 2 Mathematical Model

Within this thesis, the flow field analysis of Newtonian fluids is addressed by solving conservation equations for properties such as mass, momentum, concentration and turbulent quantities. The Arbitrary Lagrangian-Eulerian (ALE) formulation provides a convenient solution for the observation of continuous media (such as fluid flows) since it describes the medium within spatial control volumes, but allows for relative motion of the observed domain. The numerical implementation follows a finite-volume method, which is inherently conservative and consistent with the ALE formulation. The conservation equations are consequently written in their conservative ALE integral form, which follows from the Reynolds' transport theorem (White 1994).

The first part of this chapter is devoted to an overview of the required governing equations, including the mandatory initial and boundary conditions. Following, the finite-volume method is introduced, comprising the domain discretisation, necessary approximation techniques and specific aspects of the employed boundary conditions. This chapter closes with an introduction to the Navier-Stokes procedure FreSCo<sup>+</sup>, which is applied in the present study.

### 2.1 Governing Equations

The fluid flow is governed by the Navier-Stokes equations supplemented by auxiliary transport equations to capture the distribution of multiple immiscible fluid phases and to model turbulence. The conservation equations describe the transport of the investigated flow properties and are deduced from a generic transport equation.

#### 2.1.1 Generic Transport Equation

The generic transport equation describes the transport of a generic field variable  $\phi$  and demands that the sum of the time variation within an observed volume  $\bar{V}$  and the convective fluxes across the volume surface  $S(\bar{V})$  is equivalent to the sum of the diffusive fluxes across the surface and the external sources:

$$\underbrace{\frac{\partial}{\partial t} \int_{\bar{V}} (\rho\phi) d\bar{V}}_{\text{Time variation}} + \underbrace{\oint_{S(\bar{V})} (\rho\phi\tilde{u}_j) dS_j}_{\text{Convection}} = \underbrace{\oint_{S(\bar{V})} \left( \Gamma \frac{\partial\phi}{\partial x_j} \right) dS_j}_{\text{Diffusion}} + \underbrace{\int_{\bar{V}} q_\phi d\bar{V}}_{\text{Source}}. \quad (2.1)$$

Here,  $t$  denotes the time,  $\rho$  the density,  $\Gamma$  the diffusion coefficient and  $q_\phi$  the volume-specific sources. The entries of the velocity vector read  $u_j$ , while  $\tilde{u}_j = u_j - u_{j,\bar{V}}$  marks the entries of the velocity vector relative to the control volume.  $x_j$  refers to the Cartesian coordinates and  $S_j$  to the entries of the surface vector

### 2.1.2 Navier-Stokes Equations

The Navier-Stokes equations conserve mass and momentum of Newtonian fluids and balance the observed properties  $\rho$  and  $u_i$ .

#### Continuity Equation

The continuity equation regards the mass and demands that the time variation of the mass within an observed volume and the convective mass flux over the volume surface balance for source free regions. Using  $\phi = 1$ , the generic transport equation yields

$$\frac{\partial}{\partial t} \int_{\bar{V}} \rho \, d\bar{V} + \oint_{S(\bar{V})} (\rho \tilde{u}_j) \, dS_j = 0. \quad (2.2)$$

Mind that in incompressible flows, the conservation of mass in Equation (2.2) simplifies towards a conservation of volume, i.e.  $\oint_{S(\bar{V})} \tilde{u}_j \, dS_j = 0$  (cf. Section 2.1.3).

#### Momentum Equation

The momentum equation is deduced from Newton's second law of motion and states that the sum of the time variation of the momentum within an observed volume and the convective momentum flux over the volume surface is induced by external forces. The equation arises from  $\phi = u_i$ , viz.

$$\frac{\partial}{\partial t} \int_{\bar{V}} (\rho u_i) \, d\bar{V} + \oint_{S(\bar{V})} (\rho u_i \tilde{u}_j) \, dS_j = \oint_{S(\bar{V})} (\tau_{ij} - p \delta_{ij}) \, dS_j + \int_{\bar{V}} f_i \, d\bar{V}. \quad (2.3)$$

The external forces are separated into surface and volume forces. The surface forces are composed from the Cartesian coordinates of the viscous stresses  $\tau_{ij}$  and the pressure  $p$ , while  $\delta_{ij}$  refers to the entries of the identity tensor and  $f_i$  marks the coordinates of the volume-specific forces. The viscous stresses of Newtonian fluids are modelled dependent on the strain-rate tensor  $s_{ij}$  and the dynamic viscosity  $\mu$ . For incompressible fluids, the strain-rate tensor is trace free and represented by the symmetric part of the velocity gradient and hence, the viscous stress coordinates are expressed by

$$\tau_{ij} = \mu \underbrace{\left( \frac{\partial u_i}{\partial x_j} + \frac{\partial u_j}{\partial x_i} \right)}_{2s_{ij}}. \quad (2.4)$$

### 2.1.3 Two-Phase Flow

The inherent conservative Volume-of-Fluid approach (VoF) by Hirt and Nichols (1981) is applied to capture the free surface between two immiscible fluid phases. The approach is an interface-capturing method, which balances the phase concentration  $c$  to determine the instantaneous, local volume of a particular phase. The local fluid properties  $\rho$  and  $\mu$  are determined from a simple equation of state (EoS), viz.

$$\rho = \rho_1 c_1 + \rho_2 c_2, \quad (2.5)$$

$$\mu = \mu_1 c_1 + \mu_2 c_2. \quad (2.6)$$

In the scope of this thesis, the primary phase (index 1) is assigned to the gas phase and the secondary phase (index 2) is assigned to the liquid phase. The EoS is supplemented by a compatibility condition, i.e.

$$c_1 + c_2 = 1 \quad \rightarrow \quad c_1 = c, \quad c_2 = 1 - c. \quad (2.7)$$

The present thesis is concerned with air/water flows. Hence, the fluid phases are considered immiscible

$$\frac{Dc}{Dt} = 0. \quad (2.8)$$

Moreover, the background material properties ( $\rho_1, \rho_2, \mu_1, \mu_2$ ) are deemed constant. Using the strong form of the mass balance in Equation (2.2)

$$\frac{D\rho}{Dt} = -\rho \frac{\partial u_i}{\partial x_i} \quad (2.9)$$

together with the EoS in Equations (2.5) and (2.6), a volume conservation constraint similar to incompressible single phase flows is obtained

$$(\rho_1 - \rho_2) \underbrace{\frac{Dc}{Dt}}_0 = \rho \frac{\partial u_i}{\partial x_i} \quad \rightarrow \quad \frac{\partial u_i}{\partial x_i} = 0. \quad (2.10)$$

Owing to this, the integral form of the concentration transport equation (2.8) states that source free regions demand a balance of the time variation within an observed volume and the convective concentration fluxes across the volume surfaces:

$$\frac{\partial}{\partial t} \int_{\bar{V}} c \, d\bar{V} + \oint_{S(\bar{V})} (c \tilde{u}_j) \, dS_j = 0. \quad (2.11)$$

Note that the VoF technique can be used to capture multiple phases by introducing the required number of volume concentrations (i.e. the fluid properties result from  $\rho = \sum c^k \rho^k$  and  $\mu = \sum c^k \mu^k$ ) and solving the resulting transport equations.

### 2.1.4 Turbulence Capturing

Turbulent flow is characterised by intense fluctuations in space and time and contains a wide range of interacting length and time scales. Direct numerical simulations (DNS), which fully resolve the entire turbulent motion, or large eddy simulations (LES), that resolve large turbulent structures, are numerically expensive and currently not practicable for complex flows at high Reynolds numbers. Further, DNS and LES are often not reasonable from an engineering point of view, as in many applications the focus is on integral mean quantities (e.g. mean forces on a body). Reynolds-averaged approaches (Ferziger and Perić 2002) offer an approximation of the turbulent effects by modelling the flow properties as sum of the Reynolds-averaged value  $\bar{\phi}$  and the fluctuation  $\phi^T$ , viz.

$$\phi = \bar{\phi} + \phi^T. \quad (2.12)$$

#### Reynolds-Averaged Navier-Stokes Equations

The substitution of the Reynolds-averaged approach from Equation (2.12) within all transport equations and subsequent ensemble averaging leads to significant simplifications of the numerical investigation of turbulent flows. For incompressible fluids, the density, the viscosity and the concentration can be considered as non-fluctuating properties. Since the definition implies that  $\overline{\phi^T} = 0$ , only the non-linear convective term of the momentum equation (2.3) results in second moments of velocity fluctuations, which have to be modelled to close the equation system. The resulting ensemble Reynolds-averaged Navier-Stokes (RANS) equations read

$$\frac{\partial}{\partial t} \int_{\bar{V}} \rho \, d\bar{V} + \oint_{S(\bar{V})} (\rho \bar{u}_j) \, dS_j = 0, \quad (2.13)$$

$$\frac{\partial}{\partial t} \int_{\bar{V}} (\rho \bar{u}_i) \, d\bar{V} + \oint_{S(\bar{V})} \left( \rho \bar{u}_i \bar{u}_j + \underbrace{\overline{\rho u_i^T u_j^T}}_{\substack{\text{Negative} \\ \text{Reynolds-} \\ \text{stress tensor}}} \right) \, dS_j = \oint_{S(\bar{V})} (\bar{\tau}_{ij} - \bar{p} \delta_{ij}) \, dS_j + \int_{\bar{V}} \bar{f}_i \, d\bar{V}. \quad (2.14)$$

Turbulent flows are characterised by an enhanced macroscopic mixing. In engineering applications the Reynolds-stress tensor is frequently modelled by the (incompressible) Boussinesq eddy-viscosity hypothesis as

$$-\overline{\rho u_i^T u_j^T} = \mu_t \underbrace{\left( \frac{\partial \bar{u}_i}{\partial x_j} + \frac{\partial \bar{u}_j}{\partial x_i} \right)}_{2\bar{s}_{ij}} - \frac{2}{3} \rho \delta_{ij} k. \quad (2.15)$$

Here,  $\mu_t$  refers to the eddy viscosity and  $\bar{s}_{ij}$  to the mean strain-rate tensor, while the turbulent kinetic energy  $k$  is defined as

$$k = \frac{1}{2} \overline{u_i^T u_i^T}. \quad (2.16)$$

Harmonising Equation (2.15) with Equation (2.4), one obtains an effective viscosity  $\mu_{\text{eff}}$ , being composed from the dynamic viscosity and the eddy viscosity, as well as an apparent mean pressure  $\hat{p} = \bar{p} + 2/3 \rho k$ . Thereby, Equation (2.14) can be written as

$$\frac{\partial}{\partial t} \int_{\bar{V}} (\rho \bar{u}_i) d\bar{V} + \oint_{S(\bar{V})} (\rho \bar{u}_i \bar{u}_j) dS_j = \oint_{S(\bar{V})} (\hat{\tau}_{ij} - \hat{p} \delta_{ij}) dS_j + \int_{\bar{V}} \bar{f}_i d\bar{V}. \quad (2.17)$$

In the remainder of this thesis, the Reynolds-averaged values are simply denoted by their variable name without repeatedly mentioning or marking the turbulent approach for the sake of brevity. The notation of the RANS equations is therefore consistent with Equations (2.2) and (2.3).

### Turbulence Models

Reynolds-averaging yields the introduction of a turbulent kinetic energy and an eddy viscosity as additional unknowns to characterise the turbulent behaviour of the flow. Two-equation models offer a simple, well established approach to close the equation system. Popular strategies are the  $k$ - $\epsilon$  model by Jones and Launder (1972), the  $k$ - $\omega$  model by Wilcox (1988) and blending approaches like the SST  $k$ - $\omega$  model by Menter (1994). The  $k$ - $\epsilon$  model is based on solving a transport equation for the turbulent kinetic energy  $k$  and for the turbulent dissipation  $\epsilon$ :

$$\frac{\partial}{\partial t} \int_{\bar{V}} (\rho k) d\bar{V} + \oint_{S(\bar{V})} (\rho \bar{u}_j k) dS_j = \oint_{S(\bar{V})} \left[ \left( \mu + \frac{\mu_t}{\sigma_k} \right) \frac{\partial k}{\partial x_j} \right] dS_j + \int_{\bar{V}} (P - \rho \epsilon) d\bar{V}, \quad (2.18)$$

$$\frac{\partial}{\partial t} \int_{\bar{V}} (\rho \epsilon) d\bar{V} + \oint_{S(\bar{V})} (\rho \bar{u}_j \epsilon) dS_j = \oint_{S(\bar{V})} \left[ \left( \frac{\mu_t}{\sigma_\epsilon} \right) \frac{\partial \epsilon}{\partial x_j} \right] dS_j + \int_{\bar{V}} \left( C_{\epsilon 1} P \frac{\epsilon}{k} - \rho C_{\epsilon 2} \frac{\epsilon^2}{k} \right) d\bar{V}, \quad (2.19)$$

while the eddy viscosity can be determined by

$$\mu_t = \rho C_\mu \frac{k^2}{\epsilon}. \quad (2.20)$$

The production rate of the turbulent kinetic energy  $P$  follows from

$$P = \mu_t \left( \frac{\partial u_i}{\partial x_j} + \frac{\partial u_j}{\partial x_i} \right) \frac{\partial u_i}{\partial x_j} \quad (2.21)$$

and the model coefficients typically read

$$C_{\epsilon 1} = 1.44, \quad C_{\epsilon 2} = 1.92, \quad C_\mu = 0.09, \quad \sigma_k = 1.0, \quad \sigma_\epsilon = 1.3. \quad (2.22)$$

The  $k$ - $\omega$  model is composed of a transport equation for the turbulent kinetic energy  $k$  and for the specific dissipation rate  $\omega = \epsilon / (C_\mu k)$ , viz.

$$\frac{\partial}{\partial t} \int_{\bar{V}} (\rho k) d\bar{V} + \oint_{S(\bar{V})} (\rho \bar{u}_j k) dS_j = \oint_{S(\bar{V})} \left[ \left( \mu + \frac{\mu_t}{\sigma_k^*} \right) \frac{\partial k}{\partial x_j} \right] dS_j + \int_{\bar{V}} (P - \rho \beta^* k \omega) d\bar{V}, \quad (2.23)$$

$$\frac{\partial}{\partial t} \int_{\bar{V}} (\rho\omega) d\bar{V} + \oint_{S(\bar{V})} (\rho\tilde{u}_j\omega) dS_j = \oint_{S(\bar{V})} \left[ \left( \mu + \frac{\mu_t}{\sigma_\omega^*} \right) \frac{\partial\omega}{\partial x_j} \right] dS_j + \int_{\bar{V}} \left( \alpha P \frac{\omega}{k} - \rho \beta \omega^2 \right) d\bar{V}. \quad (2.24)$$

The eddy viscosity follows from

$$\mu_t = \rho \frac{k}{\omega} \quad (2.25)$$

and the production rate of the turbulent kinetic energy can be obtained from Equation (2.21). The model coefficients are usually assigned to

$$\alpha = \frac{5}{9}, \quad \beta = 0.075, \quad \beta^* = 0.09, \quad \sigma_k^* = \sigma_\omega^* = 2.0. \quad (2.26)$$

While the  $k$ - $\epsilon$  model displays problems to mimic adverse pressure gradient flows correctly and shows shortcomings in the viscous sublayer modelling, the  $k$ - $\omega$  model proves to be very sensitive to free stream values, but is on the other hand advantageous in the immediate vicinity of a wall. An improvement of the turbulence formulation can therefore be obtained by blending the procedures. The SST  $k$ - $\omega$  model by Menter combines the  $k$ - $\epsilon$  model in the outer part of the boundary layer and the free stream with the  $k$ - $\omega$  model in the immediate vicinity of a wall. Further information are given in Menter (1994), Menter et al. (2003) and Wilcox (2006).

### 2.1.5 Initial and Boundary Conditions

The above-mentioned governing equations demand for initial and boundary conditions. A distribution at the initial observation time  $t^{(0)}$  has to be specified for all field variables  $\phi$  within the complete observed volume via

$$\phi \left( x_i, t^{(0)} \right) = \phi_{\text{init}}(x_i), \quad \forall x_i \in \bar{V}. \quad (2.27)$$

The employed boundary conditions are defined as Dirichlet conditions, which provide a field value at the given boundary

$$\phi(x_i, t) = \phi_{\text{ref}}(x_i, t), \quad \forall x_i \in S_{\mathcal{D}b}(\bar{V}), \quad (2.28)$$

or as Neumann conditions, which are based on the specification of a specific gradient normal to the boundary

$$\frac{\partial\phi}{\partial n}(x_i, t) = \frac{\partial\phi}{\partial n} \Big|_{\text{ref}}, \quad \forall x_i \in S_{\mathcal{N}b}(\bar{V}). \quad (2.29)$$

Here,  $S_{\mathcal{D}b}$  and  $S_{\mathcal{N}b}$  denote the surfaces with Dirichlet and Neumann boundary conditions, respectively, while  $n$  refers to the normal direction of the boundary. While the common employed Neumann condition within this thesis refers to a vanishing gradient, the pressure usually follows a gravity-based hydrostatic gradient when the influence of gravity is considered. Common boundary conditions represent inlets, outlets and (slip

or no-slip) walls. Symmetry planes are further frequently used to reduce the size of the observed domain.

The inlet boundary condition is based on prescribing the velocity, the concentration and the turbulent quantities, while the pressure is specified via a Neumann boundary condition.

The outlet boundary condition can be realised by different techniques. One approach refers to a (usually hydrostatic) prescribed pressure supplemented by zero normal gradients for the velocities, while another option ensures mass conservation and corrects the velocity values, which arise from a zero-gradient extrapolation using a bulk correction. Both alternatives define the remaining field variables via a zero normal gradient Neumann boundary condition.

The velocity at symmetry planes and slip walls has to be separated in normal and tangential direction. For non-thermal flows, both boundary types demand that all gradients vanish normal to the boundary (or arise from the gravity when regarding the pressure) – solely the normal component of the velocity follows a Dirichlet boundary condition, which prohibits flow across the boundary.

No-slip conditions specify the wall shear for the velocities, while the pressure and the concentration result from a Neumann boundary condition. The boundary conditions for the turbulent quantities are more complex, since the turbulent fluctuations are reproduced via turbulence models and further approaches are required to ensure a realistic wall behaviour. Solving the RANS equations, the resolution of the boundary layer differs between two common approaches: Low-Reynolds wall boundary conditions fully resolve the viscous sublayer, while high-Reynolds wall boundary conditions apply a logarithmic wall-function for the mean velocity parallel to the wall. Both approaches differ in the prescribed wall shear and near-wall turbulence. A detailed discussion of the boundary condition is given by Rung (2001) and Ferziger and Perić (2008).

## 2.2 Finite-Volume Method

The transport equations from Section 2.1 have to be discretised in space and time in order to solve the numerical problem. The employed procedure is based on an implicit, second-order accurate finite-volume approximation of the transport equations in their strong conservation form and employs a cell-centred, co-located variable arrangement (Ferziger and Perić 2002) on fully unstructured computational grids composed from arbitrary polyhedral cells.

The finite-volume method provides an inherently conservative approach. It is based on subdividing the computational domain  $V$  into a finite number of control volumes  $\Delta V$  and solving the transport equations for each cell in order to determine the field variables. Each cell centre is marked with  $P$ , centres of the corresponding cell faces with  $F$  and the adjacent neighbouring cell centres with  $N_F$ . Figure 2.1 illustrates an arbitrary arrangement of two adjacent polyhedral control volumes.  $\Delta V_P$  marks the volume of the

cell with the centre  $P$  and  $\Delta S_{j,F}$  denotes the entries of the face area vector. The entries of the vector connecting the cell centres  $P$  and  $N_F$  follow from

$$d_{j,F} = x_{j,N_F} - x_{j,P} \quad (2.30)$$

with  $d_F = \|d_{j,F}\|$  being the Euclidean norm of the distance vector.

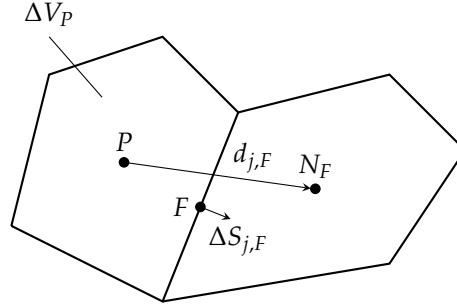


Figure 2.1: Illustration of two adjacent polyhedral control volumes, separated by the face with the centre  $F$ .  $P$  denotes the centre of the observed cell and  $N_F$  the centre of the neighbouring cell.  $\Delta V_P$  marks the cell volume, while  $\Delta S_{j,F}$  and  $d_{j,F}$  denote the entries of the face area vector and the entries of the vector connecting the cell centres.

The finite-volume method comprises approaches for the approximation of spatial integrals, time derivatives and gradients as well as interpolation schemes for the reconstruction of face values (aka. as fluxes). The face values and related fluxes have to be reconstructed since all variables of the employed algorithm are stored in a cell-centred, co-located arrangement. The description of the finite-volume method closes with an insight into the specific influences arising from the employed boundary conditions.

### 2.2.1 Spatial Integrals

Spatial integrals are approximated by a second-order accurate midpoint rule. Integrals over the cell volume  $\Delta V_P$  are determined using the field variable in the cell centre  $\phi_P$

$$\int_{\Delta V_P} \phi \, dV \approx \phi_P \Delta V_P \quad (2.31)$$

and surface integrals are composed by a sum over all faces of the specific cell, followed by the application of the midpoint rule for each face

$$\oint_{S(\Delta V_P)} \phi \, dS_j \approx \sum_F [\phi \Delta S_j]_F . \quad (2.32)$$

Here,  $\phi_F$  denotes the value in the centre of the cell face, while  $\Delta S_{j,F}$  marks the entries of the corresponding face area vector.

### 2.2.2 Time Derivatives

Time derivatives are based on a first-order implicit Euler approximation

$$\left. \frac{\partial \phi}{\partial t} \right|^{(n)} \approx \frac{\phi^{(n)} - \phi^{(n-1)}}{\Delta t} \quad (2.33)$$

or a second-order implicit three time-level approach

$$\left. \frac{\partial \phi}{\partial t} \right|^{(n)} \approx \frac{3\phi^{(n)} - 4\phi^{(n-1)} + \phi^{(n-2)}}{2\Delta t}. \quad (2.34)$$

$\Delta t$  refers to the applied constant time step, while the upper indices indicate the current ( $n$ ) and the previous time levels ( $n - 1$ ) and ( $n - 2$ ). Time derivatives are consistently evaluated using the field variable in the cell centre  $P$ . Both approaches are based on an implicit treatment of the unknown variable  $\phi^{(n)}$ , while the values of previous time levels explicitly contribute to the right-hand side of the equation system.

### 2.2.3 Determination of Gradients

On unstructured grids, gradients in the cell centre are commonly determined via Gauss' theorem or a least-squares approach. The latter is applied within a weighted formulation to enhance the accuracy and stability.

#### Gauss' Theorem

Gauss' theorem states that the gradient within a control volume corresponds with the field values at the associated surfaces

$$\int_{\Delta V_P} \frac{\partial \phi}{\partial x_j} dV = \oint_{S(\Delta V_P)} \phi dS_j. \quad (2.35)$$

Employing the approximations for the spatial integrals given in Equations (2.31) and (2.32) leads to a conservative approximation of the gradient in the cell centre  $P$ , viz.

$$\left. \frac{\partial \phi}{\partial x_j} \right|_P \approx \frac{1}{\Delta V_P} \sum_F [\phi \Delta S_j]_F. \quad (2.36)$$

### Least-Squares Approach

The least-squares approach employs the values and geometric relations of the observed cell centre  $P$  and all neighbour cell centres  $N_F$  to determine the gradient. Taylor series expansion states

$$\phi_{N_F} \approx \phi_P + d_{j,F} \left( \frac{\partial \phi}{\partial x_j} \right)_P \quad (2.37)$$

for each of the faces composing the surface of the specific cell. Equation (2.37) leads to an overdetermined system when solving for the gradient, since the number of neighbour cells always exceeds the dimension by at least one. An approximate solution of the gradient can be obtained by means of a least-squares method. Although it does not follow a conservative treatment, it enhances the accuracy and stability for irregular cells when using a weighted formulation (Rung 2008), viz.

$$\left. \frac{\partial \phi}{\partial x_j} \right|_P \approx D_{ji}^{-1} \sum_F w_F d_{i,F} (\phi_{N_F} - \phi_P), \quad (2.38)$$

where the symmetric matrix  $D_{ij}$  and the weight  $w_F$  comprise geometric information:

$$D_{ij} = \sum_F [w d_i d_j]_F, \quad w_F = \frac{1}{d_F}. \quad (2.39)$$

### 2.2.4 Reconstruction of Face Values

The reconstruction of face values is based on the interpolation of cell-centre values from the cell centre  $P$  and the adjacent cell centre  $N_F$ . The obvious reconstruction of the value in the face centre is given by a linear interpolation to the intersection point  $F'$  of the face area and the vector  $d_{j,F}$  connecting the cell centres  $P$  and  $N_F$  (cf. Figure 2.1), supplemented by a gradient-based extrapolation if the face centre does not coincide with the intersection point:

$$\phi_F \approx \underbrace{(1 - \lambda_F) \phi_P + \lambda_F \phi_{N_F}}_{\text{Interpolation}} + \underbrace{(x_{j,F} - x_{j,F'})}_{\text{Extrapolation}} \left( \frac{\partial \phi}{\partial x_j} \right)_{F'}. \quad (2.40)$$

The interpolation factor reads

$$\lambda_F = \frac{\Delta S_{j,F} (x_{j,F} - x_{j,P})}{[\Delta S_j d_j]_F}. \quad (2.41)$$

The linear interpolation scheme is often referred to as central-differencing scheme (CDS). The numerical implementation of the extrapolation-based correction term employs an explicit treatment to obtain second-order accuracy on unstructured grids. The

embedded gradient of the field variable in the intersection point follows from linear interpolation.

In general, the interpolation schemes for the face variables should characterise the physical transport properties of the particular (convective or diffusive) term. Unbiased, symmetric interpolation schemes (such as CDS) are the method of choice for non-directional information transport, while directional or biased interpolation schemes adhere for an orientation of the information transport. Most field variables and gradients are simply interpolated by Equation (2.40), though, convective fluxes are characterised by their directional transport and hence demand for special attention. The gradient within in the diffusive term can be directly determined from the cell-centre values. Note that the surface pressure, which occurs in the momentum equation (2.3), is explicitly imposed as a volume-based source term using Gauss' theorem in Equation (2.35).

### Convective Transport

Convective fluxes are characterised by their directional information transport, which establishes the use of upwind-biased formulae. The finite approximation of the generic convective term in Equation (2.1) yields

$$\oint_{S(\Delta V)} (\rho \phi \tilde{u}_j) dS_j \approx \sum_F \phi_F \underbrace{[\rho \tilde{u}_j \Delta S_j]_F}_{\dot{m}_F}. \quad (2.42)$$

The mass flux  $\dot{m}_F$  is composed from the face values of the density and the velocity as well as the entries of the face area vector. The density follows from the concentration at the face, cf. Equation (2.5), while the velocity describes the transport and is therefore interpolated using the central-differencing scheme in Equation (2.40). The mass flux is evaluated at the previous iteration – employing a Picard linearisation for the convective term if  $\phi \neq 1$ . The transported quantity  $\phi_F$  physically demands for directional flow information, which can be captured by a first-order upwind-differencing scheme (UDS):

$$\phi_F \dot{m}_F \approx \phi_P \cdot \max[\dot{m}_F, 0] - \phi_{N_F} \cdot \max[-\dot{m}_F, 0]. \quad (2.43)$$

The occurring first-order accuracy numerically enhances the diffusion. This is especially problematic when regarding the momentum transport within high Reynolds-number flows or the concentration transport, which requires a sharp interface. However, the unbiased CDS approximation of convective fluxes by Equation (2.40) is not only physically inconsistent, but reduces the stability of the equation system. Employing a blending technique enhances the accuracy whilst conserving the stability of the upwind-differencing scheme when being applied by means of a deferred correction approach:

$$\phi_F = \phi_F^{\text{UDS}} + \underbrace{\kappa_0 (\phi_F^{\text{CDS}} - \phi_F^{\text{UDS}})}_{\text{Explicit correction}}, \quad \kappa_0 \in [0, 1]. \quad (2.44)$$

The blending factor  $\kappa_0$  blends the different approximation techniques. The UDS contribution is treated implicitly, which simplifies the algorithm and ensures its stability.

The CDS part contributes via an explicit correction. The subsequent high-order schemes refer to the same deferred correction technique and explicitly apply high-order terms. The  $\kappa$ -scheme provides a compact notation, cf. Rung (2008):

$$\phi_F \approx \phi_F^{\text{UDS}} + \frac{1}{2} \left[ \kappa (\phi_{N_F} - \phi_P) - (1 - \kappa) d_{j,F} \left( \frac{\partial \phi}{\partial x_j} \right)_P \right], \quad \kappa \in [-1, 1], \quad (2.45)$$

which yields different approximation concepts, depending on the factor  $\kappa$ . Since an additional upstream field value cannot be easily identified on unstructured grids, it is reconstructed via the gradient in  $P$ . The QUICK scheme (Leonard 1979), which provides a quadratic upwind interpolation, is realised by  $\kappa = 0.5$ . To prevent numerical oscillations, the determined face value should not exceed the neighbouring field values. A monotonicity preserving variant of Equation (2.45) is the MUSCL scheme by van Leer (1997), which restricts the interpolation technique to be total variation diminishing (Harten 1983). Further details about the implementation of an extended MUSCL scheme by Lien and Leschziner (1994) can be found in Stück (2011).

The approximation of the convective concentration transport in Equation (2.11)

$$\oint_{S(\bar{V})} (c \tilde{u}_j) dS_j \approx \sum_F c_F \underbrace{[\tilde{u}_j \Delta S_j]_F}_{\dot{v}_F} \quad (2.46)$$

is crucial for a sharp interface between two fluid phases. While the volume flux  $\dot{v}_F$  is simply approximated by applying the central-differencing scheme in Equation (2.40), a more elaborate interpolation technique has to be employed for the reconstruction of the transported quantity, i.e. the face concentration  $c_F$ . A well-established approximation concept is the High-Resolution Interface Capturing (HRIC) scheme by Muzaferija and Perić (1999), which blends the numerically stable first-order upwind-differencing scheme with a compressive (limited) downwind contribution. Within the HRIC scheme, the proportions of the upwind and the downwind contribution adhere to the local Courant number as well as to the relative angle between the fluid interface and the cell face. An orthogonal interface orientation is correctly captured by an upwind scheme, whereas an inclined or parallel arrangement demands for downwind information to ensure a sharp interface. For the second case, the local Courant number  $Co_F$  is employed to blend between a compressive (limited) downwind-biased scheme for small Courant numbers ( $Co_F < 0.3$ ) and the stabilising upwind-biased scheme for  $Co_F > 0.7$ . The approximation is applied by means of a deferred correction approach, i.e. the downwind information contribute via an explicit correction. A similar approach, that is routinely used for industrial applications, is the CICSAM scheme by Ubbink (1997).

### Diffusive Transport

The finite approximation of the generic diffusive term in Equation (2.1) yields

$$\oint_{S(V)} \left( \Gamma \frac{\partial \phi}{\partial x_j} \right) dS_j \approx \sum_F \left[ \Gamma \left( \frac{\partial \phi}{\partial x_j} \right) \Delta S_j \right]_F = \sum_F \left[ \Gamma \left( \frac{\partial \phi}{\partial n} \right) \Delta S \right]_F \quad (2.47)$$

with  $\Delta S_F = \| \Delta S_{j,F} \|$  being the Euclidean norm of the face area vector. The diffusion coefficient  $\Gamma$  is composed from the dynamic or turbulent eddy viscosity, as well as constant model coefficients, dependent on the considered conservation equation from Section 2.1. The dynamic viscosity is a material value and therefore determined from the concentration at the face, cf. Equation (2.6), while the eddy viscosity follows from linear interpolation. The remaining product in Equation (2.47) represents the projection of the gradient in direction of the face area vector, which again employs a deferred correction approach:

$$\left. \frac{\partial \phi}{\partial n} \right|_F \approx \frac{\phi_{N_F} - \phi_P}{d_F} + \underbrace{\left( \frac{\partial \phi}{\partial x_j} \right)_F \left( n_{j,F} - \frac{d_{j,F}}{d_F} \right)}_{\text{Explicit correction}} \quad (2.48)$$

with  $n_{j,F} = \Delta S_{j,F} / \Delta S_F$  being the components of the surface normal. The first term can be directly determined from the cell-centre values, while the deferred correction technique is employed to respect the orientation of the gradient within an explicit correction. The gradient in the explicit correction is determined via linear interpolation and the approach can be augmented for unfavourable metrics, i.e.  $\phi_F \rightarrow \phi_F (n_{j,F} d_{j,F})^k$ , cf. Rung (2008).

## 2.2.5 Boundary Conditions

Boundary conditions provide a concept for the flow variables at the outer grid limitations. The boundary values contribute to the determination of the gradient and influence the appearing convective and diffusive fluxes. The numerical implementation of the occurring boundary fluxes refers to auxiliary boundary cells, which have no physical volume and are located within the coordinates of the particular boundary face. Dirichlet and Neumann boundary conditions either provide a boundary value or extrapolate the inner field value, demanding a vanishing spatial gradient normal to the face for a zero-gradient assumption, cf. Section 2.1.5. The following paragraphs summarise the influence on the convective and diffusive transport.

### Convective Transport

The convective transport is governed by the mass flux  $\dot{m}_F$  (or the volume flux  $\dot{v}_F$ ). The inlet boundary condition describes the inflow into the simulation domain, which results from the given boundary value; the outlet boundary condition manages the outflow by extrapolating the inner field value. Symmetry boundary conditions, as well as (slip or no-slip) walls, prohibit flow across the boundary, which leads to a vanishing convective flux ( $\dot{m}_F = 0 / \dot{v}_F = 0$ ).

## Diffusive Transport

The diffusive transport arises from the spatial gradient normal to the face. Hence, the diffusive flux at the inlet can be obtained from the difference between the inner field value and the prescribed boundary value. The zero-gradient Neumann boundary condition at the outlet provokes a vanishing diffusive term.

At symmetry planes and slip walls, the field variables are generally extrapolated, which leads to a vanishing diffusive transport. However, the normal component of the velocity adheres to a different restriction. While the tangential velocity is extrapolated, the suppression of the velocity normal to the wall leads to a diffusive flux arising from normal stresses. Based on the viscous stress tensor in Equation (2.4), the approximation of the diffusive fluxes leads to

$$\mathcal{F}_i^{\text{diff}} = -2\mu_F \Delta S_F \frac{(u_{k,Bd} - u_{k,P}) n_{k,F}}{d_{j,F} n_{j,F}} n_{i,F} \quad (2.49)$$

with  $u_{k,Bd}$  being the entries of the boundary velocity, which includes the extrapolated tangential velocity and a potential wall velocity.

The no-slip boundary condition implies that the fluid velocity equals the wall velocity, which leads to a gradient of the tangential velocity normal to the wall. The resulting wall shear stresses contribute to the diffusive term, while for incompressible fluids, no spatial gradient of the normal velocity occurs due to Equation (2.2). The diffusive fluxes yield

$$\mathcal{F}_i^{\text{diff}} = -\mu_F \Delta S_F \frac{(u_{k,Bd} - u_{k,P}) t_{k,F}}{d_{j,F} n_{j,F}} t_{i,F}. \quad (2.50)$$

Here,  $t_{i,F}$  denotes the entries of the surface tangent. Application of a high-Reynolds boundary condition modifies the viscosity based on a logarithmic wall function. Further details on turbulent variables go beyond the scope of this thesis. Detailed information can be found in Rung (2001) and Ferziger and Perić (2008).

## 2.3 Numerical Procedure

The Navier-Stokes procedure FreSCo<sup>+</sup> (Rung et al. 2009) solves the (at times Reynolds-averaged) Navier-Stokes equations supplemented by auxiliary transport equations for mixture fractions, turbulence etc., cf. Section 2.1. The segregated algorithm is based on the implicit, second-order accurate finite-volume approximation of the transport equations in their strong conservation form given in Section 2.2. The in-house code employs a cell-centred, co-located variable arrangement and is capable to process fully unstructured and locally refined computational grids of arbitrarily shaped polyhedral cells. A Volume-of-Fluid method or a two-way coupled Euler/Lagrange method can be used to model multiphase flows and cavitation (Yakubov et al. 2013, 2015). Several RANS and scale resolving closures (LES, DES) are available to mimic the effect of turbulence. Body motion can be realised by a prescribed motion or in a floating manner according to the embedded quaternion-based six degrees of freedom (6DoF) module

(Luo-Theilen and Rung 2017). Grid fluxes of moving or deforming meshes are computed in line with the space conservation law (Demirdžić and Perić 1988). The algorithm is parallelised using a domain decomposition technique based on a multi-criterion graph-partitioning approach (Karypis and Kumar 1995). Inter-processor communication employs the message passing interface (MPI) protocol.

The segregated iterative solution procedure begins with an update of the current position of the computational grids according a potential body motion and sequentially solves the approximated transport equations, each transposed as equation system containing the specific field variables. The pressure-velocity coupling follows from the SIMPLE algorithm, which at first determines the entries of the velocity vector from the momentum equation (2.3) using an estimated pressure  $p^*$ . A *pressure correction equation* is formed by combining the momentum equation and the continuity equation (2.2), cf. Ferziger and Perić (2002). Following, the pressure correction  $p'$ , which is required to compensate the mass imbalances induced by an inaccurate pressure estimation in the momentum equation, is determined. Finally, the pressure and the velocities are corrected. The spatial odd-even decoupling of the cell-centred formulation is suppressed by an artificial dissipation pressure contribution to the mass imbalance along the line of the correction by Rhie and Chow (1983). Subsequently, all other considered field variables are determined by solving the respective transport equations.

Since the transport equations are coupled by the field variables and comprise non-linear contributions, an iterative solution is mandatory. Inner iterations describe the number of solution cycles for one equation system, while outer iterations mark the repeated execution of the complete solution procedure. The iterations proceed until a maximum number of iterations is reached or the integral residual over all control volumes evinces a satisfying convergence. Transient simulations are characterised by a time loop that repeatedly performs the described sequence until a prescribed number of time steps is completed. The convergence is commonly ensured by means of an under-relaxation technique, which decreases the rate of change of the field variables when solving an equation system, cf. Stück (2011).



## 3 Overset-Grid Approach

The overset-grid approach couples an unlimited number of grids implicitly on the level of the equation system and provides a straightforward method for the simulation of multiple bodies with relative motion and mutual hydrodynamic interaction. The initial grid priority as well as the local resolution of the coupled grids govern the dynamic grid prioritisation process. The motion of the individual foreground grid(s) usually depends on the respective motion of the meshed body. The latter is either prescribed by a guided motion module or determined by the hydrodynamical/mechanical interaction forces using the quaternion-based 6DoF module. Load balancing is dynamically controlled and updated (Brunswig and Rung 2013).

The introduction outlined a conservative inter-grid coupling and a dynamic body contact as primary challenges of overset-grid procedures. This chapter starts with a general description of the employed overset-grid approach with the focus on the applied interpolation algorithms from Brunswig and Rung (2011). It then describes the developed mass conservation practices to ensure a conservative inter-grid coupling and introduces an inter-grid coupling for bodies featuring dynamic contact.

### 3.1 Interpolation Algorithms & Baseline Inter-Grid Coupling

The inter-grid coupling is based on an elaborate priority management, which blanks cells for regions covered by multiple grids (Hadžić 2006, Brunswig and Rung 2011). Thereafter, interpolation-based links between disjunct grids are compiled adjacent to the blanked areas. The inter-grid coupling distinguishes between active (*solve*), inactive (*ignore*) and dependent (*interpolation*) cells. In the latter case, field values need to be reconstructed from an interpolation of partner-grid donors. Suitable donors are selected from active cells of the partner grids. Figure 3.1 shows an exemplary arrangement of the different cell types on two overlapping grids in a two-dimensional configuration. The foreground grid and its corresponding labels are coloured in blue, while the background grid and its corresponding labels are coloured in black. Note that solve cells are not coloured.

The amount of donor cells and the specific donor information differ between the different interpolation schemes, i.e. a simple low-order injection to the interpolation cell  $I$  in Figure 3.1 might only involve values from the nearest donor  $\mathcal{D}_1$ , whereas a simplex-based interpolation scheme involves values from three donors in 2D ( $\mathcal{D}_1, \mathcal{D}_2, \mathcal{D}_3$ ) or four donors in 3D and perhaps even their gradients to obtain second-order accuracy.

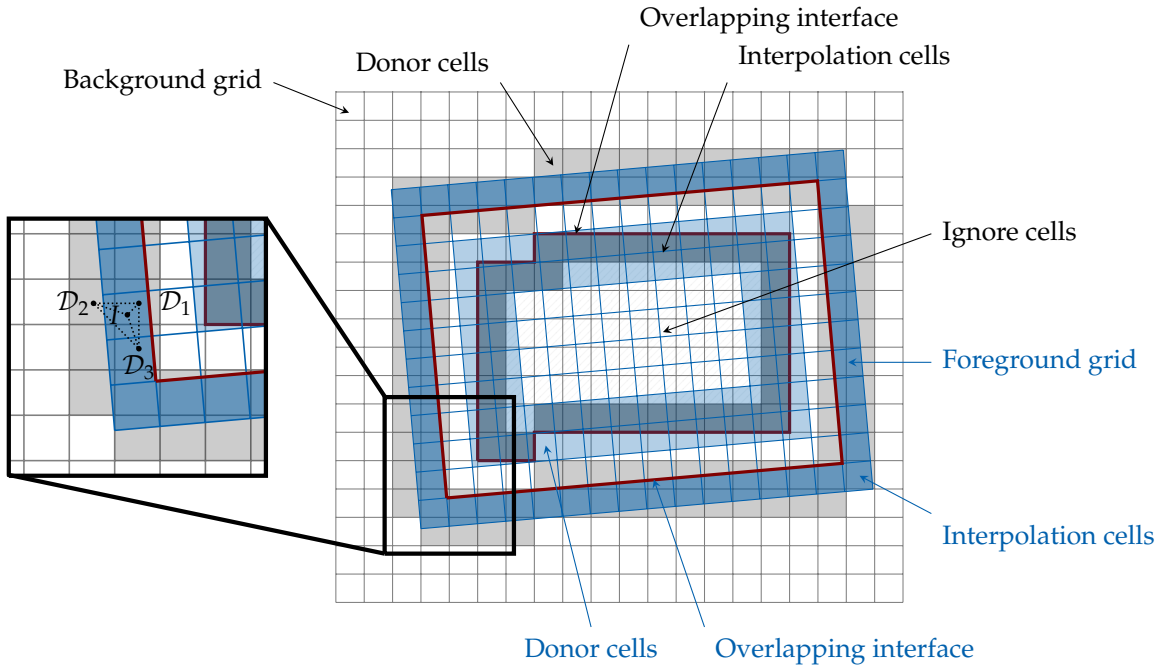


Figure 3.1: Illustration of the different cell types for two overlapping grids in a two-dimensional configuration. The foreground grid and its corresponding labels are coloured in blue, while the background grid and its corresponding labels are coloured in black. The overlapping interfaces between the interpolation cells and the adjacent solve cells are indicated in red. Note that the solve cells are not coloured. The enlarged view pictures an example of an interpolation cell ( $I$ ) and the three involved donor cells ( $\mathcal{D}_1, \mathcal{D}_2, \mathcal{D}_3$ ) for a related simplex.

The employed interpolation algorithms are all based on a weighted interpolation of cell-centred variables from donor cells to interpolation cells

$$\phi_I = \sum_{\beta=1}^{n_{\mathcal{D}}} w_{\beta} \phi_{\beta} + \delta. \quad (3.1)$$

$\phi_I$  denotes the interpolated field value, while  $\phi_{\beta}$  and  $w_{\beta}$ , with  $\sum_{\beta=1}^{n_{\mathcal{D}}} w_{\beta} = 1$ , are the field values and interpolation weights of the  $n_{\mathcal{D}}$  donor cells for the location  $I$ . The explicit coupling parameter  $\delta$  contains second-order information, e.g. the spatial gradients of the donor cells. Available interpolation options are the zero-order injection from the nearest donor cell, the interpolation from a cell cluster and the interpolation from a simplex of donor cells. The cell cluster is composed of the nearest donor cell and its neighbours. The respective interpolation weights are based on the inverse distance of the cell centres. The simplex-based interpolation can be first- or second-order accurate and weighted with the inverse sub-simplex areas (2D) or volumes (3D). In order to couple the grids implicitly, the transport equations for the interpolation cells are replaced by Equation (3.1). Figure 3.2 illustrates the interpolation cells within a two-grid arrangement and shows an exemplary equation system for the implicit coupling approach, i.e. the interpolation

stencils are directly substituted into the coefficient matrix. The interpolated values are depicted in red and enter the coefficient matrix with a unity value on the main-diagonal, whereas the donor entries ( $-w_\beta$ ) are marked in yellow. The right-hand side terms inhere the explicit contributions  $\delta$  of Equation (3.1) and are also marked in yellow.

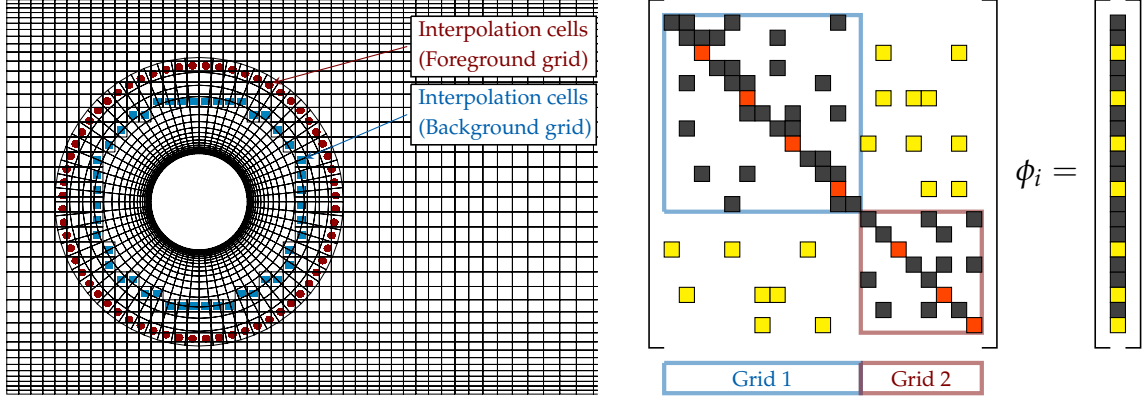


Figure 3.2: Illustration of the implicit coupling approach (right) for a two-grid arrangement (left). The interpolation of Equation (3.1) is cast into the equation system. Matrix: red unity entries on the main-diagonal for the interpolation cells and yellow negative donor weights on the off-diagonal. RHS: yellow entries for the explicit parts.

Since the SIMPLE algorithm is used to update the pressure, its implicit coupling is handled by interpolating the pressure correction  $p'$ . The interpolation has to result in the same pressure in the interpolation cell and the donor cells, even if the initial pressure values  $p^*$  differ. This leads to an alternative interpolation formula for the interpolated pressure correction value, viz.

$$p'_I = \sum_{\beta=1}^{n_D} w_\beta p'_\beta + \frac{1}{\vartheta} \left( \sum_{\beta=1}^{n_D} w_\beta p_\beta^* - p_I^* + \delta(p^*) \right). \quad (3.2)$$

While the first part of Equation (3.2) consists of the interpolation of the pressure correction values  $p'_\beta$ , the second part represents the coupling between the initial pressure values in the interpolation cell  $p_I^*$  and the donor cells  $p_\beta^*$ . This correction is combined with further explicit coupling information of the parameter  $\delta(p^*)$  and exposed to the reciprocal value of the under-relaxation factor  $\vartheta$  used by the pressure correction scheme. Continuous updating of the pressure values during the iterative solution process usually supersedes the second part of Equation (3.2). Different from single-grid simulations, the pressure correction equation system for implicitly coupled overset grids is non-symmetric due to the non-symmetric entries from the coupling procedure. Thus, a suitable iterative solver for non-symmetric systems, i.e. a biconjugate gradient (BiCG) method, is employed.

## 3.2 Mass Conservation Practices

As indicated by Equations (3.1) and (3.2) and Figure 3.1, the present grid coupling is not based upon fluxes but the direct interpolation of cell-centre values. This simplifies the coupling procedure for arbitrary disjunct grids, but results in erroneous fluxes across the overlapping grid boundaries, which do not necessarily conserve the fluid mass.

As explained in Section 2.3, the objective of the employed SIMPLE algorithm is to determine the pressure correction, which is required to compensate the mass imbalances being induced by an inaccurate pressure estimation in the momentum equation. Without any mass conservation practice, the erroneous fluxes across the overlapping grid boundaries cause an additional pressure correction, which leads to an erroneous pressure.

The essential idea is to add up the erroneous mass fluxes at the *overlapping interfaces* (depicted as red lines in Figure 3.1), which are determined by the  $n_{\mathcal{F}}$  interior faces between the interpolation cells and the adjacent solve cells. Subsequently, the defect is counteracted by either a virtual adaption of the cell volumes or a correction of the mass fluxes at the overlapping interfaces. The mass defect of the overset approach  $\Delta\dot{M}_O$  is defined as the sum of the mass fluxes across the overlapping interfaces:

$$\Delta\dot{M}_O = \sum_{\gamma=1}^{n_{\mathcal{F}}} \dot{m}_{\gamma}. \quad (3.3)$$

The respective challenge refers to identifying local corrections of a global defect  $\Delta\dot{M}_O$ .

### 3.2.1 Volume Correction Approach

The first correction approach is deduced from the finite-volume approximation of the continuity equation (2.2) for single-phase flows using the implicit Euler approximation for the time derivative:

$$\left[ \frac{(\rho\Delta V)^{(n)} - (\rho\Delta V)^{(n-1)}}{\Delta t} \right]_P = - \sum_F \dot{m}_F^{(n)}. \quad (3.4)$$

Experience shows that the mass defect introduced by the interpolation is usually quite small compared to the global mass flux (below 1%). Based on the idea of compensating the interpolation-induced mass defect  $\Delta\dot{M}_O$  by virtually changing the cell volumes  $\Delta V$  while keeping a constant density, the correction of a cell volume states

$$\Delta V^{(n)} = \Delta V^{(n-1)} - \frac{\Delta\dot{M}_O}{n_{C_S} \rho} \Delta t. \quad (3.5)$$

$n_{C_S}$  marks the total number of all solve cells and the upper indices indicate the current and the previous time level. This virtual volume adaptation compensates the global

mass imbalance, which forms the right-hand side of the pressure correction scheme, in proportion of the overset-induced erroneous fluxes, viz.

$$\dot{m}_{\text{corr}} = \dot{m} + \rho \underbrace{\frac{\Delta V^{(n)} - \Delta V^{(n-1)}}{\Delta t}}_{-\Delta \dot{M}_O / n c_S}. \quad (3.6)$$

The correction approach offers a very simple approach to obtain a mass conservative flow field. Although it is based on a fictitious change of all cell volumes for the complete set of partial differential equations, a consistent manipulation of the face areas or the mass fluxes at the overlapping interfaces is not included and no local information is considered. The expected benefit of the approach is a smooth pressure field which is free from spurious oscillations even for non-vanishing net inter-grid fluxes.

### 3.2.2 Flux Correction Approaches

The second investigated option is to correct the mass fluxes at the overlapping interfaces to restore the global mass balance, i.e.

$$\sum_{\gamma=1}^{n_F} (\dot{m}_\gamma + \delta \dot{m}_\gamma) = 0. \quad (3.7)$$

Such a flux correction practice was formerly suggested by Hadžić (2006). It is based on correcting the mass flux  $\dot{m}_F$  through face  $F$  by its weighted contribution to the global imbalance. The related flux correction reads

$$\delta \dot{m}_F = -\frac{|\dot{m}_F|}{\sum_{\gamma=1}^{n_F} |\dot{m}_\gamma|} \Delta \dot{M}_O. \quad (3.8)$$

A drawback of this approach is that it does not inhere any information related to the local solution quality, particularly not the local mass flux imbalance. This is illustrated by a simple one-dimensional example depicted in Figure 3.3. The figure reveals the deficit of missing local information for the example of two overlapping interfaces (marked in red), where one flux is vanishing. In this case, the procedure employing Equation (3.8) would always correct the non-zero flux to zero (cf. left-hand side of Figure 3.3) although a correction of the other flux could be much more appropriate.

In order to address this issue, a second flux correction practice is suggested. The correction aims to capture local effects when distributing the global mass defect (cf. right-hand side of Figure 3.3). The divergence of the velocity between the donor cells and the interpolation cell offers a possibility to measure the local defect in the flow. Its

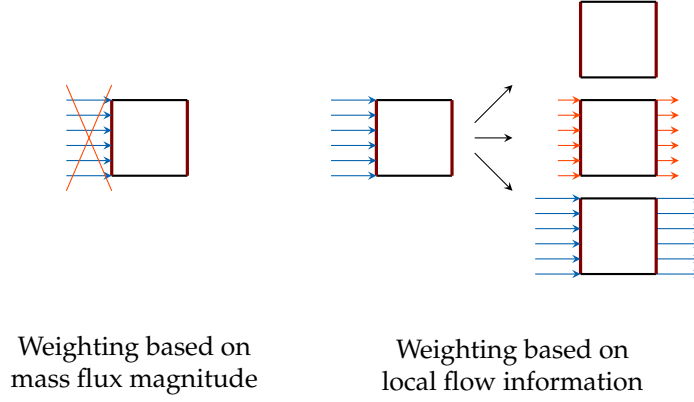


Figure 3.3: Flux correction proportional to their magnitude according to Hadžić (2006), or based on local flow information.

magnitude is used in combination with the volume of the interpolation cell to determine the local flux correction, i.e.

$$\delta \dot{m}_F = - \frac{\left( \left| \frac{\partial u_i}{\partial x_i} \right| \Delta V_I \right)_F}{\sum_{\gamma=1}^{n_F} \left( \left| \frac{\partial u_i}{\partial x_i} \right| \Delta V_I \right)_\gamma} \Delta \dot{M}_O. \quad (3.9)$$

The magnitude of the velocity divergence of an interpolation cell is obtained from a least-squares approach regarding the velocity differences and the distances between the interpolation cell  $I$  and its  $n_D$  corresponding donor cells

$$\left| \frac{\partial u_i}{\partial x_i} \right| \approx \left| \frac{\sum_{\beta=1}^{n_D} (u_{i,\beta} - u_{i,I})(x_{i,\beta} - x_{i,I})}{\sum_{\beta=1}^{n_D} (x_{i,\beta} - x_{i,I})^2} \right|. \quad (3.10)$$

### 3.3 Inter-Grid Coupling for Dynamic Body Contact

The interplay of hydrodynamically interacting bodies is usually buffered by a fluid layer. This guarantees a sufficient overlap of fluid cells, which is commonly required to couple the grids at the overlapping interfaces. Colliding bodies or bodies in direct proximity often do not comply with this condition. An example is illustrated in Figure 3.4, which shows two cylinders in direct proximity. The respective cells with invalid donor cells (aka. *critical cells*) are marked in red.

Cell blanking is applied for regions that are covered by multiple grids, which requires coupling information at the overlapping interfaces. A missing inter-grid coupling is problematic, since it implies mass defects due to the artificial openings between the blanked area and the active simulation domain. Preserving a minimal gap by using an extreme local refinement deteriorates the computational efficiency and provides no solution for collision simulations. The developed strategy therefore introduces artificial boundary conditions in critical areas. This requires a dynamic identification

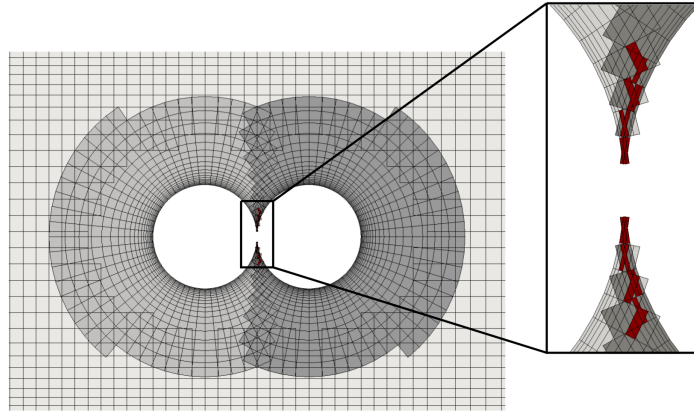


Figure 3.4: Two cylinders in direct proximity. The cells with missing donor information are marked in red.

of the critical cells in the vicinity of the contact zone and a subsequent manipulation of the computational model. A simple collision procedure is applied to prohibit the penetration of floating bodies.

### 3.3.1 Detection of Critical Areas

The detection of critical areas is embedded into the existing grid-coupling algorithm. The procedure simply identifies interpolation cells with invalid donors due to small gaps between bodies in direct proximity, which has been previously applied by Noack et al. (2009). The detection algorithm initially tries to achieve a valid coupling following a low-order scheme, i.e. reducing the number of donor cells in Equation (3.1). A reduction of the order reduces the required overlap and thereby enhances the coupling possibility. If no reduction is possible, for example if the nearest donor cell itself is dependent on the interpolation cell of the partner grid (aka. *cyclic interpolation*)

$$\phi_I = f(\phi_D) \quad \text{and} \quad \phi_D = f(\phi_I), \quad (3.11)$$

the critical cell is deactivated and tagged as *inactive*. The inactive cell is marked for proximity corrections if it lays within a critical distance to a wall boundary. Within this thesis, critical distances of ten cells are generally chosen, which reliably covers the typical occurring coupling problems within a wall distance of three cells. Small separate areas of active cells are located by means of a flood fill algorithm and likewise deactivated. The influence of a deactivated cell on the adjacent solve cells is suppressed by introducing an artificial boundary expressed by the manipulation of the coefficients of the equation system.

### 3.3.2 Artificial Boundary Conditions

Artificial boundary conditions are implemented to suppress the flow across the faces between active and inactive cells. The applied boundary condition is similar to an immersed boundary (IB) approach. The IB-method was first introduced by Peskin (1972) and assumes that a body is immersed in the fluid domain, which greatly simplifies the grid generation and grid adaptation for flows with moving boundaries (Mohd-Yusof 1997, Tseng and Ferziger 2003, Mittal and Iaccarino 2005). It is commonly based on a forcing function as additional source term in the governing equations, which ensures the agreement between the computed properties of the flow and the desired properties along the boundary of an immersed body. Extensive overviews of IB-methods are given in Bandringa (2010) and Hylla (2013).

Inactive cells cause unknown fluxes between the active and the inactive domain. The present approach aims at a simple closure for these fluxes. In contrast to classic IB-methods, the implementation of (slip flow) no-flux conditions along these faces provides a straightforward solution, while the accuracy of the geometry and the computational model are deliberately compromised during the contact period. The present concept is based on a few simple changes, viz.

- (a) Suppression of the convective and diffusive fluxes across the faces between active and inactive cells via

$$\dot{v}_F = 0 \quad \text{and} \quad \Gamma_F = 0. \quad (3.12)$$

The additional diffusive flux arising from normal stresses by means of Equation (2.49), cf. Section 2.2.5, is excepted from the suppression.

- (b) Extrapolation of information from the centre of the active cell  $P_A$  to the face  $F$  between an active and an inactive cell. This supports the evaluation of flow gradients in active cells adjacent to inactive cells. The extrapolation follows a zero-order or first-order accurate formula. A zero-accurate formula is given by

$$\phi_F = \phi_{P_A}. \quad (3.13)$$

- (c) The mean value of all  $n_{C_A}$  active neighbour cells is used when reactivating the deactivated cell  $P_{DA}$ :

$$\phi_{P_{DA}} = \frac{1}{n_{C_A}} \sum_{\beta=1}^{n_{C_A}} \phi_{\beta}. \quad (3.14)$$

Since inactive cells are already marked by the overset-grid approach (cf. Section 3.3.1), no further cell identification algorithm is required. Inactive regions have the effect of obstacles. This temporary *solidification* of fluid cells is sometimes appreciated, e.g. to inhibit a mass transport in the centre regime of a gear pump and thereby facilitating a realistic pump characteristic. In other applications, the related flow field obstruction has to be regarded with caution. However, in most engineering cases, the respective predictive errors with regard to the actual simulation objective are negligible if the interest is not on the gap flow. Alternatively, a detailed analysis of the gap flow requires

an improved resolution, e.g. using local grid refinement that would in turn automatically prevent activating the suggested modification.

The temporary shift of small domain fractions from the active to the inactive region and vice versa is afflicted with spurious fluxes, which impose the need for the mass conservation strategy from Section 3.2 in incompressible single-phase flows.

### 3.3.3 Collision of Rigid Bodies

The collision module features a detection strategy and inserts contact forces on the interfering (floating) bodies according to a collision law for non-frictional rigid bodies (Gross et al. 2012, Koblitz et al. 2017). The detection procedure identifies interfering bodies by monitoring the inactive cells and the corresponding partner (*intersection*) grids. The boundary face coordinates of the two involved bodies with the smallest distance to the respective inactive cell are marked as possible contact points. Figure 3.5 shows two interfering bodies ( $L$  and  $R$ ), three inactive cells and the resulting boundary face coordinates marked by red crosses. With the objective of keeping the collision

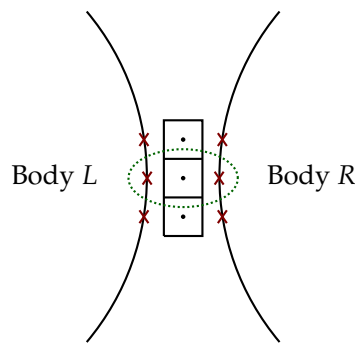


Figure 3.5: Illustration of two interfering bodies ( $L$  and  $R$ ), three inactive cells and the resulting boundary face coordinates marked by red crosses. The shortest link is highlighted in green.

module simple, but generally applicable, contact forces are only applied at the boundary coordinates with the smallest distance to each other (aka. *collision points*; as highlighted in green in Figure 3.5). This constraint allows only one collision per body per time step, but simplifies the collision procedure by avoiding complex equation systems. The contact force is applied normal to the body surface in the contact points. Note that the contact forces are activated in case of coupling problems between overlapping grids, which leads to a premature contact. This drawback of the collision procedure is also resolution dependent.

The applied collision law is based on the assumptions that (a) body deformations can be neglected and (b) the contact forces exceed the hydrodynamic forces to the extent that only the contact forces have to be considered during the collision. The collision behaviour is modelled via a coefficient of restitution  $e \in [0, 1]$ , which is dependent on the material, the geometry and the collision velocity:  $e = 0$  refers to perfect plasticity,

while  $e = 1$  corresponds to perfect elasticity. The collision can be described by a sudden change of the body velocities. After a collision of two arbitrary bodies  $L$  and  $R$ , the entries of the body velocity vector normal to the body surface refer to

$$v_{i,L}^{(n)} = \frac{m_L v_{i,L}^{(n-1)} + m_R v_{i,R}^{(n-1)} + e m_R (v_{i,R}^{(n-1)} - v_{i,L}^{(n-1)})}{m_L + m_R}, \quad (3.15)$$

$$v_{i,R}^{(n)} = \frac{m_L v_{i,L}^{(n-1)} + m_R v_{i,R}^{(n-1)} + e m_L (v_{i,L}^{(n-1)} - v_{i,R}^{(n-1)})}{m_L + m_R}. \quad (3.16)$$

Here,  $m_L$  and  $m_R$  denote the body masses and  $v_i$  refers to the entries of the velocity vector in the contact point of the respective body. The upper indices mark the time level directly before and after the collision. The implemented contact forces  $F_i^C$  and the resulting torque  $T_i^C$  at the centre of gravity can be directly deduced from the normal velocities with respect to the body surface in the contact point and the distance between the contact point  $x_{j,CP}$  and the centre of gravity  $x_{j,CoG}$ :

$$F_i^C = \frac{m (v_i^{(n)} - v_i^{(n-1)})}{\Delta t}, \quad (3.17)$$

$$T_i^C = \epsilon_{ijk} (x_{j,CP} - x_{j,CoG}) F_k^C, \quad (3.18)$$

where  $\epsilon_{ijk}$  denotes the Cartesian coordinates of the permutation tensor. With respect to assumption (b) which states that only the contact forces have to be considered during the collision, the hydrodynamic forces are neglected in the 6DoF solver and are replaced by  $F_i^C$  and  $T_i^C$  when the bodies approach each other ( $v_{i,L}^{(n)} \cdot v_{i,R}^{(n)} < 0$ ). In the case of a contact of  $m_{i,L}$  with a fixed wall, an infinite artificial wall mass is set to calculate the contact forces which yield  $v_{i,L}^{(n)} = -e v_{i,L}^{(n-1)}$ .

The assumption (b) is justified by the investigated parameter range of the applications within this thesis. For spherical particles, the rebound velocity depends on an impact Stokes number which is deduced from the diameter-related Reynolds number  $Re_D$  as well as the density ratio of the body  $\rho_B$  and the fluid  $\rho_F$  (Joseph et al. 2001):

$$St = (Re_D/9) (\rho_B/\rho_F). \quad (3.19)$$

For small values  $St < 10$ , no rebound has been observed in the performed experiments by Joseph et al. (2001). According to their studies, which regard an immersed particle collision in water and glycerol-water mixtures, the coefficient of restitution for dry surfaces can be applied if the Stokes number exceeds 500, i.e. the contact forces supersede the hydrodynamic forces. Since this condition can be regarded as fulfilled for the investigated applications, the use of the dry coefficient of restitution in combination with (b) seems appropriate.

## 4 Analysis of Non-Conservative Inter-Grid Coupling Effects

This chapter is devoted to the analysis of a non-conservative inter-grid coupling. The first section presents the verification and validation of the overset procedure described in Chapter 3 for two- and three-dimensional steady-state flow simulations, while the subsequent examination involves transient flows and/or relative grid motion and reveals the challenges arising from non-conservative interpolation practices. Note that, except for the moving hydrofoil simulations, gravity is neglected in this chapter. Convective momentum transport is always approximated using a monotonicity preserving QUICK scheme and a HRIC scheme is used to approximate convective kinematics in the concentration equation.

### 4.1 Verification and Validation for Steady-State Flows

The verification and validation of the overset procedure is performed by the simulations of a two-dimensional steady-state flow around a circular cylinder embedded in a channel and a three-dimensional lid-driven cavity flow. The cylinder flow has been formerly suggested for code verification studies by Schäfer et al. (1996), while Tang et al. (2003) have used the three-dimensional lid-driven cavity flow to evaluate the influence of different interpolation schemes in the context of overset grids. Both cases involve no grid motion and should prove the accuracy of the baseline overset approach by comparison with literature reported and single-grid results. While Section 4.1.1 shows an extensive analysis of the cylinder flow results obtained with the different mass conservation practices, Section 4.1.2 proves that the overset-grid approach works for three-dimensional applications.

#### 4.1.1 DFG Benchmark Case

The two-dimensional simulation examines the steady, laminar, incompressible flow around a cylinder in a channel, aka. the *DFG Benchmark Case* (cf. Figure 4.1). The upstream end of the channel is the inlet and the downstream end refers to a pressure boundary condition. The centre of the cylinder is arranged a small distance below the channel centre line to enforce an asymmetric flow field. The velocity profile prescribed at the inlet reads

$$u_x = \frac{6\bar{U}}{H^2} \left[ (y + 2D)H - (y + 2D)^2 \right], \quad u_y = 0. \quad (4.1)$$

The diameter of the cylinder is assigned to  $D = 0.1$  m, the channel height refers to  $H = 4.1 D$  and the bulk velocity reads  $\bar{U} = 0.2$  m/s. With a density of  $\rho = 1$  kg/m<sup>3</sup> and a viscosity of  $\mu = 0.001$  Pa s, these values result in a Reynolds number of  $Re_D = 20$ .

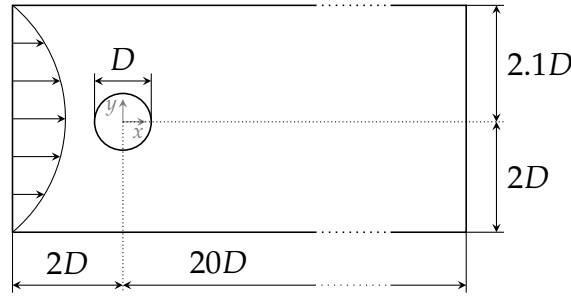


Figure 4.1: Configuration of DFG benchmark case.

Single-grid and overset-grid simulations are performed for three different grid levels, which approximately double the edge resolution as indicated by Table 4.1.

Table 4.1: Total amount of control volumes employed for the single-grid and overset-grid simulations of the DFG benchmark case.

| Grid(s)       | Coarse | Medium | Fine    |
|---------------|--------|--------|---------|
| Single grid   | 18 176 | 72 704 | 290 816 |
| Overset grids | 19 840 | 79 360 | 317 440 |

Figure 4.2 shows the single grid and the overlapping grid arrangement for the coarsest resolution. It demonstrates that the concept of overlapping grids can lead to a better grid quality with respect to cell skewness and orthogonality, see the transition from the O-grid around the cylinder to the Cartesian mesh filling the rest of the domain for the single grid. The cell status attribution of the overlapping grids is depicted in Figure 4.3, the dark grey area represents ignore cells of the background grid. Note that for the sake of clarity, only every second grid line is displayed in Figures 4.2 and 4.3. Identical solver setups and approximation schemes are used for all approaches. Overset-grid simulations are always performed with a second-order simplex interpolation, while assessing the influence of mass conservation practices.

Results obtained for the DFG benchmark case are reported in Figure 4.4 and Figures 4.6 to 4.9. Figure 4.4 compares the predicted lift and drag forces obtained for a single grid with four overset-grid simulation series using the different mass conservation practices from Section 3.2. The simulations refer to the meshes outlined in Table 4.1. The resolution of the corresponding boundaries is identical for the overlapping and the single-grid simulations and the respective near-wall meshes also agree in the vicinity of the cylinder. The discretised shape of the cylinder varies with the refinement level and features variations of the circumference from -0.01% for the coarse mesh to -0.00063% for the fine mesh as compared to the analytical circumference.

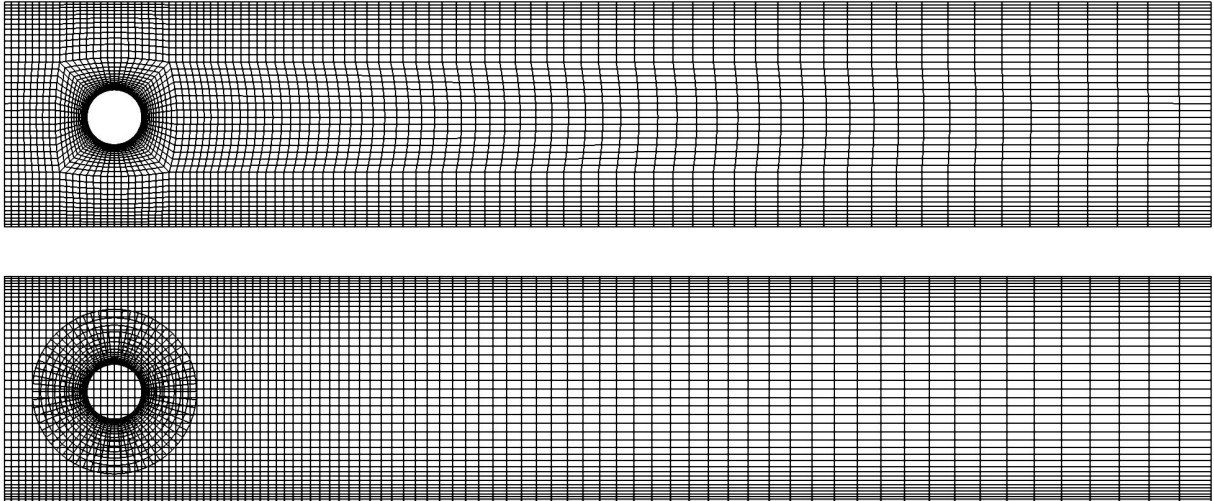


Figure 4.2: Coarse single-grid and overset-grid configuration for the DFG benchmark case. For clarity, only every second grid line is displayed.

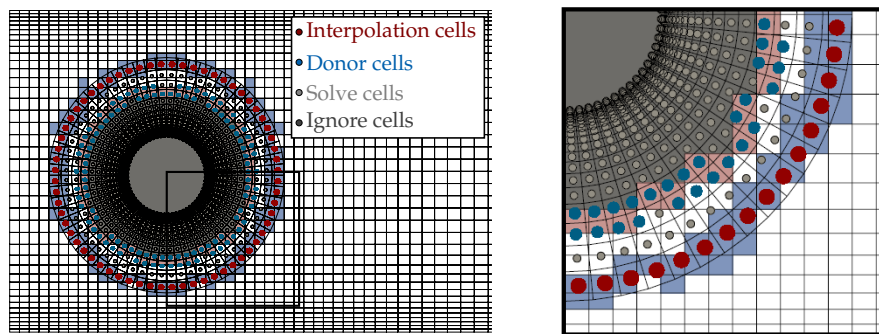


Figure 4.3: Cell status attribution of the overlapping grids (Dots: foreground-grid attribution / Coloured cells: background-grid attribution). For clarity, only every second grid line is displayed. The enhanced view on the right-hand side shows the attribution in the lower right corner of the overlapping region.

The displayed range of the drag forces on the left-hand side of Figure 4.4 agrees with the range of extrapolated results recommended by Schäfer et al. (1996), i.e.  $c_D \in [5.57, 5.59]$ , who compared the data of 17 different software packages each of them using various resolutions. Note that the recommended range of the lift forces  $c_L \in [0.0104, 0.0110]$  was extended to display the results of all grid configurations on the right-hand side of Figure 4.4. The shaded area indicates values which fall out of the recommendations of Schäfer et al. (1996). The recommended ranges cover approximately 0.35% of the expected drag and 5.7% of the expected lift values, whereas results of the present simulations vary only about 0.05% and 1.65% of these values. The force predictions of the four overset-grid simulations are virtually indistinguishable. Using Richardson extrapolation, the predicted lift and drag forces differ slightly between the single-grid ( $c_D = 5.5840$ ,  $c_L = 0.0105$ ) and the averaged overset simulations ( $c_D = 5.5812$ ,  $c_L = 0.0106$ ). The magnitude of the friction forces is approximately half of the pressure

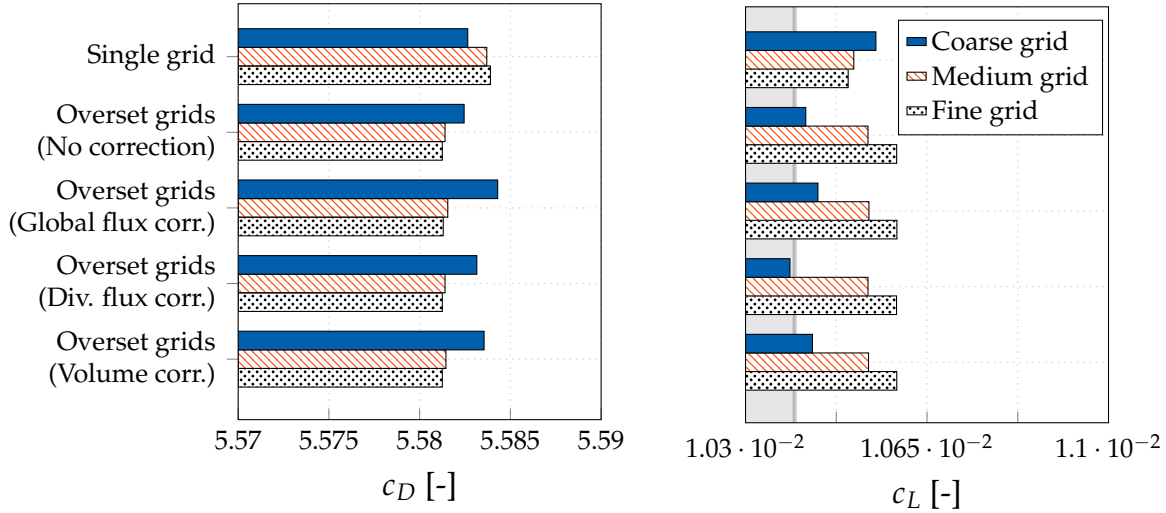


Figure 4.4: Convergence of the predicted drag and lift coefficients obtained with the single and overset grids for the DFG benchmark case (Coarse/medium/fine grids; Table 4.1). The shaded area indicates the values which fall out of the recommendations of Schäfer et al., i.e.  $c_D \in [5.57, 5.59]$  and  $c_L \in [0.0104, 0.0110]$ .

force contribution and the direction of the total force is roughly  $0.1^\circ$  inclined against the horizontal axis.

When attention is given to an analysis of the observed order of accuracy calculated according to Stern et al. (2006), the overset-grid simulations reveal approximately second-order convergence for the magnitude of the pressure (2.2) and friction forces (1.8), disregarding the employed coupling approach. These values are slightly inaccurate due to the unstructured compact interpolation employed to couple the two grids, the unstructured gradient-based reconstruction of remote upstream values for the QUICK-scheme (Jasak 1996) and the inaccuracy introduced by the frequently employed first-order accurate Couette flow assumption for the shear stress evaluation along the wall. Moreover, the convergence rate of the force direction is around 1.0 due to the linear convergence of the discrete shape into a circular shape. The convergence rates of the force magnitudes obtained from the single-grid results are approximately 15% inferior to the overset-grid results due to the mesh distortion during the transition of the grid blocks, which is not seen by the orthogonal meshes of the overset-grid region.

The two overset-grid simulations that do not counteract the mass imbalance, i.e. the uncorrected and the volume corrected approach, show an interesting behaviour regarding the convergence rate. They reveal a much stronger convergence rate for the mass imbalance (around 3.8) than for the flow field. The mass imbalance of all simulations with a flux correction is almost identical and negligible. Figure 4.5 compares the convergence behaviour for the three investigated overset grids with and without the flux correction noted in Equation (3.8). The figure reveals that the convergence behaviour does not improve by the flux correction in such steady grid simulations.

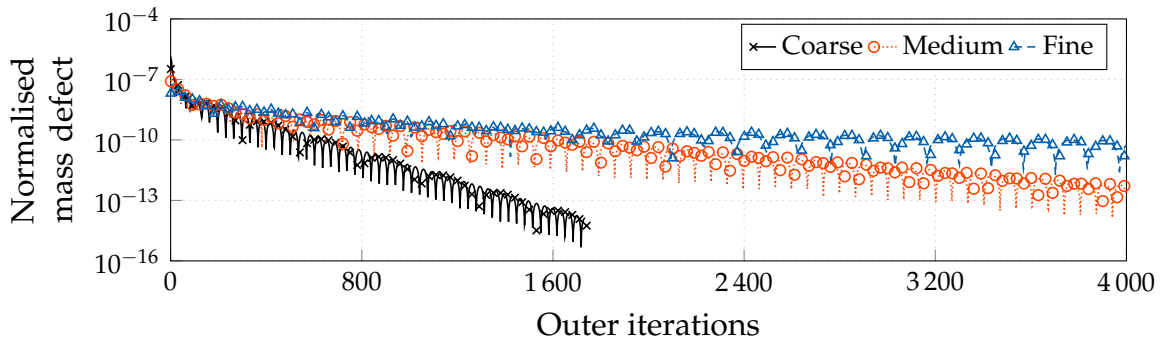


Figure 4.5: Influence of the flux correction on the convergence behaviour for the overset-grid simulations of the DFG benchmark case at  $Re = 20$  (Lines: without flux correction / Symbols: with flux correction). Due to clarity, only every 30<sup>th</sup> symbol is displayed.

Note that one could also make an attempt to investigate the properties of the pressure correction from a more formal point of view, focussing upon the consistency and condition of the equation system. Though, observations have shown that the traceability of the investigated challenges by mathematical approaches is unfortunately limited. It has been proved that (a) the consistency of the equation system is always guaranteed and (b) that the condition number, which is traditionally critical to the pressure correction scheme, does not show any sensitivity to the mass conservation practices – probably because the conservation practices do not directly influence the matrix coefficients but the right-hand side of the equation system. Still, the condition number deteriorates when changing from single-grid to overset-grid schemes due to the asymmetric entries in the equation system.

Due to the high level of predictive agreement between the three suggested mass conservation practices, the remainder of this subsection is confined to the exemplary flux correction outlined in Equation (3.8). Figures 4.6 and 4.7 present the comparison of the pressure fields computed for the different grid refinement levels. Colours and isolines refer to results returned by the overset-grid simulations with the flux correction practice and dots indicate the results of the single-grid simulations. The velocity field and the streamlines predicted on the fine grid are shown in Figure 4.8. Despite some small deviations in the vicinity of the transition between the H- and the O-portion of the single grid, a good agreement between the single-grid and overset-grid results is obtained. The predictive agreement generally improves with the resolution and interpolation-based deficiencies of the overset approach are only observed for the coarse grid – for instance along the upper left edge of the inner grid, as depicted in the enhanced views of the predicted pressure distributions in Figure 4.7.

Figure 4.9 compares the computed pressure distribution for the first- and second-order simplex interpolation scheme using the flux correction practice outlined in Equation (3.8). The predictive difference is marginal and hardly visible, even for the coarse grid simulations on the left-hand side of Figure 4.9.

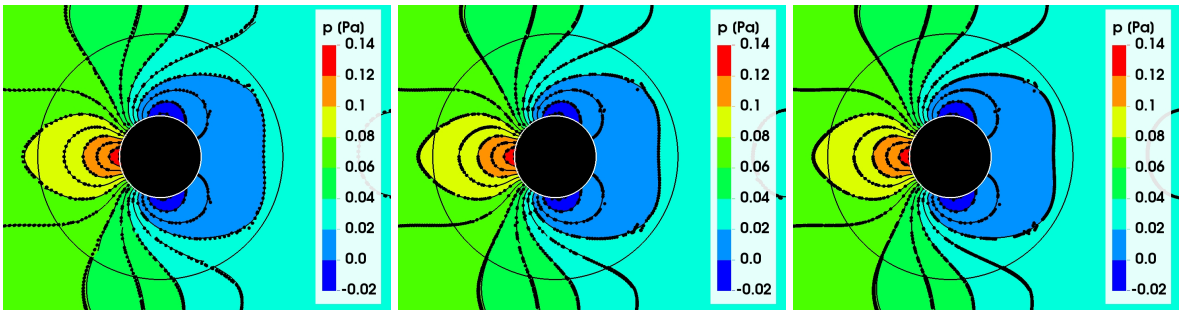


Figure 4.6: Comparison of the predicted pressure distributions on the coarse grids (left), medium grids (centre) and fine grids (right) for the DFG benchmark case (Lines & colours: overlapping grids / Dots: single grid).

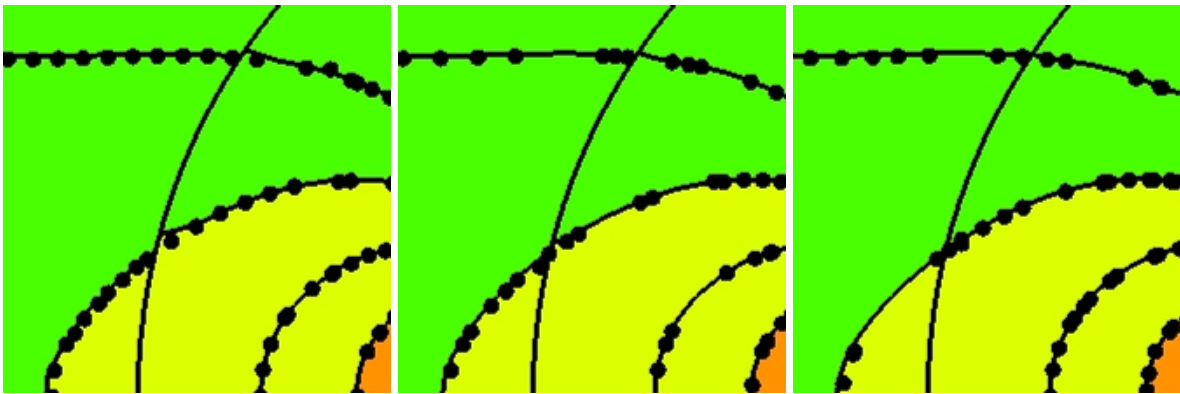


Figure 4.7: Enhanced views of the critical area along the upper left edge of the inner grid for the comparison of the predicted pressure distributions in Figure 4.6 on the coarse grids (left), medium grids (centre) and fine grids (right) for the DFG benchmark case (Lines & colours: overlapping grids / Dots: single grid).

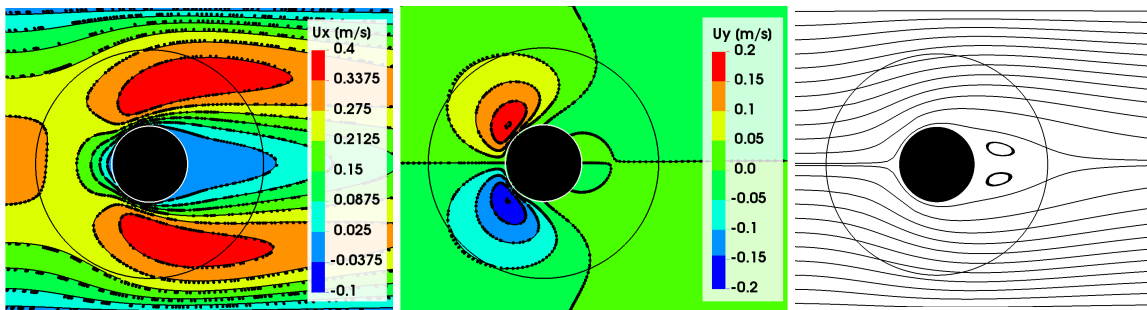


Figure 4.8: Comparison of the predicted horizontal velocities ( $u_x$ , left), vertical velocities ( $u_y$ , centre) and overset streamlines (right) on the fine grid (Table 4.1) for the DFG benchmark case (Lines & colours: overlapping grids / Dots: single grid).

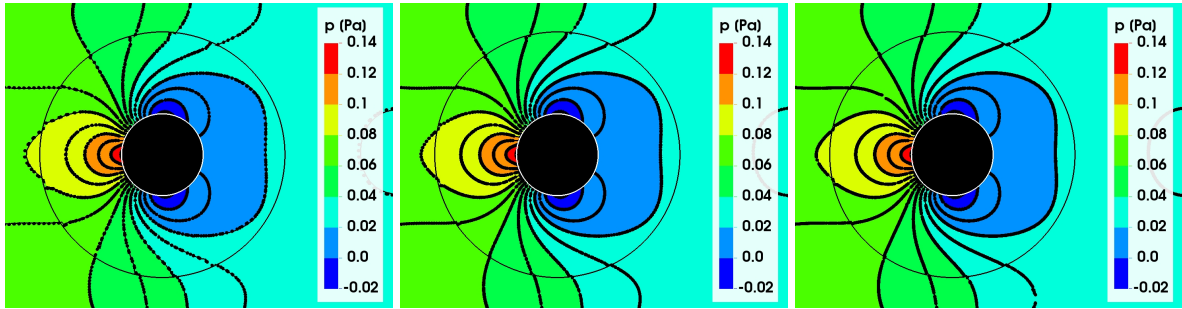


Figure 4.9: Comparison of the predicted pressure distributions using the overset approach on the coarse grids (left), medium grids (centre) and fine grids (right) for the DFG benchmark case (Lines & colours: second-order simplex interpolation / Dots: first-order simplex interpolation).

The results seem to indicate that the predictive accuracy returned by the overset-grid method is generally fair and not substantially deteriorated by non-conservative interpolation practices to couple the grids. The latter is true under the reservation of steady simulations. The computational effort scaled almost linearly with the number of cells, thus the computation time of the overlapping grids case was about 10 % longer than the time needed to run the single-grid case.

#### 4.1.2 Lid-Driven Cavity Case

The three-dimensional simulation of the steady, laminar and incompressible lid-driven cavity flow is based on a cubic cavity with an edge length of  $L = 1$  m and a lid velocity of  $u_x = 0.4$  m/s. The density and viscosity are  $\rho = 1$  kg/m<sup>3</sup> and  $\mu = 0.001$  Pa s, hence the Reynolds number reads  $Re_L = 400$ . The background grid comprises the cavity, employs frictional walls as boundary conditions and can be used for single-grid simulations. The overset-grid configuration is obtained by introducing a second cubic grid with a side length of  $0.55L$ , which is arranged in the centre of the cavity and rotated by  $0.25\pi$  rad in each direction, compare Figure 4.10. The background grid and the foreground grid are discretised uniformly by  $32 \times 32 \times 32$  and  $20 \times 20 \times 20$  cells, which results in cell volumes of approximately  $0.03 \cdot 10^{-3} L^3$  and  $0.02 \cdot 10^{-3} L^3$ .

The verification of the three dimensional overset-grid approach is performed by comparing the predicted pressure distributions and velocities of the single-grid and overset-grid simulations in the plane  $y = 0$  from the present computation to results published by Tang et al. (2003), cf. Figure 4.11. Identical solver setups and approximation schemes were prescribed. The overset grids are coupled using a second-order simplex interpolation and the divergence-based flux correction practice outlined in Equation (3.9). In line with the DFG Benchmark case, the colours and isolines again refer to results returned by the overset-grid approach, while the single-grid results are represented by dots. The obtained results reveal a good agreement, merely the coarse resolution of the grids leads to some small interpolation-based discrepancies at the overlapping interfaces similar to the DFG benchmark case (for instance along the upper left edge of the inner grid, cf. Figure 4.7). The predicted characteristics of the flow field are similar

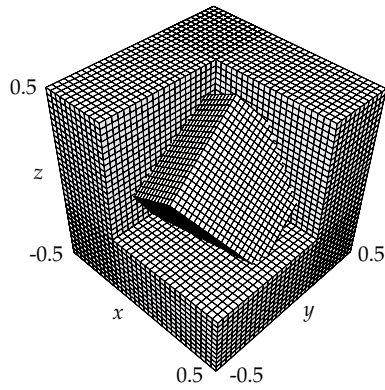


Figure 4.10: Geometry and arrangement of the overlapping grids in the lid-driven cavity case.

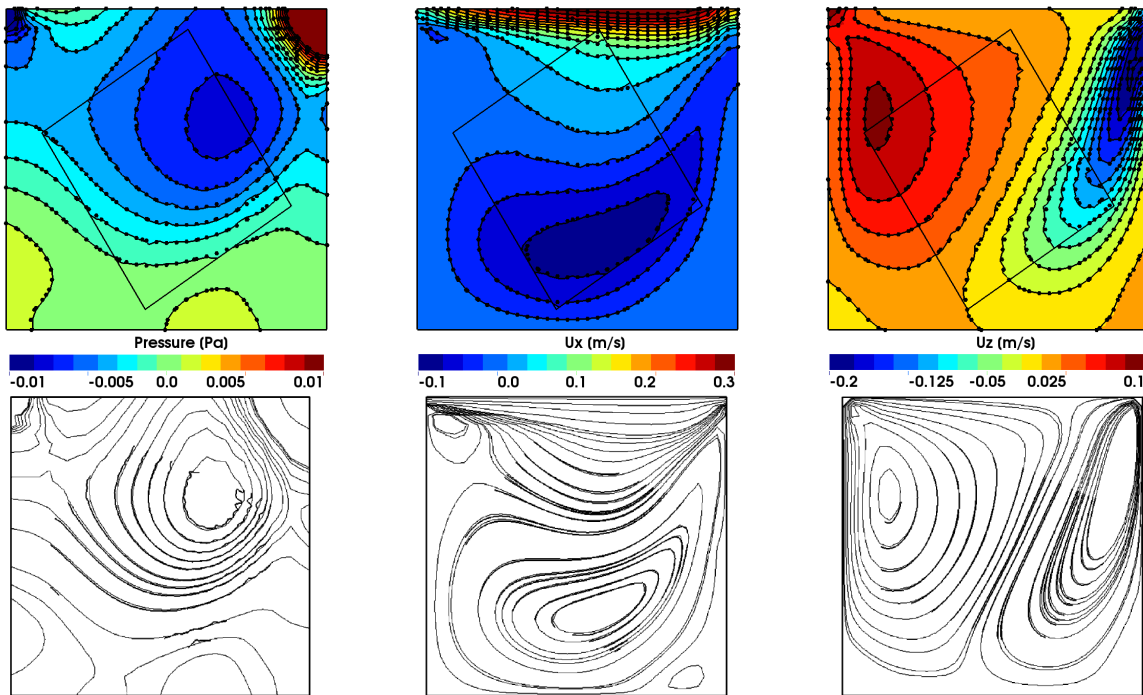


Figure 4.11: Comparison of the predicted pressure distributions (left), horizontal velocities ( $u_x$ , centre) and vertical velocities ( $u_z$ , right) for the lid driven cavity case at the plane  $y = 0$  (Lines & colours: overlapping grids / Dots: single grid) obtained from the present computation (top) compared to results published by Tang et al. (2003) (bottom).

to the ones published by Tang et al. (2003), who stated only isolines for the pressure and the velocities, but no numerical values. Similar to the two-dimensional DFG benchmark case, all other mass conservation practices return similar results and do not reveal any further conclusions.

## 4.2 Transient Flow Studies

The steady flow examples discussed in Section 4.1 did not display a substantial influence of a conservative vs. a non-conservative inter-grid coupling. The following cases involve transient flows and/or relative grid motion and reveal the challenges associated to non-conservative interpolation practices. Whilst the introduction of the mass conservation strategies hardly improves the convergence rate for steady-state flow simulations, their benefits are much more pronounced in transient overset-grid simulations. Especially simulations with moving grids are fairly sensitive to residual mass imbalances, since they feature a dynamic update of the cell status and thus yield transient variations of the mass defect. The arising local mass defects are often masked by the global grid movement and are challenging to control. For instance a change of the donor structure, e.g. by a rotation of the simplex, often results in a different interpolation value that is hard to distinguish from a change of variables due to a transient grid motion, cf. Figure 4.12. The varying mass imbalances influence the current state of

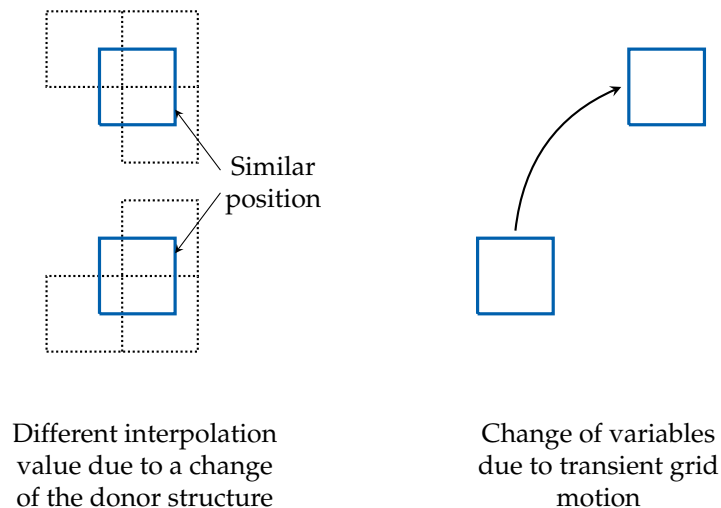


Figure 4.12: Challenge of moving overlapping grids: Different field values may originate from a change of the donor structure or transient grid motion.

the flow field, but are also conserved in the variables of the old time level when the solution advances in time. This particularly refers to solve cells that were assigned to an interpolate status in the former time step and thereby might introduce non-conservative influences from the old time level. It will be seen that these issues promote unfavourable effects, which are augmented with the grid velocity. The following investigation deals with the simulation of a moving hydrofoil in single-phase and two-phase channel flow conditions, a body-force disturbed channel flow and a moving grid configuration of the three-dimensional lid-driven cavity case from Section 4.1.2. Section 4.2.1 examines the pitching hydrofoil and shows an extensive analysis of the coupling effects for a variety of interpolation algorithms and mass conservation practices introduced in Chapter 3. Further, the influences of different grid resolutions and an additional free surface are evaluated. The additional body-force disturbed channel flow and the three-dimensional lid-driven cavity case regard a transient flow with non-moving grids

and a steady-state solution on two coupled grids, which are moving relatively to each other. These cases aim to show the challenges of a non-conservative coupling for the more complex configurations and prove that the grid-coupling approach with mass conservation features works consistently. For clarity, without limiting the generality, only the results of the divergence-based mass conservation practice are presented for the latter simulations. All simulations refer to an implicit second-order accurate three-time level scheme for the approximation of time derivatives.

### 4.2.1 Pitching Hydrofoil

A submerged hydrofoil mounted inside a channel is investigated in different scenarios to evaluate the effects of a non-conservative coupling for moving grid configurations. The two-dimensional geometry is derived from the experiments reported by Duncan (1983) and illustrated in Figure 4.13. The shape of the investigated hydrofoil refers to a NACA 0012 profile with a chord length of  $L = 0.203$  m. The considered physical domain of the channel has a height of  $3L$  and a length of  $14L$ . The left boundary of the channel is the inlet with a prescribed velocity of  $u_x = 0.8$  m/s, while the right boundary is the outlet with a prescribed hydrostatic pressure. Since viscous effects are irrelevant for the present study, the hydrofoil and the upper and lower boundaries are assigned to slip walls. The chord-based Reynolds number is  $Re_L = 1.65 \cdot 10^5$  and effects of turbulence are neglected. The leading edge of the hydrofoil is positioned four chords downstream of the inlet at a height of  $0.91L$  above the channel bottom.

The two overlapping grids, which are employed in the study, are shown in Figure 4.13. The foreground grid is composed from locally refined hexahedrals and captures the flow around the hydrofoil. It is embedded in a uniform hexahedral background grid for the channel flow. Both grids are composed from virtually isotropic cells. The hydrofoil is centred in the foreground grid. This grid spans  $2L \times L$  and is rigidly aligned to the pitching hydrofoil. The background grid is at rest.

The hydrofoil is initiated with zero angle of attack and oscillating with a frequency of  $f = 1$  Hz and an amplitude of  $\hat{\alpha} = 0.1745$  rad around the leading edge. The angle and the corresponding angular velocity are harmonic functions, cf. Figure 4.14. The maximum angular velocity is  $\dot{\alpha}_{\max} = 1.1$  rad/s, which corresponds to a maximum velocity of the foreground grid of  $u_{\text{grid,max}} = 0.35$  m/s.

The employed constant time step reads  $\Delta t \cdot f = 10^{-3}$ . Four different spatial discretisations are regarded to examine the effects of the refinement level and different cell ratios in the overlapping region. The resolution of the hydrofoil employs cell edge lengths of  $\Delta x_{\text{foil}}/L \approx 6.37 \cdot 10^{-3}$  for all four considered foreground grids. The spatial resolution of the overlapping region reads  $\Delta x_c/L = 6.6 \cdot 10^{-2}$  for the coarse foreground and background grids, where  $\Delta x_c$  refers to an edge length of the nearly isotropic cells. Hence, the Courant number of the grid motion reads  $u_{\text{grid,max}} \Delta t / \Delta x_c = 2.6 \cdot 10^{-2}$  for the coarse grid. The finer grids refer to an edge length ratio of  $\Delta x_m / \Delta x_c = 1/2$ ,  $\Delta x_f / \Delta x_c = 1/4$  and  $\Delta x_{vf} / \Delta x_c = 1/8$ .

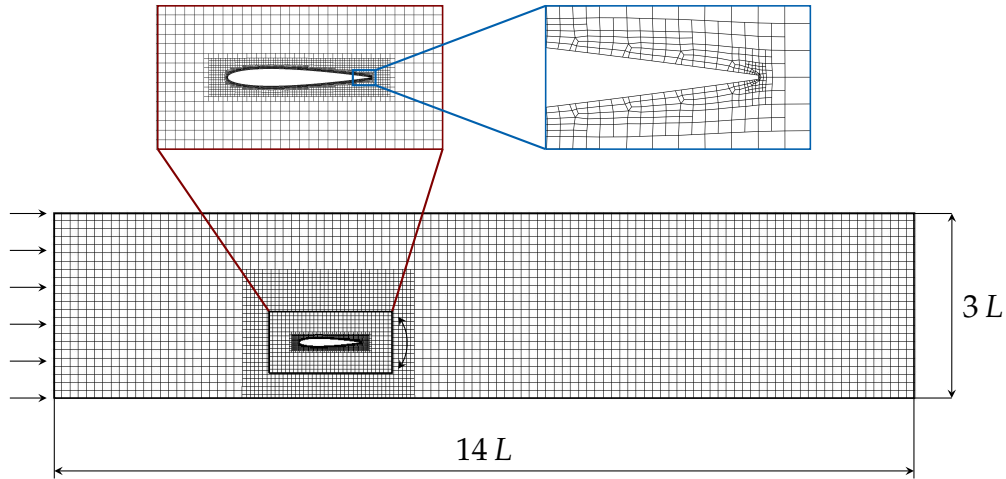


Figure 4.13: Two-dimensional hydrofoil and channel geometry in an overset-grid configuration. The foreground grid and the mesh around the trailing edge are shown as an enhanced view.

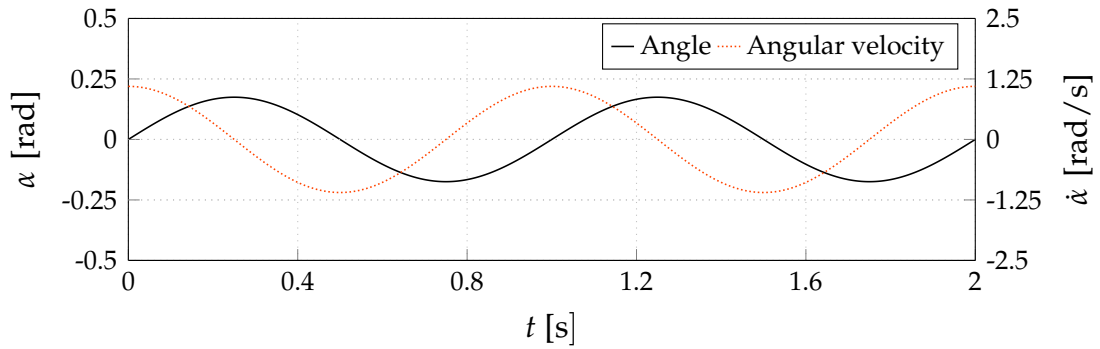


Figure 4.14: Evolution of the angle and the angular velocity of the pitching hydrofoil.

The steady-state overset simulations display benefits in the grid quality and allow grid generation by modular grid components. When attention is directed to moving grids with a non-conservative coupling, difficulties occur for incompressible single-phase flow simulations. The single-phase flow simulations of the oscillating hydrofoil with a non-conservative coupling reveal a fluctuating mass defect over time. The quantification of the mass defect  $\Delta\dot{M}_O$  follows from a non-dimensional parameter, viz.

$$\mathcal{M} = \frac{\Delta\dot{M}_O}{\dot{m}_{\text{inflow}}}. \quad (4.2)$$

The fluctuating mass defect results in a fluctuating pressure. The latter is measured in terms of a second non-dimensional parameter, i.e.

$$\mathcal{P} = \frac{1}{0.5 \rho u_{\text{inflow}}^2} \left( \frac{\sum_{\beta=1}^{n_{c_A}} (p \Delta V)_{\beta}}{\sum_{\beta=1}^{n_{c_A}} \Delta V_{\beta}} - p_{\text{av}} \right), \quad (4.3)$$

where  $\beta$  runs over all active control volumes and  $p_{av}$  denotes the time average of the pressure over the total simulation time, which is determined in a post processing step. To avoid negative pressure, a reference ambient pressure of 1 bar is used.

Since satisfactory results are reported for the combination of non-conservative methods with two-phase flows of air and water (Chung et al. 2007, Carrica et al. 2013), the influence of a free surface with a high density ratio between the two phases and a density ratio of 1.0 is also evaluated. The two-phase flow simulations are based on a submergence of  $0.99 L$  below the still water line. The background grid is refined around the free surface to capture possible effects of the mass defect on the water level, cf. Figure 4.15. All test conditions are summarised in Table 4.2.

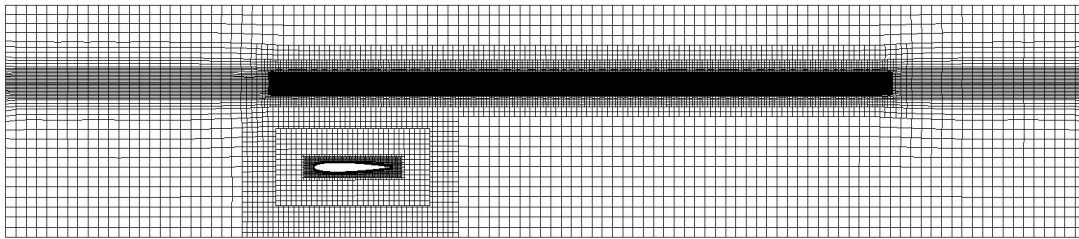


Figure 4.15: Overset-grid configuration for the two-phase flow hydrofoil simulations with a refinement around the free surface.

### Non-Conservative Grid Coupling

The evolution of the two assessed parameters  $\mathcal{M}$  and  $\mathcal{P}$  is shown in Figure 4.16 for the single-phase flow simulation using a second-order simplex interpolation on the coarse grids (Pitching hydrofoil test 1). The mass defect parameter  $\mathcal{M}$  shows an oscillatory behaviour and results in a fairly small maximum of 0.045 %. The maximum negative values of the mass defects occur at simulation times around 0.5 s, 1 s, 1.5 s and 2 s. This coincides with the foil angle being zero and maximum angular velocities of the pitching foil. The maximum positive values of the mass defects are observed at simulation times around 0.25 s, 0.75 s, 1.25 s and 1.75 s, when the foil angle has reached its maximum, while the angular velocities of the foil are equal to zero. The non-dimensional pressure variation  $\mathcal{P}$  hits a maximum of 0.45. This value appears to be much higher than the  $\mathcal{M}$ -value, since small variations of the mass are penalised by large variations of the pressure in incompressible flows. The largest fluctuations occur during the period of negative mass defects, while they converge to zero in between. A Fourier transformation of the time signals of  $\mathcal{M}$  and  $\mathcal{P}$  is displayed in Figure 4.17. The mass defect shows a main frequency of 2 Hz, which matches the occurrence of the maximum angles as well as the occurrence of the maximum angular foil velocities. Further significant peaks occur at 4 Hz, 6 Hz and 7 Hz. The pressure defect parameter shows a main frequency of 1 Hz, which is assumed to be induced by the oscillating motion. Further distinctive fluctuations can be observed up to 100 Hz, while the first frequencies coincide with the frequencies of mass defect peaks.

Table 4.2: Test conditions

| Test    | Pitching | Phases    | Grids        | Interpolation | Conservation |
|---------|----------|-----------|--------------|---------------|--------------|
| default | true (x) | water (w) | coarse (c/c) | simplex (sos) | false (-)    |
| 1       | x        | w         | c/c          | sos           | -            |
| 2       | -        | w         | c/c          | sos           | -            |
| 3       | x        | w         | c/c          | fos           | -            |
| 4       | x        | w         | c/c          | cc            | -            |
| 5       | x        | w         | c/c          | nc            | -            |
| 6       | x        | w         | c/c          | sos           | vc           |
| 7       | x        | w         | c/c          | sos           | gfc          |
| 8       | x        | w         | c/c          | sos           | dbfc         |
| 9       | x        | w         | m/m          | sos           | -            |
| 10      | x        | w         | f/f          | sos           | -            |
| 11      | x        | w         | vf/vf        | sos           | -            |
| 12      | x        | w         | c/m          | sos           | -            |
| 13      | x        | w         | c/f          | sos           | -            |
| 14      | x        | w         | c/vf         | sos           | -            |
| 15      | x        | w         | m/c          | sos           | -            |
| 16      | x        | w         | f/c          | sos           | -            |
| 17      | x        | w         | vf/c         | sos           | -            |
| 18      | x        | w         | m/m          | sos           | dbfc         |
| 19      | x        | w         | f/f          | sos           | dbfc         |
| 20      | x        | w         | vf/vf        | sos           | dbfc         |
| 21      | x        | w         | c/m          | sos           | dbfc         |
| 22      | x        | w         | c/f          | sos           | dbfc         |
| 23      | x        | w         | c/vf         | sos           | dbfc         |
| 24      | x        | w         | m/c          | sos           | dbfc         |
| 25      | x        | w         | f/c          | sos           | dbfc         |
| 26      | x        | w         | vf/c         | sos           | dbfc         |
| 27      | x        | a/w       | c/c          | sos           | -            |
| 28      | x        | w/w       | c/c          | sos           | -            |

Phases: a = air, w = water  
Grids: c = coarse, m = medium, f = fine, vf = very fine  
Interpolation: sos = 2<sup>nd</sup>-order simplex, fos = 1<sup>st</sup>-order simplex, cc = cell cluster, nc = nearest cell  
Conservation: vc = volume correction, gfc = global flux correction, dbfc = divergence-based flux correction

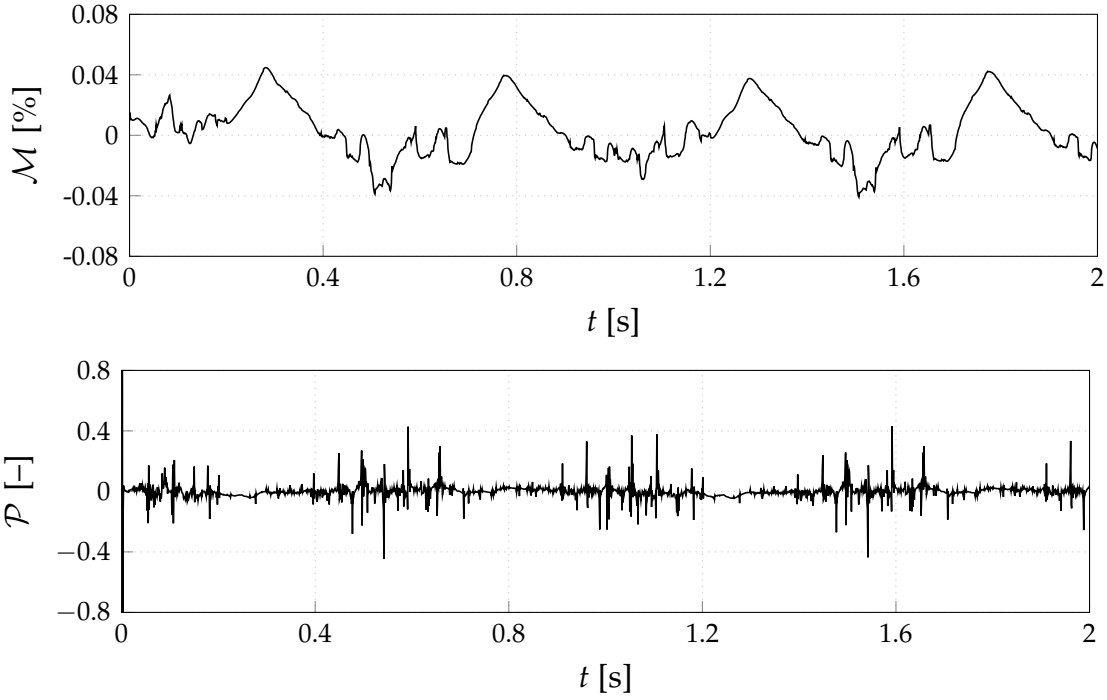


Figure 4.16: Evolution of the mass and pressure defect parameters ( $\mathcal{M}, \mathcal{P}$ ) for a non-conservative second-order simplex interpolation on the coarse grids (Pitching hydrofoil test 1).

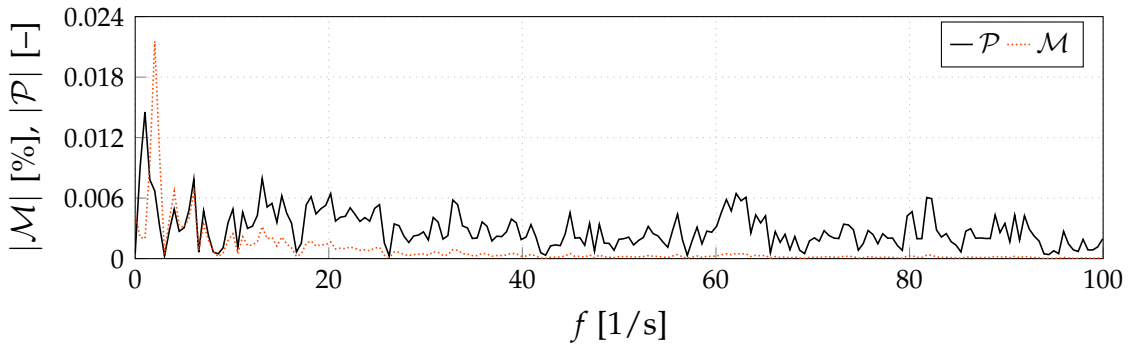


Figure 4.17: Frequencies of the mass and pressure defect parameters ( $\mathcal{M}, \mathcal{P}$ ) for a non-conservative second-order simplex interpolation on the coarse grids (Pitching hydrofoil test 1).

Figure 4.18 presents an enhanced view of the evolution of the pressure defect parameter in the simulated flow field on the left-hand side and the corresponding pressure coefficient

$$c_p = \frac{p - p_\infty}{0.5 \rho u_{\text{inflow}}^2} \quad (4.4)$$

over the relative chord length of the hydrofoil at two subsequent time steps ( $t = 0.542$  s and  $t = 0.543$  s) on the right-hand side. Both pressure distributions show the same characteristics, but indicate a pressure shift.

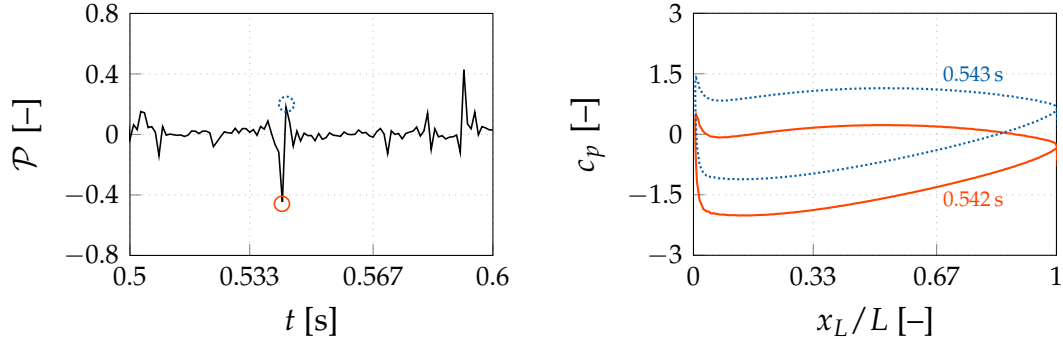


Figure 4.18: Enhanced view of the pressure defect parameter ( $\mathcal{P}$ ) for a non-conservative second-order simplex interpolation on the coarse grids and the corresponding pressure coefficient ( $c_p$ ) over the relative chord length of the hydrofoil at 0.542 s and 0.543 s (Pitching hydrofoil test 1).

Similar to the DFG benchmark test, the simulation of a fixed hydrofoil (test 2) returns a negligible mass defect and vanishing pressure fluctuations, cf. Figure 4.19. The maximum value of mass defect parameter reads  $8.68 \cdot 10^{-3}$  %, while the pressure defect parameter shows a maximum of  $4.54 \cdot 10^{-3}$ , a value that is even smaller.

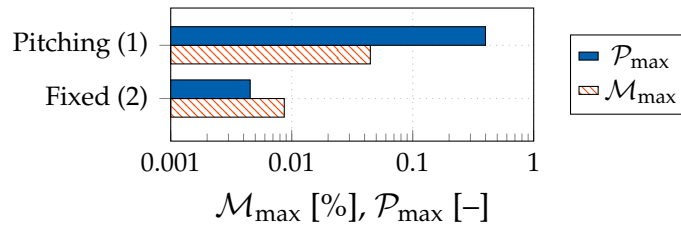


Figure 4.19: Maximum values of the mass and pressure defect parameters ( $\mathcal{M}$ ,  $\mathcal{P}$ ) for the pitching hydrofoil and the fixed hydrofoil on the coarse grids (Pitching hydrofoil tests 1-2).

It is expected that the oscillating motion of 1 Hz can only affect mass and pressure fluctuations of the same frequency directly. Further fluctuations seem to have other reasons. The main technical difference between the simulation of the fixed and the oscillating hydrofoil is the reassignment of the interpolation cells to new donor cells and the allocation as solve or interpolation cell. It is assumed that the transient character of the flow and the cell variations cause the fluctuations by temporal discontinuities.

### Interpolation Accuracy (Test 1, 3-5)

The mass and pressure fluctuations are increased using a less accurate interpolation algorithm, cf. Figure 4.20: The first-order simplex interpolation results in a maximum mass defect of 0.08 % and a maximum pressure variation of 1.43. The interpolation from a cell cluster leads to a maximum mass defect of 0.65 % and a maximum pressure variation of 3.89. The zero-order injection from the nearest donor cell shows a significant increase of the maximum mass defect to 2.75 % and the maximum pressure variation to 13.06. Since unstructured grids only provide information about direct neighbour cells, a simplex-based interpolation algorithm proves the smallest possible pressure fluctuations. Hence, the second-order simplex interpolation algorithm is used for further investigations.

The use of structured grids supports the application of more accurate interpolation methods (Chung et al. 2007, Carrica et al. 2013) and is expected to decrease the non-conservative effects. Due to the advantage in meshing complex geometries with unstructured grids, the pressure fluctuations are rather addressed by additional compensation mechanisms than by enforcing the use of higher-order interpolations.

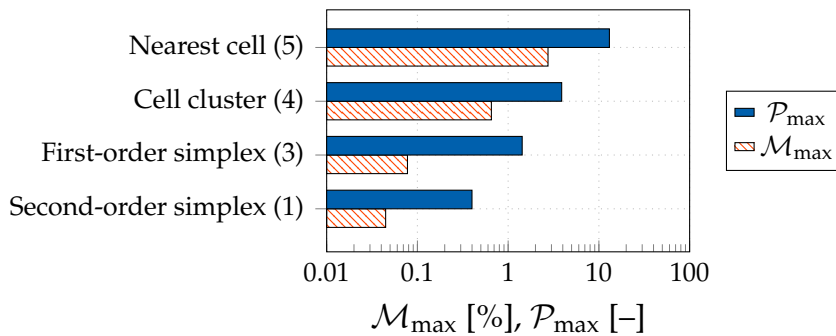


Figure 4.20: Maximum values of the mass and pressure defect parameters ( $\mathcal{M}$ ,  $\mathcal{P}$ ) for different non-conservative interpolation algorithms on the coarse grids (Pitching hydrofoil tests 1, 3-5).

### Grid Coupling with Mass Conservation (Test 6-8)

Application of the mass conservation practices damps the mass defect and the resulting pressure fluctuations significantly. The volume correction approach of Equations (3.5) and (3.6) does not change the amount of the maximum mass defect, since the mass fluxes at the overlapping interfaces are not subject to any correction. The approach suppresses the translation of spurious coupling fluxes into pressure correction and therefore reduces the maximum pressure variation to 0.037. The flux correction methods feature a further improvement of the results. The first flux correction practice of Equation (3.8), which is based on the global mass flux contribution, shows a maximum mass defect of  $0.18 \cdot 10^{-3}$  % and a maximum pressure variation of 0.034. The consideration of the local velocity distribution whilst correcting the mass fluxes provides a more consistent solution regarding the pressure and velocity coupling. Hence, the divergence-based flux

correction of Equation (3.9) hits a maximum mass defect of  $0.19 \cdot 10^{-3} \%$ , but improves the maximum pressure variation to 0.03. Figure 4.21 shows an indicative enhanced view of the mass and pressure defect parameters for all mass conservation practices for a period of 0.2 s ( $t = 1.4 \text{ s} - 1.6 \text{ s}$ ). Results display a substantial reduction of both defect parameters and only marginal differences can be seen between the two investigated flux correction practices. However, the fluctuations of the pressure defect parameter of the divergence-based flux correction are often slightly smaller and therefore, the divergence-based flux correction is used for further analysis.

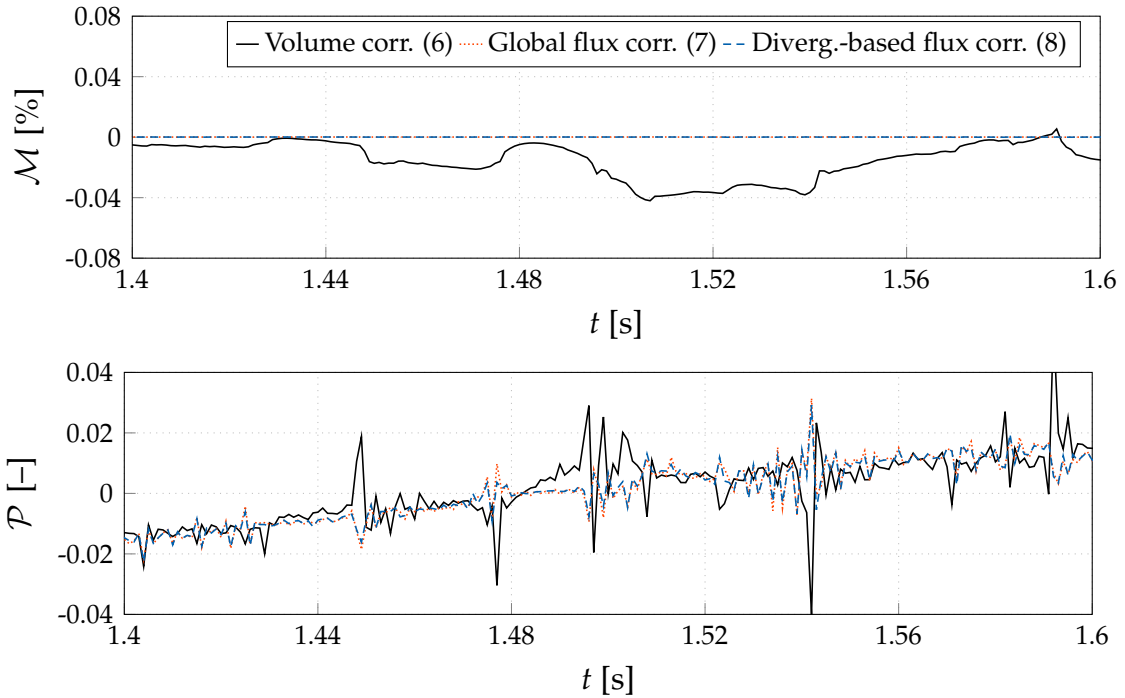


Figure 4.21: Enhanced view of the evolution of the mass and pressure defect parameters ( $\mathcal{M}, \mathcal{P}$ ) for a non-conservative second-order simplex interpolation on the coarse grids with the different mass conservation practices (Pitching hydrofoil tests 6-8).

### Grid Refinement (Test 1, 9-11)

The grid refinement study indicates decreasing mass and pressure fluctuations for an increasing refinement level. The trend is illustrated in Figure 4.22 for the maximum values of the mass and pressure defect parameters. The plotted data for the four refinement levels show a maximum reduction of the mass and pressure defect to  $4.63 \cdot 10^{-3} \%$  and 0.064 for the very fine grids using a second-order simplex interpolation without a mass conservation strategy. This improvement comes up with a reduction of the cell area of the coarse grid  $\Delta A_c$  by a factor of  $\Delta A_c / \Delta A_{vf} = 64$ . However, the least maximum pressure defect is still more than twice the value of the simulation with the divergence-based flux correction on the coarse grid. Since the maximum pressure

variation displays a saturation for an enhanced grid refinement, feasible refinement levels will not reach the accuracy which is provided by the mass conservation practices.

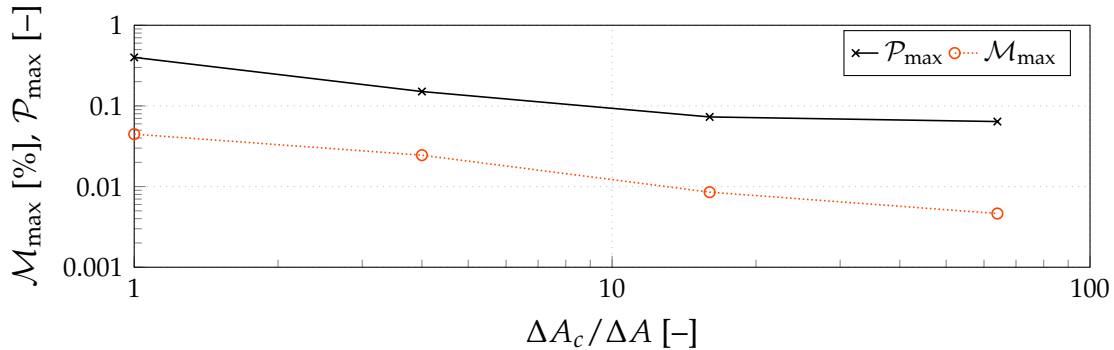


Figure 4.22: Maximum values of the mass and pressure defect parameters for different grid refinement levels using a second-order simplex interpolation without a mass conservation strategy (Pitching hydrofoil tests 1, 9-11).

#### Inter-Grid Cell Ratio in the Overlapping Region (Test 1, 8-26)

The influence of different cell sizes of the interpolation cells and the corresponding donor cells on the mass and pressure defect parameters is shown in Figures 4.23 and 4.24. Two options are evaluated, namely (a) a refinement of the background grid, while the coarse foreground grid is used and (b) a refinement of the foreground grid, while the coarse background grid is used. All results are obtained using a second-order simplex interpolation and diagrammed for simulations with and without divergence-based flux correction.

An exclusive refinement of the background grid without using mass conservation practices shows nearly no change of the maximum mass defect. Though, the maximum pressure variations are decreased from 0.45 to 0.09, which correlates to the trend of the mutual grid refinement. In contrast, an exclusive refinement of the foreground grid increases the maximum mass and pressure defect parameters significantly. The most critical simulation with a cell area ratio of  $\Delta A_c / \Delta A_{vf} = 64$  depicts a maximum mass defect parameter 0.42 % and a maximum pressure defect parameter of 3.3.

Application of the divergence-based flux correction shows an increasing trend of the maximum mass and pressure defect parameters for an increasing cell ratio - independent whether the foreground or the background grid is refined. The simulations with a cell area ratio of  $\Delta A_c / \Delta A_{vf} = 64$  show approximately the same pressure fluctuations as the simulation on the medium grids without application of a mass conservation practice.

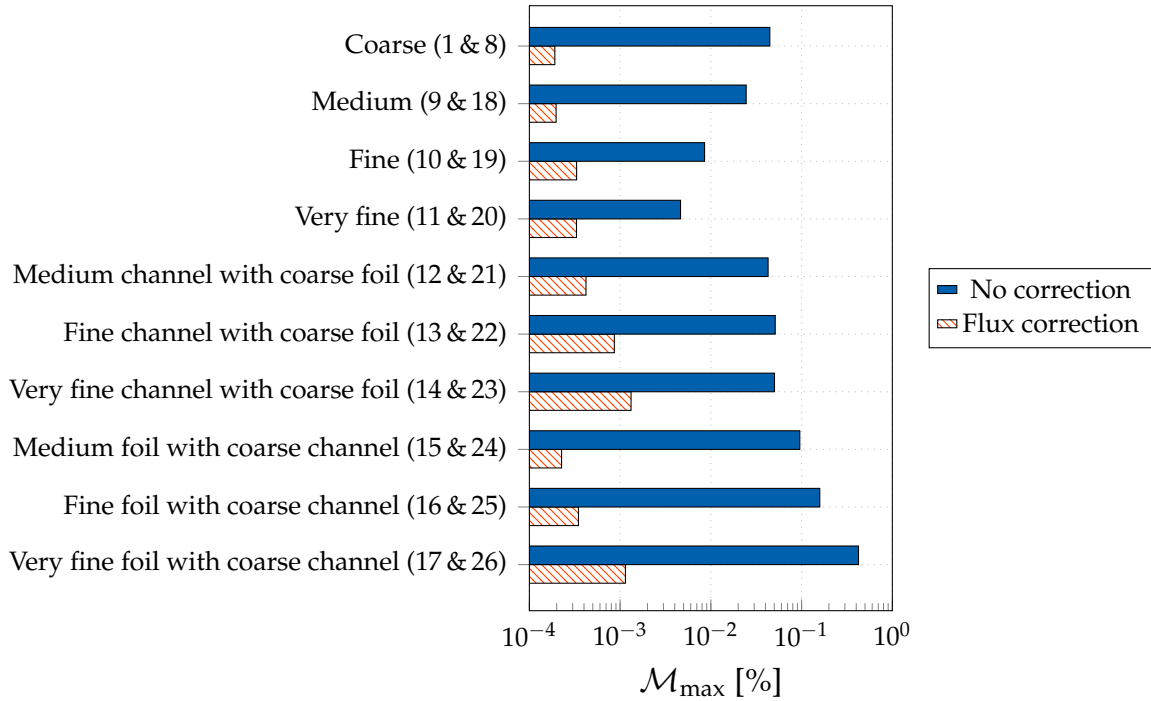


Figure 4.23: Maximum values of the mass defect parameter for different cell ratios between donor and interpolation cells with and without divergence-based flux correction (Pitching hydrofoil tests 1, 8-26).

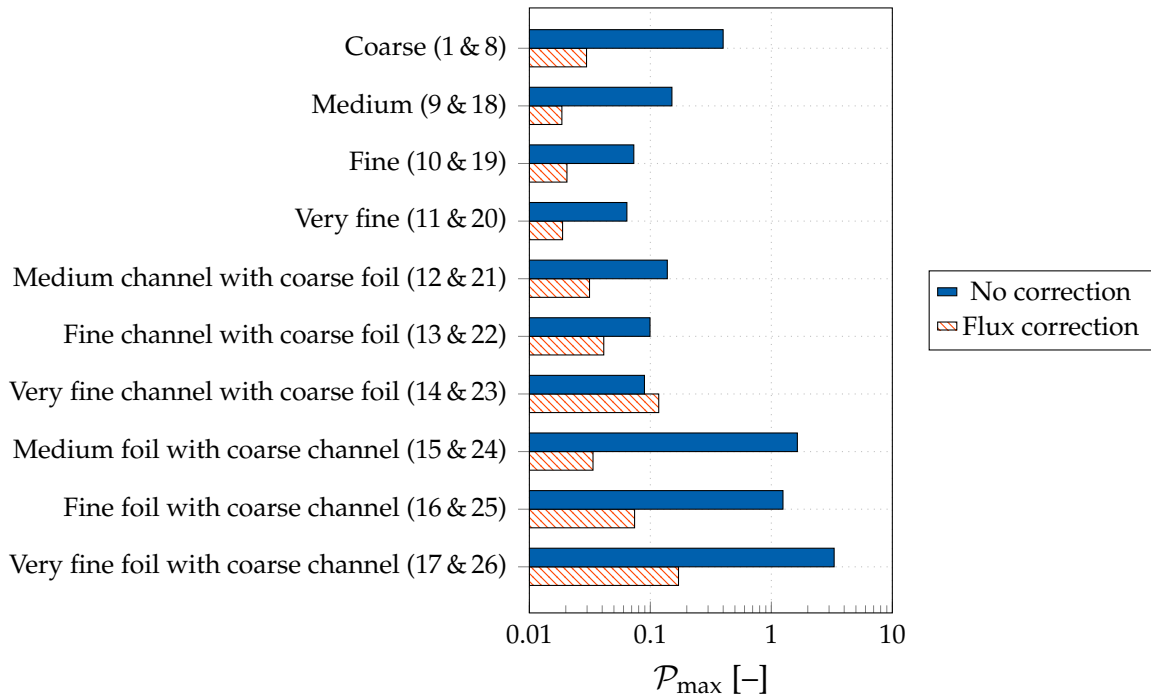


Figure 4.24: Maximum values of the pressure defect parameter for different cell ratios between donor and interpolation cells with and without divergence-based flux correction (Pitching hydrofoil tests 1, 8-26).

**Two-Phase Flows (Test 1, 8, 27-28)**

The influence of a two-phase flow on the mass and pressure defect parameters is displayed in Figure 4.25 for an exemplary time interval from 1.3s to 1.8s. For a better comparison the inflow values of the single-phase flow are used to determine the non-dimensional parameters of Equations (4.2) and (4.3). The uncorrected two-phase flow simulation with air and water shows nearly the same small amount of pressure fluctuations as the single-phase flow simulation with a divergence-based flux correction (Figure 4.25, bottom), even though the mass defect is slightly increased compared to the non-conservative single-phase flow simulation (Figure 4.25, top).

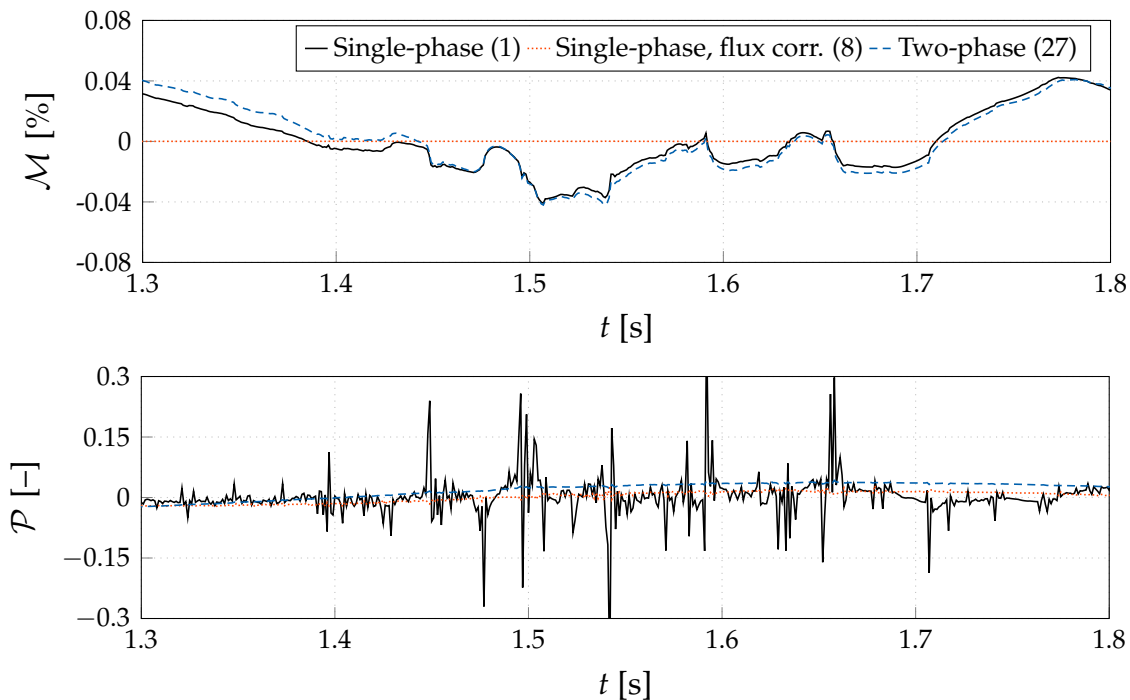


Figure 4.25: Enhanced view of the evolution of the mass and pressure defect parameters ( $\mathcal{M}$ ,  $\mathcal{P}$ ) for single-phase flow simulations with and without flux correction and a two-phase flow simulation of water and air (Pitching hydrofoil tests 1, 8, 27).

Though, a two-phase flow simulation with a density ratio of 1.0 results in the same pressure fluctuations as the non-conservative single-phase flow simulation. This leads to the conclusion that a high density ratio between two phases enables the compensation of the mass defect by an adaptation of the free surface, which results in an intense damping of the pressure fluctuations. Within the given setup, an average elevation of the free surface of  $2.65 \cdot 10^{-7}$  m is required to compensate the maximum mass defect. This marginal elevation of the free surface does not change the flow field in an observable manner, but leads to satisfactory results regarding the pressure. Naval applications are usually based on a two-phase flow simulation with the high density ratio of water and

air, which explains the good results of non-conservative interpolation methods reported in the literature (Chung et al. 2007, Carrica et al. 2013).

### 4.2.2 Body-Force Disturbed Channel Flow

A body-force disturbed channel flow with a non-moving overset-grid configuration is investigated to show the effect of a non-conservative interpolation when coupling multiple non-moving grids in a transient single-phase flow. The two-dimensional channel geometry, the boundary conditions and the spatial resolution of the overlapping region agree with the hydrofoil simulation in Section 4.2.1. The coarse background grid is directly used, while the foreground grid features the same extent as the foreground grid of the pitching hydrofoil simulation but does not include a hydrofoil or any refinement. The longitudinal position of the foreground grid corresponds to the pitching hydrofoil simulation and the transverse extent covers the channel height  $H = 0.61$  m from  $0.220 H$  to  $0.552 H$ . A longitudinal body-force of 100 Newton, constant in time and space, is applied on the foreground grid in the quadratic area of  $(1.413 H, 0.302 H) \times (1.577 H, 0.466 H)$ . The overset-grid configuration of the channel and the applied body-force are pictured in Figure 4.26.

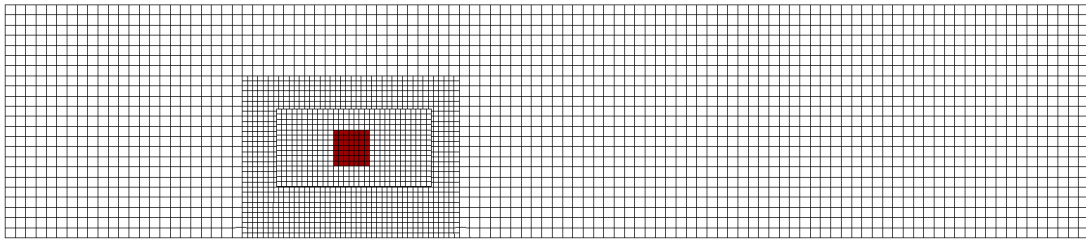


Figure 4.26: Overset-grid configuration of the channel. The foreground grid is positioned in the refined region of the background grid and recognisable by an offset of the grid lines. The area of the applied longitudinal body-force is coloured in red.

The applied constant time step reads  $10^{-3}$  s, which corresponds to a travel time fraction of  $1.31 \cdot 10^{-3} H/u_x$ . The overset grids are coupled using a second-order simplex interpolation and the straight non-conservative coupling is compared to the divergence-based flux correction approach outlined in Equation (3.9). The quantification of the mass and pressure defects follows from the non-dimensional parameters  $\mathcal{M}$  and  $\mathcal{P}$ , cf. Equations (4.2) and (4.3).

The evolution of the mass and pressure defect parameters is shown in Figure 4.27 for the non-conservative coupling with and without flux correction. The lack of a mass conservation practice reveals an oscillatory behaviour of the mass and pressure defect parameters for the transient single-phase flow simulation. The mass defect parameter hits a maximum of 0.755 %, while the pressure defect parameter reaches a maximum value of 2.283 (excluding the first time steps which are needed to obtain a converged pressure level, since the simulation starts with a non-realistic initial flow field at rest).

Application of the divergence-based flux correction practice reveals a maximum mass defect parameter of  $4.66 \cdot 10^{-3} \%$  and reduces the maximum pressure defect parameter to 0.386. The other mass conservation practices show a similar damping behaviour and do not reveal any new conclusions. Without corrections, the defect parameters are augmented by at least one order of magnitude.

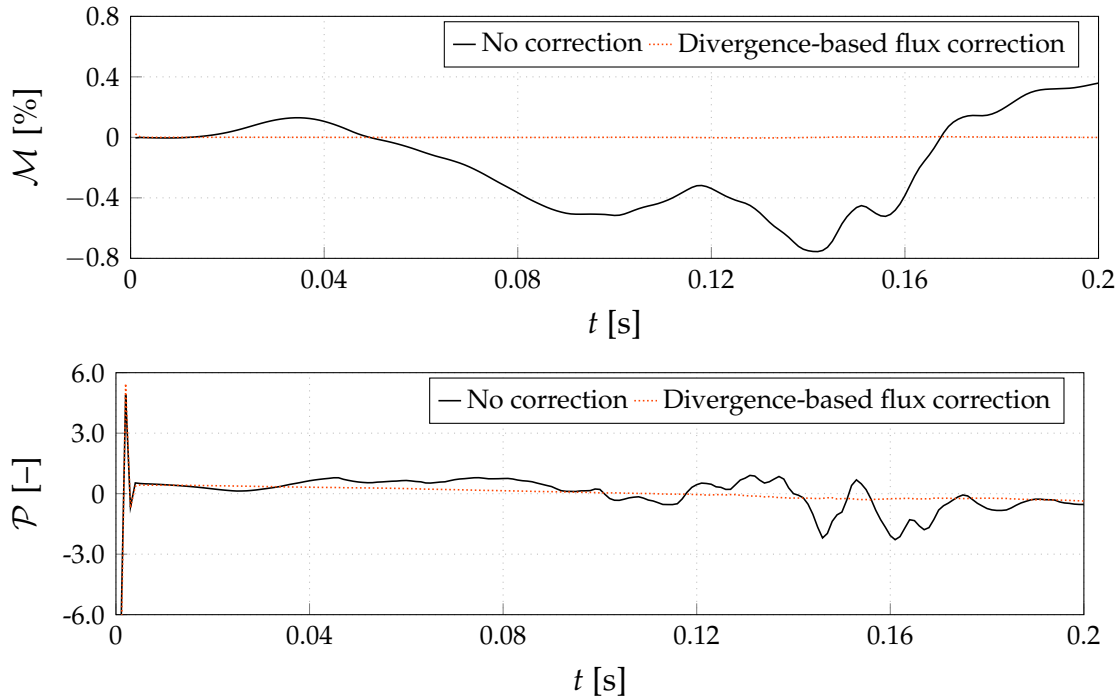


Figure 4.27: Evolution of the mass and pressure defect parameters ( $\mathcal{M}, \mathcal{P}$ ) with and without flux correction.

The results indicate that the simulation of transient flows with non-moving overset grids, e.g. when using immersed boundary methods, shows the same problems as relatively moving grids. Both simulation types reveal a periodic change of the erroneous fluxes and show that these overset-induced mass imbalances cause unrealistic pressure fluctuations if they are not eliminated by mass conservation practices before solving for the pressure.

### 4.2.3 Moving Lid-Driven Cavity Case

A moving grid configuration of the three-dimensional lid-driven cavity case from Section 4.1.2 is investigated in terms of the effects of grids moving relatively to each other in a steady-state flow and the physical reliability of the results with a mass conservation practice. The configuration of the simulation is the same as the configurations of the non-moving single-grid and overset-grid simulations in Section 4.1.2, cf. Figure 4.10. The foreground grid is arranged in the centre of the cavity and initially rotated by  $0.25\pi$  rad in each direction. During the simulation, a rotation of 1 rad/s around each Cartesian

axis is applied. The applied constant time step reads  $\Delta t = 0.01$  s, i.e. a full rotation is discretised by 628 time steps. The overset grids are coupled using a second-order simplex interpolation and the straight non-conservative coupling is compared to the divergence-based flux correction approach outlined in Equation (3.9). The quantification of the mass and pressure defects follows from the adapted non-dimensional parameters  $\mathcal{M}$  and  $\mathcal{P}$ :

$$\mathcal{M} = \frac{\Delta \dot{M}_O \cdot \Delta t}{m_{\text{cavity}}}, \quad \mathcal{P} = \frac{1}{0.5 \rho u_{\text{lid}}^2} \left( \frac{\sum_{\beta=1}^{n_{c_A}} (p \Delta V)_{\beta}}{\sum_{\beta=1}^{n_{c_A}} \Delta V_{\beta}} - p_{\text{final}} \right). \quad (4.5)$$

Figure 4.28 presents the mass and pressure defect parameters with and without flux correction for a simulation time from 2 s to 7 s. While the simulation with a non-

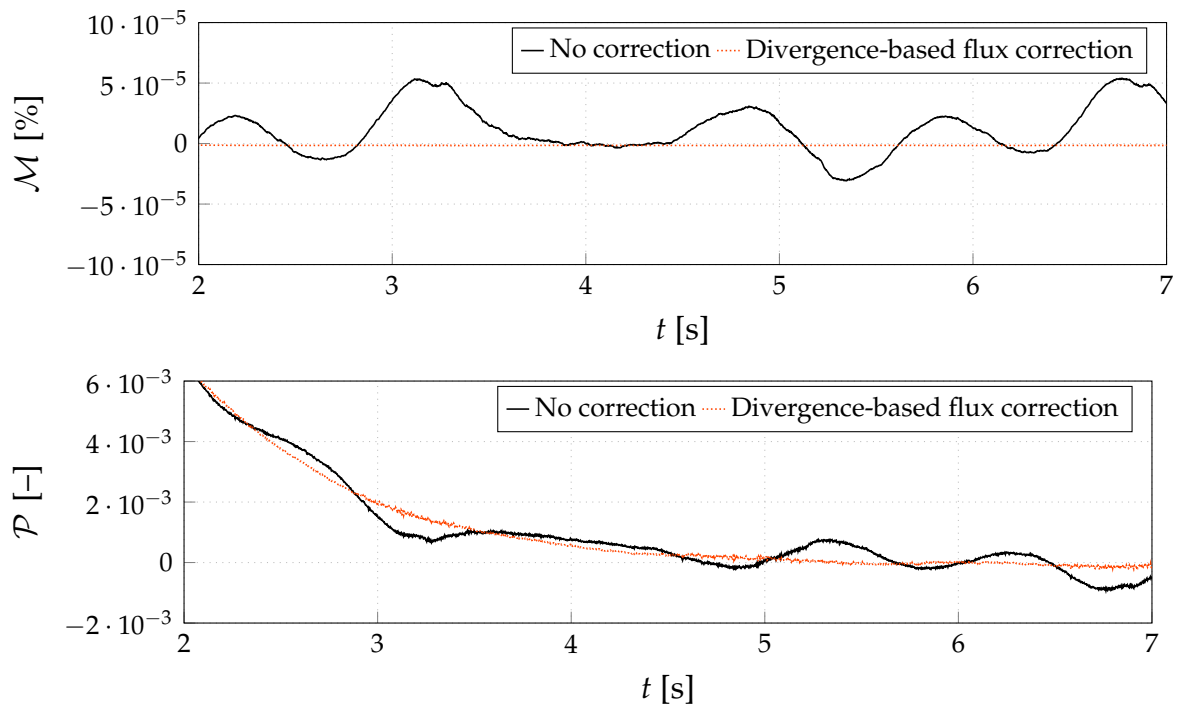


Figure 4.28: Evolution of the mass and pressure defect parameters ( $\mathcal{M}, \mathcal{P}$ ) with and without flux correction.

conservative coupling shows mass and pressure fluctuations in the final steady-state flow field, the results with the divergence-based flux correction feature a steady-state solution even though the foreground grid is relatively moving. This accentuates the sensitivity of relatively moving grids to residual mass imbalances and shows the effectiveness of the implemented divergence-based mass conservation practice. As already shown in Section 4.2.1, all mass conservation practices are very effective and attain similar results. For clarity, only the results of the divergence-based mass conservation practice are presented here.

The final predicted pressure distributions and velocities after a simulation time of 70 s are compared in Figure 4.29 for the divergence-based flux correction to the steady

single-grid results. The colours and isolines refer to the overset-grid approach, while the dots indicate the single-grid solutions. The results show only small discrepancies at the overlapping interface which also occur for the non-moving overset-grid simulation and are explained by the coarseness of the grids. Further small differences are observed at the boundaries and the maximum pressure plateau. Altogether, the values display a fair agreement.

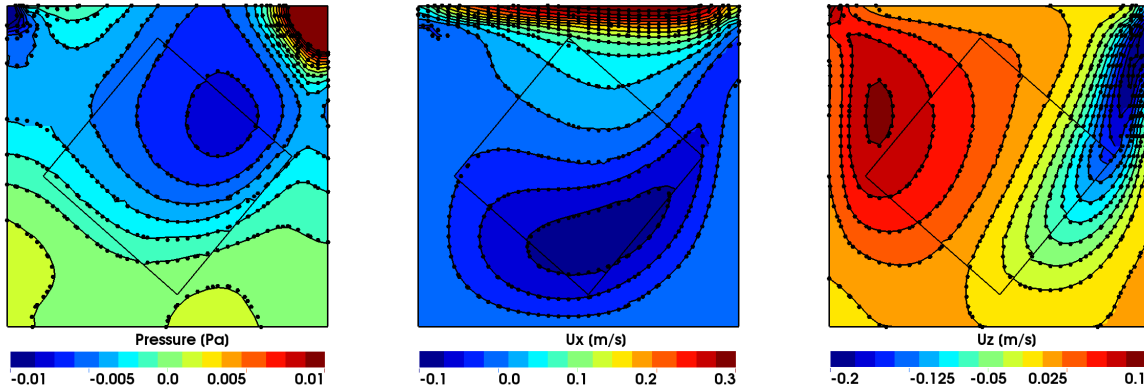


Figure 4.29: Comparison of the predicted pressure distributions (left), horizontal velocities ( $u_x$ , centre) and vertical velocities ( $u_z$ , right) for the lid driven cavity case with rotating grid at the plane  $y = 0$  (Lines & colours: overlapping grids / Dots: single grid).

### 4.3 Summary

The steady-state simulations with non-moving overlapping grids successfully prove the accuracy of the baseline overset-grid approach and show no sensitivity towards the non-conservative coupling. However, mass and pressure fluctuations have been observed for incompressible transient single-phase flows and/or relatively moving grids if no mass conservation practices are used.

Regarding the interpolation methods, the second-order simplex-based scheme proves the best results. However, transient single-phase flow simulations on unstructured grids still show intense pressure fluctuations which require additional conservation mechanisms. Further improvement can be achieved by an increased grid refinement if the cell ratio within the overlapping region is of a similar resolution quality. Immiscible two-phase flows with a high density ratio compensate the mass defect entirely by marginal free surface adaptations. This leads to a smooth pressure evolution and explains the good results of non-conservative interpolation methods within naval applications. Accordingly, the mass conservation practices significantly improve the mass imbalance in transient single-phase flows, which minimises the pressure fluctuations in homogeneous as well as heterogeneous resolution conditions. While all mass conservation practices lead to notable improvements, the divergence-based flux correction, which considers local flow information, slightly proves the best results.

# 5 Verification and Application of the Dynamic Body Contact

This chapter aims to prove and apply the inter-grid coupling for bodies in direct proximity. The verification of the artificial boundary conditions derived in Section 3.3.2 is performed by comparing simulation results obtained with (a) the artificial boundaries and (b) a resolved geometry, studying the two-dimensional wave generation above a submerged box. A two-dimensional simulation series of two colliding circular cylinders is employed to prove the collision procedure introduced in Section 3.3.3. Related applications comprise the simulation of a two-dimensional external gear pump and a three-dimensional generic landslide.

For all simulations within this chapter, convective momentum transport is approximated using a monotonicity preserving QUICK scheme. The concentration transport employs a HRIC scheme. Overset-grid simulations are performed using a second-order simplex interpolation along with the flux-correction approach in Equation (3.8).

## 5.1 Verification of Artificial Boundary Conditions

The two-dimensional incompressible flow around a submerged quadratic box in an open channel is simulated to verify the artificial boundaries derived in Section 3.3.2 for a transient two-phase flow of air and water. The computation considers turbulent effects, but does not involve body motion relative to the surrounding mesh, since any motion can be captured by the applied overset-grid approach. The investigated box is arranged in the water regime of an open channel and has an edge length of  $B = 0.01$  m. Its centre is positioned in the point of origin, as illustrated in Figure 5.1. The domain length reads  $L = 111 B$  and the height of the domain refers to  $H = 21 B$ . The left boundary is the inlet with a constant prescribed velocity of  $u_x = 2$  m/s for both phases and the right boundary is the outlet, where zero normal-gradient conditions are employed. The upper boundary is used to preserve a constant pressure level. The lower boundary is assigned to a slip wall. The initial free-surface height is set to  $5.5 B$  above the point of origin, which corresponds to  $D = 11 B$  above the channel bottom.

To verify the artificial boundaries, two meshes are generated. One mesh refers to the channel with a resolved box and the second mesh just comprises the plane channel. Slip boundaries are used for the resolved geometry and a fictitious box, which is based on the artificial boundary described in Section 3.3.2, is added to the second configuration. The two meshes are each composed of approximately 117 000 cells and refined around the box and the free surface. The box area features virtually isotropic cells with a size of

$0.1 B \times 0.1 B$ . The free-surface area is refined to 86 cells per wave height to accurately capture free-surface effects.

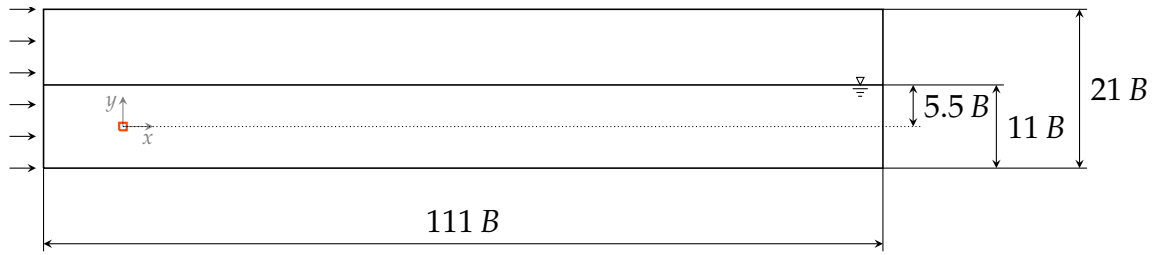


Figure 5.1: Two-dimensional box (coloured in red) and channel geometry for the two-phase flow simulation around a submerged box.

The simulation settings provide a stationary final flow field. The corresponding non-dimensional parameters read  $Re_B = 0.2 \cdot 10^5$  for the box-based Reynolds number and  $Fn_D = 1.925$  for the Froude number, which is calculated based on the water depth. The applied constant time step of  $\Delta t = 0.1 \cdot 10^{-3}$  s corresponds to a travel time fraction of  $0.18 \cdot 10^{-3} L/u_x$  and leads to a maximum Courant number of  $Co = 0.25$ . An implicit second-order accurate three-time level scheme is used to approximate time derivatives. Turbulent effects are considered by the SST  $k-\omega$  turbulence model by Menter (1994) and the gravity acceleration is set to  $9.81 \text{ m/s}^2$  in negative  $y$ -direction.

A comparison of the free-surface elevation  $\eta$  delivered by the resolved geometry and the artificial boundary simulations is shown in Figure 5.2. Both methods result in an identical contour of the free surface between water and air. For clarity, only every 15<sup>th</sup> point is displayed for the artificial boundary method.

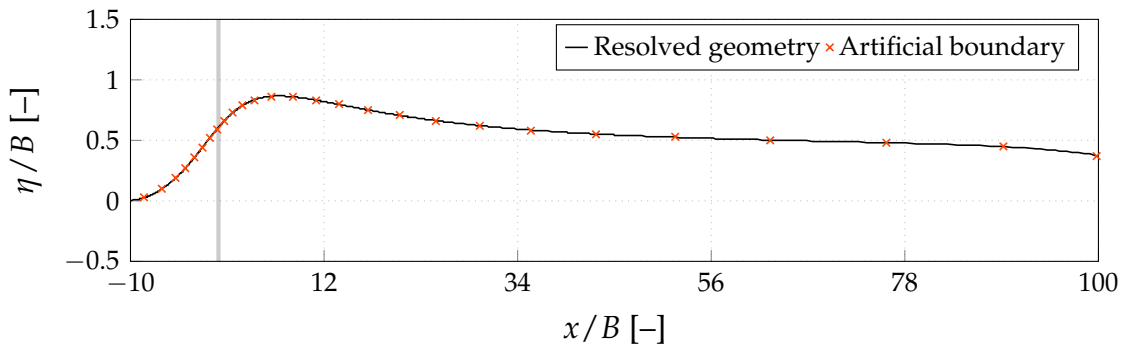


Figure 5.2: Comparison of the surface elevation for the resolved geometry and the artificial boundary simulations. The considered box position at  $x/B = 0$  is marked by the grey line, while  $B$  refers to its edge length/height.

The transient behaviour of the maximum values of the horizontal velocity  $u_x$ , the vertical velocity  $u_y$ , the pressure  $p$ , the turbulent kinetic energy  $k$ , the specific turbulent dissipation rate  $\omega$  and the eddy viscosity  $\mu_t$  within the whole flow field is displayed in Figure 5.3. The final maximum values of the entire region and their deviation are

tabulated in Table 5.1. The final maximum values of the horizontal velocity and the pressure are identical for both methods, although small differences can be observed for the evolution of the pressure. The final maximum values of the other flow properties show tiny differences well below 1 %. The small discrepancies do not influence the overall solution in a critical manner and can be explained by the differences of the equation system.

Table 5.1: Comparison of the final maximum values within the whole flow field of the turbulent free-surface flow around a quadratic box for the resolved geometry and the artificial boundary.

|   | Resolved geometry | Artificial boundary | Deviation |
|---|-------------------|---------------------|-----------|
| Horizontal velocity [m/s]   | 2.504             | 2.504               | —         |
| Vertical velocity [m/s]   | 2.000             | 2.001               | 0.05 %    |
| Pressure [Pa]   | 2708              | 2708                | —         |
| Turbulent kinetic energy [m <sup>2</sup> /s <sup>2</sup> ]            | 0.5857            | 0.5861              | 0.07 %    |
| Specific turbulent dissipation rate [m <sup>2</sup> /s <sup>3</sup> ] | 1476              | 1477                | 0.07 %    |
| Eddy viscosity [Pa s]   | 0.8029            | 0.8028              | 0.01 %    |

Figure 5.4 shows a graphical comparison of the predicted flow fields, e.g. the horizontal velocity, the vertical velocity, the pressure, the turbulent kinetic energy, the specific turbulent dissipation rate and the eddy viscosity, for the resolved geometry and the artificial boundary. Colours and isolines refer to the results returned by the artificial boundary method, while dots indicate the results returned by the resolved geometry. The comparison reveals a fair predictive agreement of both approaches. Non-coupleable cells inside gaps between bodies can thus be replaced by artificial slip walls.

## 5.2 Verification of the Collision Procedure

The verification of the collision procedure introduced in Section 3.3.3 is conducted by a two-dimensional simulation series of two colliding circular cylinders with varying masses, initial velocities and coefficients of restitution. Geometry and arrangement, displayed in Figure 5.5, are derived from the DFG benchmark case (Schäfer et al. 1996), cf. Section 4.1.1. The diameter of the cylinders is  $D = 0.1$  m and the channel refers to a length of  $L = 22 D$  and a height of  $4.1 D$ . The cylinders are arranged  $0.05 D$  below the channel centre line and the initial horizontal distance of their centres amounts to  $1.5 D$ . Since the focal point is the collision simulation, the interference with the flow field shall be negligible. Hence, the fluid is initialised with a density of  $\rho = 0.001$  kg/m<sup>3</sup> and a viscosity of  $\mu = 0.001$  Pa s. A constant inlet velocity of  $u_x = 0.001$  m/s is prescribed at the left boundary of the channel and the downstream end preserves a constant pressure level of 0 bar. The circular cylinders and the upper and lower boundaries of the channel are considered as no-slip walls.

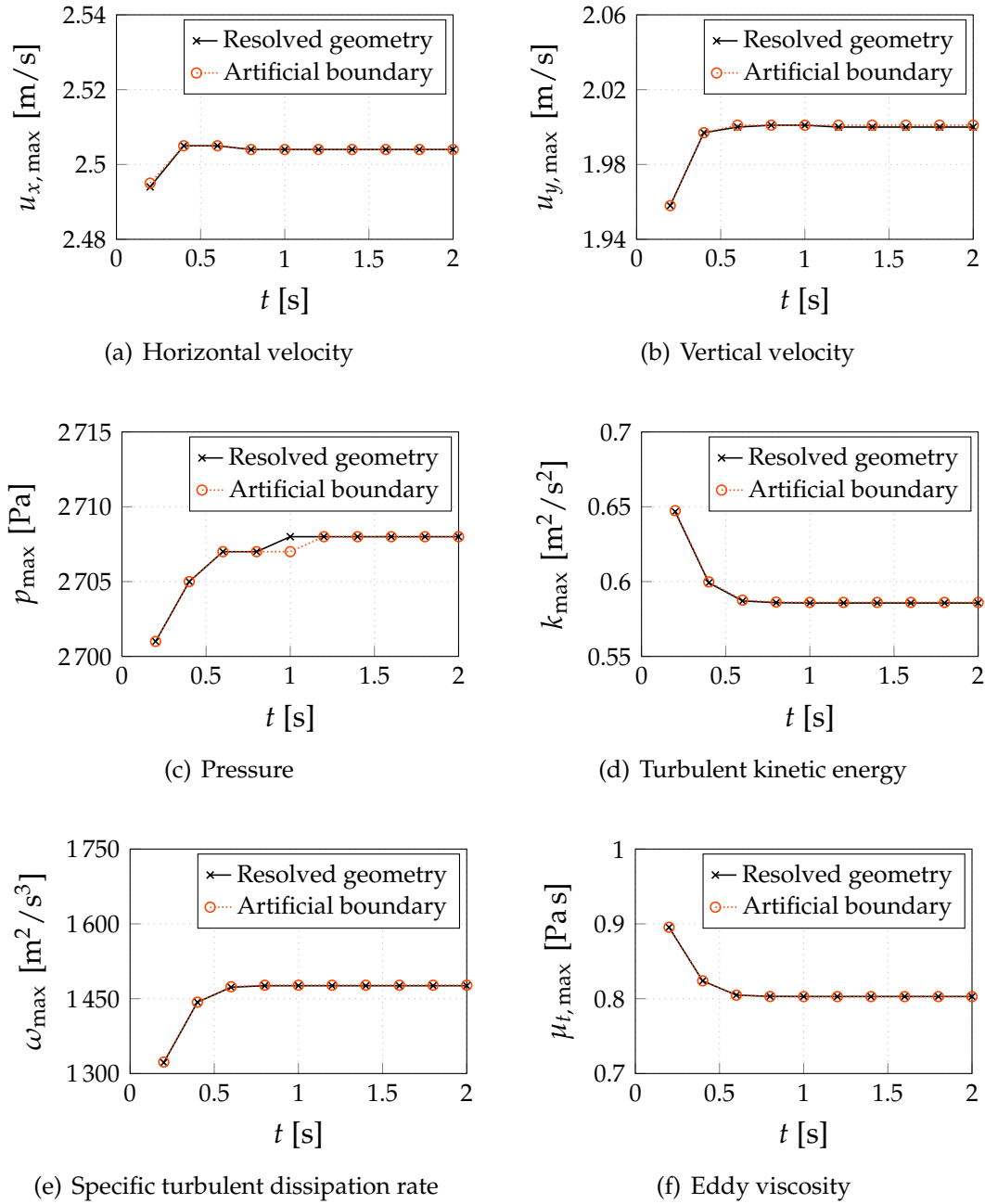


Figure 5.3: Comparison of the convergence of the maximum values of the horizontal velocity, the vertical velocity, the pressure, the turbulent kinetic energy, the specific turbulent dissipation rate and the eddy viscosity within the whole flow field over the simulation time for the resolved geometry and the artificial boundary regarding the two-phase flow simulation around the submerged box.

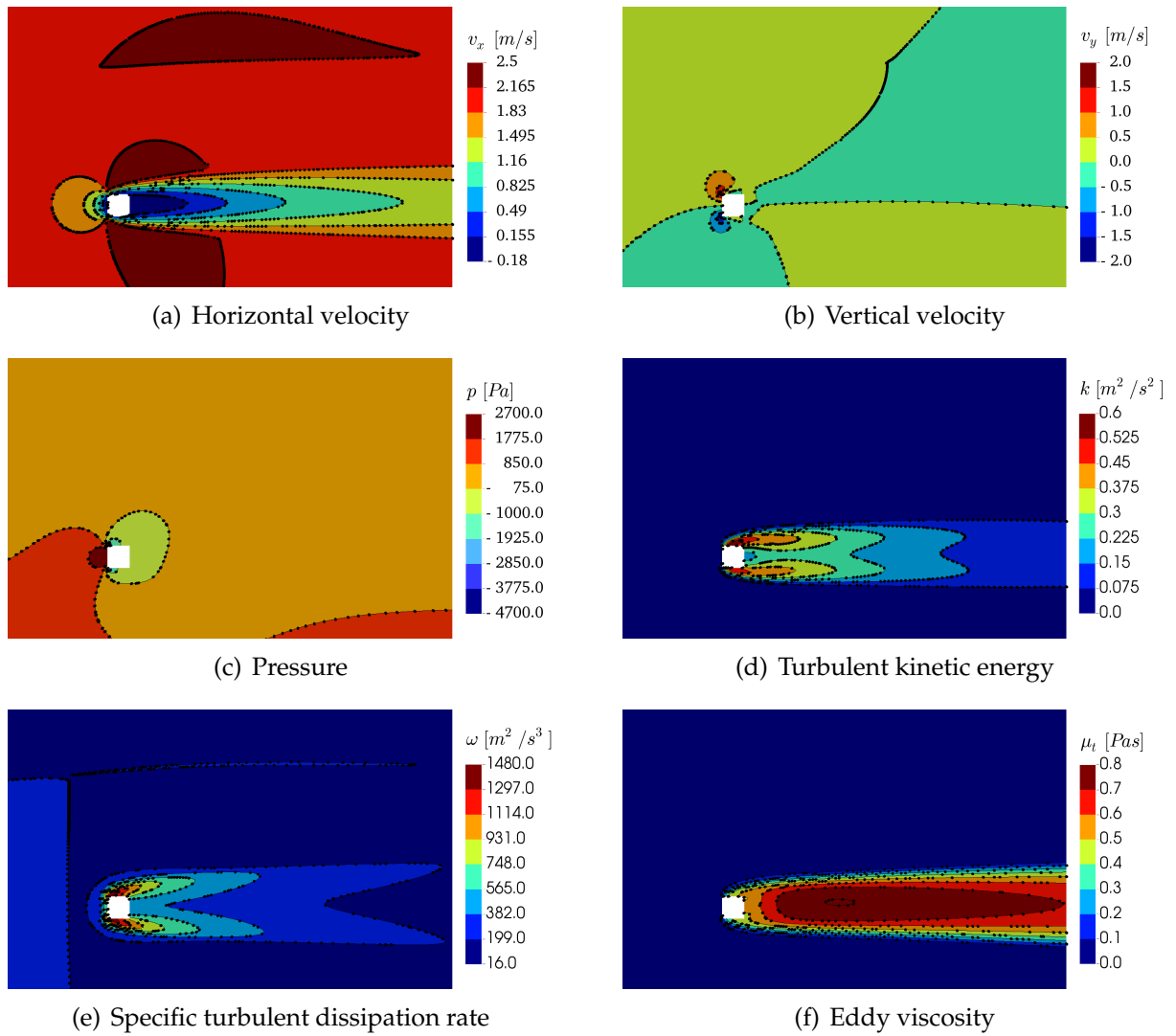


Figure 5.4: Comparison of the predicted final field values of the horizontal velocity, the vertical velocity, the pressure, the turbulent kinetic energy, the specific turbulent dissipation rate and the eddy viscosity for the modelled geometry and the artificial boundary regarding the two-phase flow simulation around the submerged box.

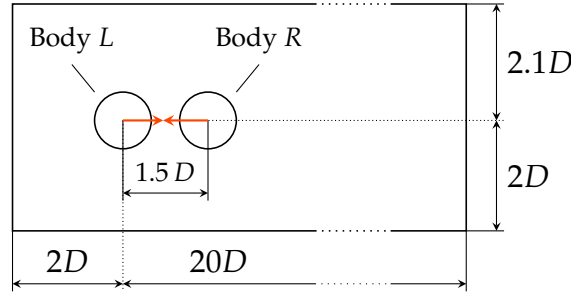


Figure 5.5: Geometry and arrangement of the two colliding cylinders in a channel.

The grid arrangement is composed of three overlapping grids, where the background grid comprises the channel, and each cylinder is embedded in a separate circular foreground grid. Since the focus of the present study is not on the flow field, the resolution of the grids coincides with the coarse grid arrangement of Section 4.1.1. Turbulent effects and gravity forces are neglected. The applied constant time step of  $\Delta t = 0.001$  s corresponds to a travel time fraction of  $0.45 \cdot 10^{-6} L/u_x$ . An implicit Euler scheme is used to approximate time derivatives.

The simulation series refers to nine different combinations involving three coefficients of restitution  $e = [1.0, 0.5, 0.0]$ , two cylinder masses  $m = [1 \text{ kg}, 2 \text{ kg}]$  and three initial body velocities, viz.  $v_x^{(0)} = [1 \text{ m/s}, 0 \text{ m/s}, -1 \text{ m/s}]$ . The employed settings as well as the final velocities and the resulting contact forces are shown in Table 5.2. The numerical results coincide with the analytical values of the collision law from Equations (3.15) to (3.17).

Table 5.2: Settings and results of the simulation series of two colliding cylinders.

| Case | Coeff. of rest. [-] | Mass [kg] |     | Initial vel. [m/s] |      | Final vel. [m/s] |      | Contact force [kN] |
|------|---------------------|-----------|-----|--------------------|------|------------------|------|--------------------|
|      |                     | L         | R   | L                  | R    | L                | R    |                    |
| 1a   | 1.0                 | 2.0       | 1.0 | 1.0                | 0.0  | 0.33             | 1.33 | 1.33               |
| 1b   | 0.5                 | 2.0       | 1.0 | 1.0                | 0.0  | 0.50             | 1.00 | 1.00               |
| 1c   | 0.0                 | 2.0       | 1.0 | 1.0                | 0.0  | 0.67             | 0.67 | 0.67               |
| 2a   | 1.0                 | 2.0       | 1.0 | 1.0                | -1.0 | -0.33            | 1.67 | 2.67               |
| 2b   | 0.5                 | 2.0       | 1.0 | 1.0                | -1.0 | 0.00             | 1.00 | 2.00               |
| 2c   | 0.0                 | 2.0       | 1.0 | 1.0                | -1.0 | 0.33             | 0.33 | 1.33               |
| 3a   | 1.0                 | 2.0       | 2.0 | 1.0                | -1.0 | -1.00            | 1.00 | 4.00               |
| 3b   | 0.5                 | 2.0       | 2.0 | 1.0                | -1.0 | -0.50            | 0.50 | 3.00               |
| 3c   | 0.0                 | 2.0       | 2.0 | 1.0                | -1.0 | 0.00             | 0.00 | 2.00               |

Figure 5.6 depicts snapshots of the colliding circular cylinders for case 2a, e.g. a coefficient of restitution of 1.0, masses of 2 kg and 1 kg and initial velocities of 1 m/s and  $-1$  m/s. The images represent the collision process and illustrate the arising

flow velocities. In addition, the picture in the lower right corner displays the three overlapping grids at the time of the cylinder contact.

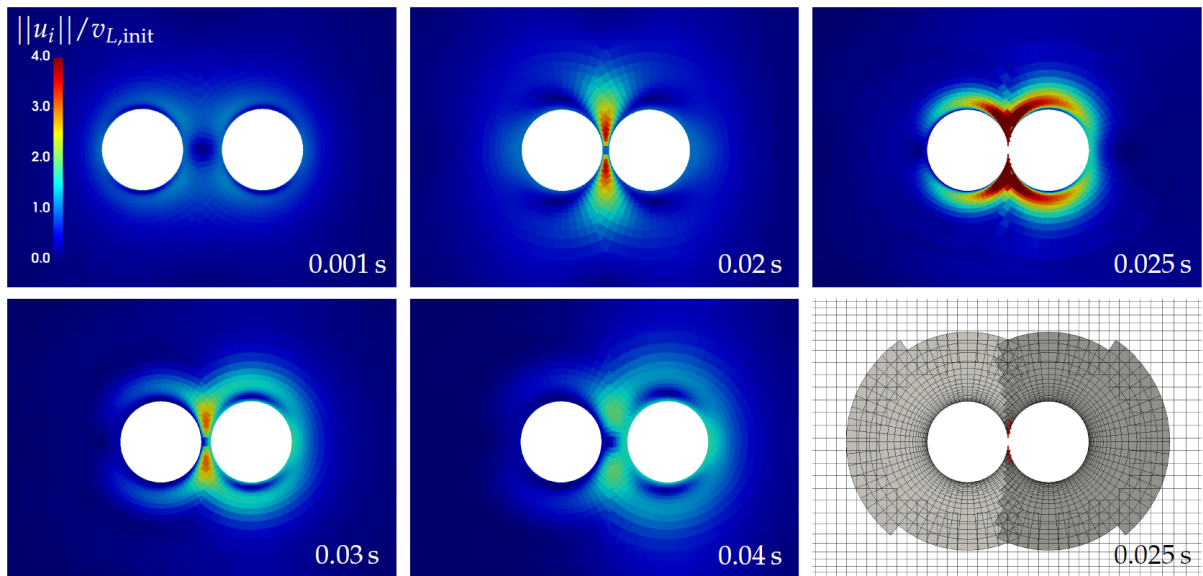


Figure 5.6: Snapshots of the colliding circular cylinders (case 2a). The three overlapping grids at cylinder contact are depicted in the lower right corner.

Figure 5.7 displays the evolution of the horizontal velocity and the total force for the involved cylinders in case 2a. For an impact Stokes number of approximately 14 000, cf. Equation (3.19), the contact forces significantly exceed the hydrodynamic forces. Hence, the collision procedure comes along with a peak of the effective cylinder forces at a simulation time of  $t = 0.025$  s (cf. right-hand side of Figure 5.7), where both cylinders are in contact. This provokes a sudden change of the cylinder velocities (displayed on the right-hand side of Figure 5.7) and successfully prohibits a penetration of the floating bodies.

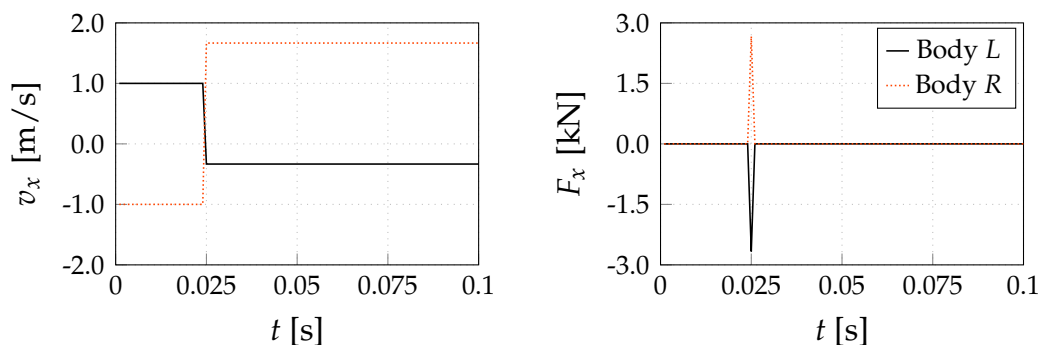


Figure 5.7: Evolution of the horizontal velocities (left) and forces (right) of the colliding circular cylinders (case 2a).

### 5.3 External Gear Pump

External gear pumps are frequently used lubrication pumps. The key benefits are a simple design, a small installation size, low costs and a high reliability in combination with a high supply pressure. Disadvantages follow from the high rotational velocity, which stimulates the appearance of vibration and noise and decreases the pump efficiency. The simulation of the process within an external gear pump is of interest to better understand the operation conditions and to optimise the design.

An example is given in Figure 5.8, which shows a schematic representation of an external gear pump. It consists of two counter-rotating gears, which transport fluid within the outer open space between the teeth and the gearbox. In the centre part, the free space is significantly reduced by the interlocking teeth. This inhibits the mass transport in the centre regime and leads to an increased pressure at the outlet of the pump. Due to a significant pressure jump between the suction and the pressure side, which often amounts to an order of 10 bar, it is essential to model the gear contact and thus prevent a non-realistic backflow.

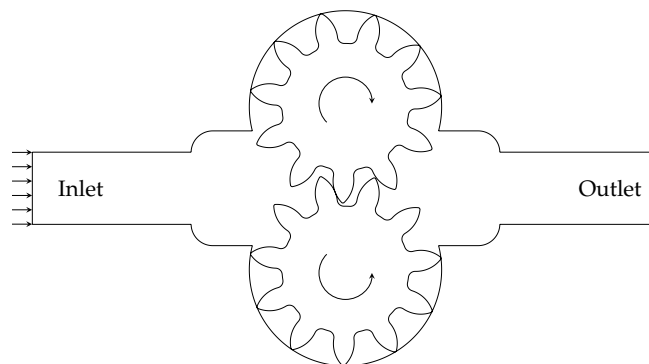


Figure 5.8: Schematic representation of an external gear pump. The gear contact in the centre part is essential to inhibit a leakage between the high-pressure outlet section and the low-pressure inlet section.

The revolutionary motion of the gears involves significant changes of the grid connectivity and demands for a well-working grid update strategy. First numerical studies of external gear pumps introduced a new mesh for each time step (Houzeaux and Codina 2003, Vande Voorde et al. 2004) or applied a remeshing method in combination with a mesh deformation strategy (Strasser 2007, Kim et al. 2007, Yazdani and Soteriou 2014, Yazdani et al. 2015). Castilla et al. (2010) employed a combined grid update strategy using ten predefined meshes for one revolution and adapting these grids to intermediate positions. The common assumption is based on a gap between the gears. Though, Houzeaux and Codina (2003) followed the assumption that no fluid flow occurs in the intersection zone of the teeth and merged both gear geometries within each time step and Castilla either introduced a small additional wall (Castilla et al.

2010) or an enhanced viscosity between both gears (Del Campo et al. 2012, Castilla et al. 2015). Vacca and Guidetti (2011) as well as Devendran and Vacca (2013) applied a lumped parameter model regarding each enclosed volume of the external gear pump separately. The pressure in each considered volume follows from a combined fluid state equation and the mass conservation law, viz.  $p = f(V, \dot{m})$ . More recently, Qiu et al. (2015) simulated two interlocking gears with a marker and cell method and Yoon et al. (2017) numerically investigated a three-dimensional external gear pump by using an immersed solid approach. These strategies feature the advantage that a consistent mesh can be used for the complete simulation, while specific fluid areas are marked as solid to represent the gear. While no contact treatment is mentioned by Yoon et al. (2017), Qiu et al. (2015) introduced a special contact procedure using additional pressure degrees of freedom on the solid boundaries of interacting bodies to provide forces within thin or vanishing gaps. Within this thesis, the enhanced overset-grid coupling approach for bodies in direct proximity, which facilitates a dynamic contact, will be used to examine an external gear pump.

While most studies on external gear pumps did not publish information on the applied pump geometry, Castilla et al. (2008) refer to the pump 1PLA44 by Pedro Roquet and provide an approximate geometry of the counter-rotating gears and the surrounding gear box (Castilla et al. 2010). Almost all geometric pump properties and operating conditions of the present study are taken from Castilla et al. (2010) or refer to their studies. Since the exact pump geometry has not been provided, few assumptions as well as compatibility conditions are introduced and lead to the examined spur gear geometry listed in Table 5.3. Note that two identical gears have been arranged in the gear box, which is depicted in Figure 5.9. The suction chamber (left-hand side in Figure 5.9) and the pressure chamber (right-hand side in Figure 5.9) follow an identical design. The operating conditions are summarised on the bottom of Table 5.3.

Table 5.3: Gear geometry and operating conditions.

|                                   |         |
|-----------------------------------|---------|
| Outer diameter of the gears       | 53.3 mm |
| Distance between the gear centres | 45.1 mm |
| Height of the gears               | 36.0 mm |
| Number of teeth                   | 11      |
| Pressure angle                    | 20°     |
| Pitch diameter per tooth          | 4.1 mm  |
| Backlash                          | 1.0 mm  |
| Input gauge pressure              | 0 bar   |
| Output gauge pressure             | 10 bar  |
| Rotational velocity               | 472 rpm |

Castilla focussed on the suction chamber of the external gear pump. His first investigation provided experimental Time Resolved Particle Image Velocimetry data (Castilla et al. 2008, Ertürk 2008). The subsequent flow rate study of the inflow – with and without gear contact – highlighted the importance of the gap closure (Castilla et al.

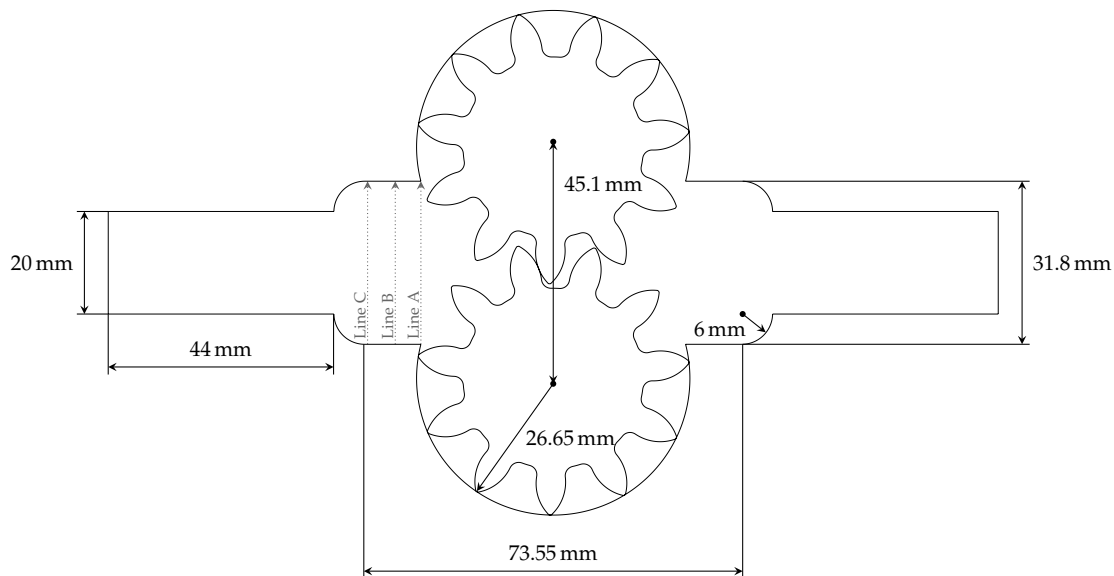


Figure 5.9: Dimensions of the gear box. In- and outlet chamber are symmetrically designed. Lines A, B and C refer to evaluation locations which are positioned at 60.77 mm, 55.77 mm and 50.37 mm from the inlet.

2010). Further examinations of the pump showed cavitation influences (Del Campo et al. 2012) and three-dimensional effects (Castilla et al. 2015). Within this section, the study of the inflow will be used to validate the enhanced overset-grid coupling approach for bodies in direct proximity which allows gear contact. All comparative results refer to Castilla et al. (2010).

Following Castilla's examinations, the simulation refers to the working fluid of oil, i.e.  $\rho = 885 \text{ kg/m}^3$  and  $\mu = 0.028 \text{ Pa s}$ . The pressure difference between the inlet and the outlet reads 10 bar, which is imposed by two pressure boundaries at the respective inlet and outlet ends of the domain. No compressibility or gravity are considered in the present flow model. Since Castilla reports turbulent structures within the inflow chamber, the SST  $k-\omega$  turbulence model by Menter (1994) is applied using a low-Reynolds wall boundary condition. The simulation is advanced by a constant time step of  $\Delta t = 0.01 \cdot 10^{-3} \text{ s}$ , which corresponds to approximately 12 700 time steps per gearing cycle. About three gearing periods are simulated, though, it has been proved that also more gearing periods show a cyclic behaviour. An implicit Euler scheme is used to approximate time derivatives.

Three overlapping meshes are used to simulate the external gear pump: One grid covers the complete simulation domain of the gearbox, and two similar grids are employed around the gears to facilitate the rotational motion. The dimensions of the background grid are specified in Figure 5.9. A detail of the employed meshes is depicted in Figure 5.10. The picture shows the active cells within the inner part of the suction chamber and the critical central region with the interlocking teeth. The mesh is refined around the teeth and in the overlapping region.

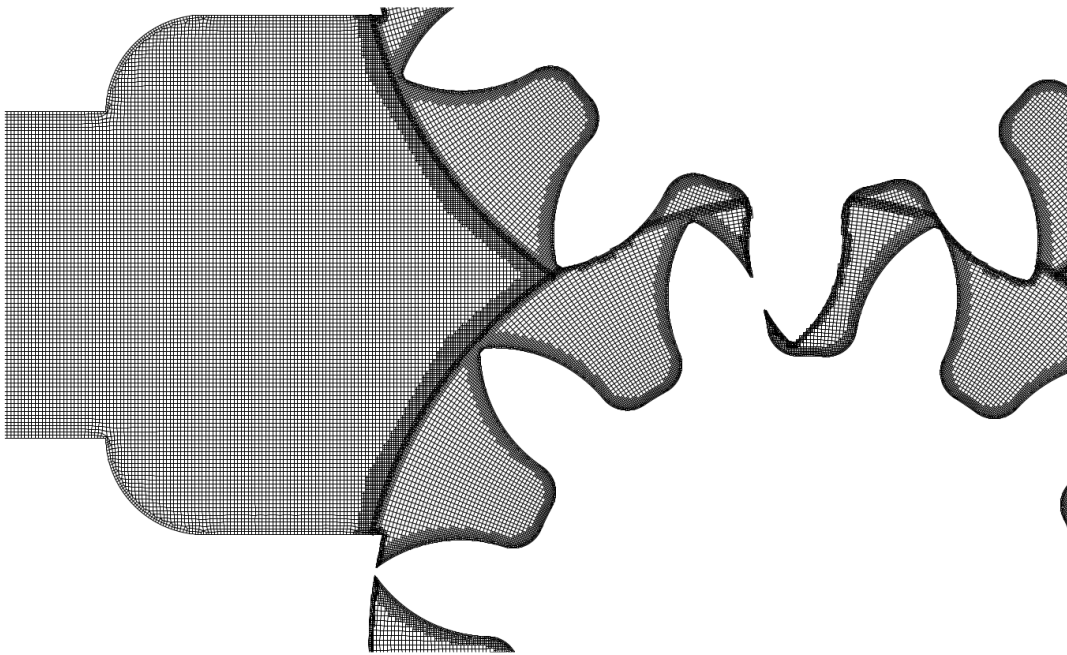


Figure 5.10: Detail view of the employed meshes showing the active cells within the inner part of the suction chamber and the critical central region with the interlocking teeth.

Figure 5.11 compares different flow rate evolutions over one gearing period. The comparison shows the computational data as well as the results with and without gear contact from Castilla et al. (2010). The inflow  $Q$  is normalised using the theoretical flow rate  $Q_T = C_V \cdot f$  with the volumetric capacity  $C_V = 44 \text{ cm}^3/\text{rev}$  taken from Castilla et al. (2010) and the pump frequency  $f = 7.867 \text{ rps}$ . The simulation time is normalised with the gearing period  $T_G = 1/(f \cdot z)$  where  $z = 11$  denotes the number of teeth. The computational results indicate a good agreement with the data reported from the simulation with gear contact by Castilla et al. (2010). The slight differences in comparison with Castilla's data can be deduced to the uncertainty in the gear and gearbox geometry. The simulation without gear contact predicts a volumetric efficiency of approximately 73 % and shows an almost constant flow evolution. In contrast, the gear contact prevents a backflow towards the low pressure side of the pump, which results in an increased mean flow rate of nearly 92 %  $Q_T$  (Castilla et al. 2010), but also in intense fluctuations. The flow rate fluctuations can be explained by the *water hammer effect*, which describes the sudden opening and closing of the inter-teeth chambers and is in good agreement with the flow ripples reported by Ivantysyn and Ivantysynova (1993) and Manring and Kasaragadda (2003). This phenomenon cannot be depicted without gear contact. Castilla justifies the difference between the shape of his observed flow pulse at the inlet and the shape from Ivantysyn and Ivantysynova (1993) and Manring and Kasaragadda (2003) by a location-related difference between the suction and the discharge pipe of the pump, which implies a reverse opening/closing behaviour of the inter-teeth chambers. Note that while Castilla assumes the simplification of only one contact point between both gears and reports convergence problems for trapped fluid,

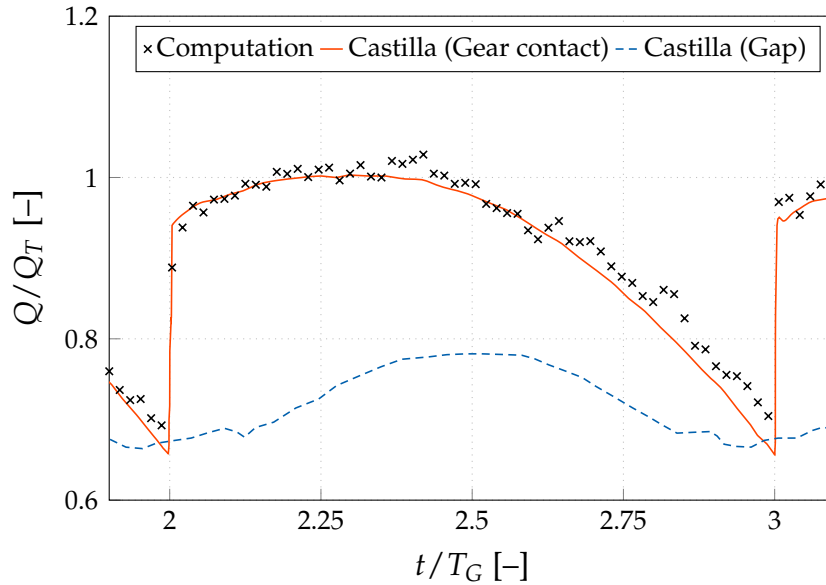


Figure 5.11: Flow rate at the gearpump inlet in comparison with the data obtained from Castilla et al. (2010) with gear contact or gap between the gears. For clarity, only every 20<sup>th</sup> point is displayed.

the employed numerical procedure presented within this thesis handles the enclosed inter-teeth volumes without any convergence problem.

The streamlines in the suction chamber are presented in Figure 5.12. The comparison depicts the computational result on the left-hand side and a graphic taken from Castilla et al. (2010) on the right-hand side. The RSM turbulence model has been reported as one of the best options close to the gearing region and shows a good agreement to the computational results. Hence, this picture from Castilla has been chosen for the comparison. The rotation angle of the gears is based on the figures in Castilla et al. (2010). Both figures show a similar vortex distribution with four main vortices each – two in the upper and two in the lower region. Slight differences occur in between both upper and also both lower vortices, where the computed streamlines are more attached to the side walls of the gearbox. This indicates a stronger separation of the vortices. Moreover, the tip vortices appear to be more intense in the computation. Altogether, a fair agreement of the streamlines can be observed.

In Figure 5.13, detailed focus is put on the normal velocity profiles along lines A, B and C, which are located inside the suction chamber at 60.77 mm, 55.77 mm and 50.37 mm from the inlet, cf. Figure 5.9. The gear position is the same as for the streamlines in Figure 5.12. Figure 5.13 compares the obtained non-dimensional normal velocity distribution  $u_x/\bar{u}_x$  with Castilla's experimental and computational data (Castilla et al. 2010). Here,  $\bar{u}_x$  denotes the mean value of the normal velocity along the respective line with the control variable  $l$  marking the position in relation to the total line length  $L$ . The simulation results show a fair overall agreement with the velocity profiles from Castilla, though slightly smaller maximum values occur in the centre of the channel and the strength of the flow reversal close to the niche walls is generally underestimated in the

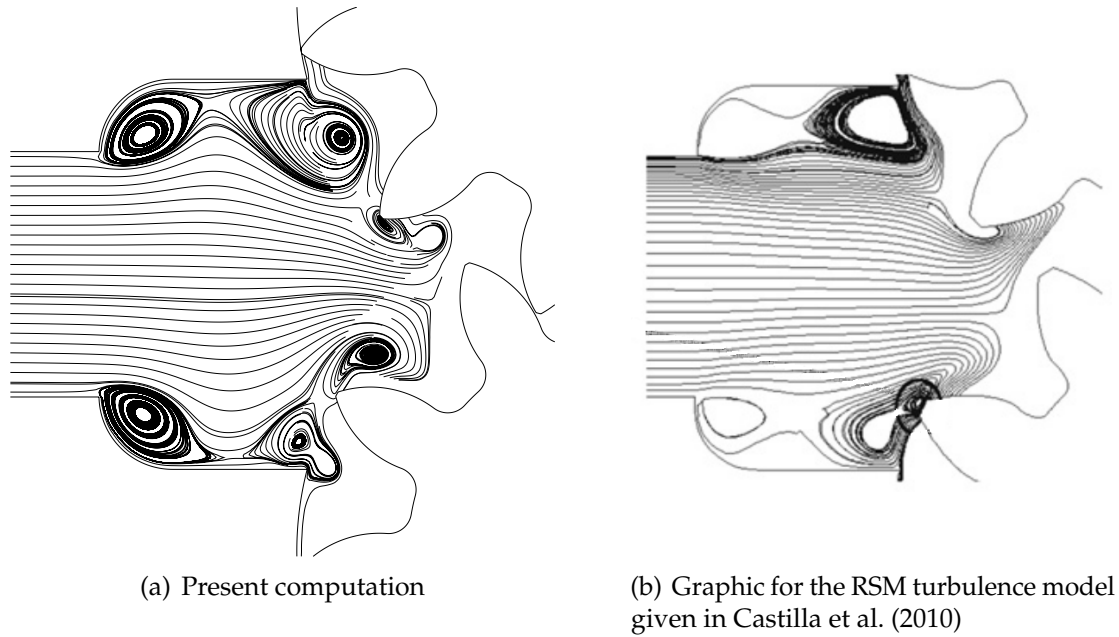


Figure 5.12: Streamlines of the flow in the suction chamber obtained for the present computation (linear eddy-viscosity model) compared to results published by Castilla et al. (2010) (RSM turbulence model).

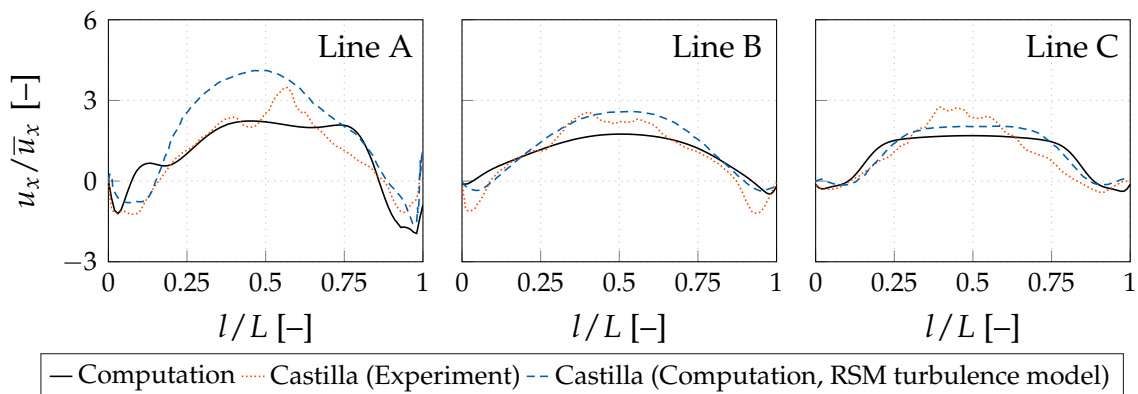


Figure 5.13: Normal velocity distribution along lines A, B and C in comparison with Castilla's experimental and computational data (Castilla et al. 2010). The depicted numerical results from Castilla refer to the RSM turbulence model.

present study. The assessed position of the evaluation line closest to the gears (line A) barely touches the overset regime and is approximately  $0.3 D$  upstream of the nearest modification by artificial boundary conditions. Here,  $D$  refers to the diameter of the gears. Hence, the differences can rather not be attributed to the enhanced overset-grid approach, but the latter can perhaps follow from the weaknesses of the employed eddy-viscosity turbulence model to accurately mimic the curvature induced attenuation of turbulent shear. The vortex velocities in the outer part of the channel are quite

well predicted, except for line B, where the simulation results do not reproduce the entire backflow. With the exception of line C, where both computational distributions practically match each other, discrepancies occur especially in the centre region.

In conclusion, the reasonable accordance of the computational results with the data from Castilla et al. (2010) indicates that the contact of multiple bodies within the overset-grid procedure works and that the developed numerical method can be employed to simulate an external gear pump.

### 5.4 Sliding Wedge

A three-dimensional application of the enhanced overset-grid coupling approach for bodies in direct proximity is concerned with a landslide simulation by means of a sliding wedge in a water tank and observation of the generated wave field. Liu et al. (2005) conducted similar landslide experiments and simulations and measured the free-surface elevation in different gauge positions, which will be used for comparison.

A three-dimensional view of the simulation domain is depicted in Figure 5.14. The slope and the water area of the tank are configured consistent to Liu's examinations, e.g. the slope has a ratio of 1:2 and the tank features a maximum water depth of 3.0 m, which implies a wetted length of 6.0 m. The remaining part of the background domain is enlarged to cover the complete wedge in its initial position. Hence, the overall height and length of the tank read 3.75 m and 7.5 m respectively. The tank has a width of 3.7 m and the wedge is symmetrically arranged.

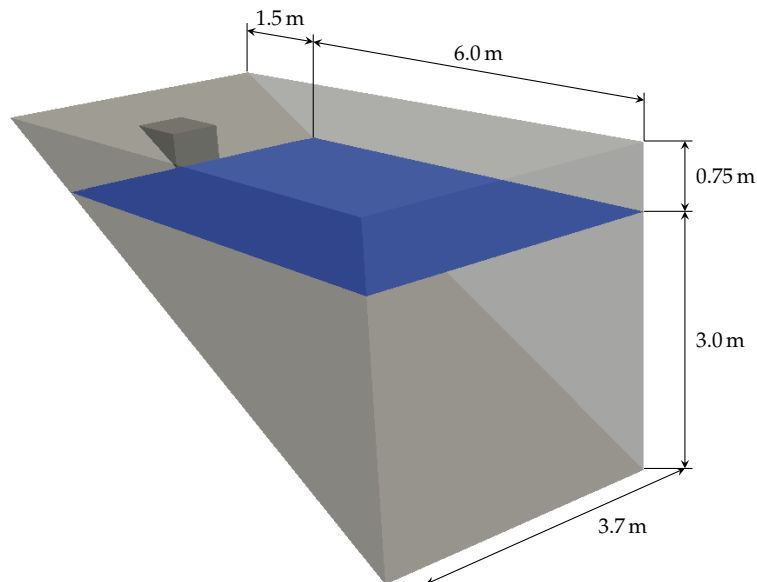


Figure 5.14: Three-dimensional view of the simulation domain with marked dimensions of the water tank and the initial free-surface height. The wedge is depicted in its initial position.

Deviating from the setup of Liu et al. (2005), a slightly lower wedge is investigated in order to generate a thin gap between the slope and the wedge, which shall be closed automatically by means of the inter-grid coupling for bodies in direct proximity. The closure must not affect the sliding body motion and should result in a reasonable wave pattern. Figure 5.15 shows the foreground grid with the embedded wedge in its initial position. The wedge has a width of 0.6525 m, a length of  $L = 0.8947$  m and a height of  $H = 0.4473$  m, resulting in a gap size of one cell between the wedge and the slope, which is indicated in the enlarged view on the lower left of Figure 5.15. The initial position of the wedge is set relative to the free surface by a vertical distance of  $\Delta z = 0.454$  m to the upper boundary of the wedge. The point of origin is positioned in the intersection of the slope and the free surface and relates to symmetric conditions regarding the  $y$ -axis. Water and air phase refer to densities of  $\rho_w = 1000 \text{ kg/m}^3$  and  $\rho_a = 1 \text{ kg/m}^3$ , and the density ratio between the body and the water phase reads  $\rho_B / \rho_w = 3.43$ .

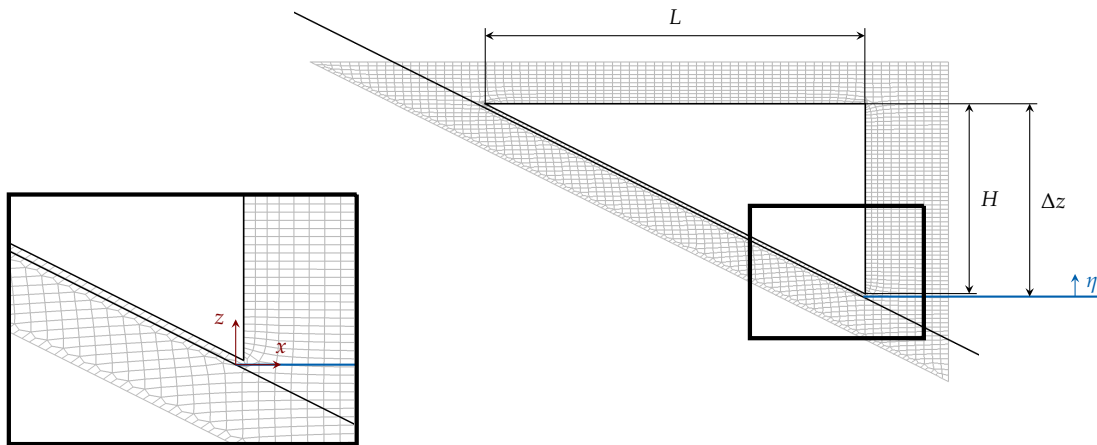


Figure 5.15: Side view of the wedge in its initial position with the surrounding foreground grid. The enlarged view on the lower left pictures the gap size of one cell between the wedge and the slope, the initial free surface (coloured in blue) and the origin of the coordinate system. The total view on the right denotes the wedge dimensions and the initial position relative to the free surface.

The water tank is covered by a background grid of approximately  $5.2 \cdot 10^6$  cells including a refinement box in the immersion area of the wedge using two bisecting refinement steps in each direction. The resolution of the refinement box features approximately 61 cells per wave height when referring to a maximum wave height of roughly 0.3 m. The foreground grid around the wedge features twice the resolution of the background grid, which results in about  $10.4 \cdot 10^4$  cells. This setup leads to a maximum cell area ratio of four in the overlapping region. The slope and the wedge are assigned to no-slip walls, while side and back walls refer to slip wall boundary conditions. The upper boundary is used to preserve a constant pressure level. The approximation of time derivatives employs an implicit second-order accurate three-time level scheme using

a constant time step of  $\Delta t = 0.001$  s. The corresponding maximum Reynolds number reads  $Re_L \approx 2.35 \cdot 10^6$  and turbulent effects are considered by the  $k-\omega$  turbulence model (Wilcox 2006) along with a high-Reynolds wall function approach. The gravity acceleration is set to  $9.81 \text{ m/s}^2$  in negative  $z$ -direction. Contact forces are deemed negligible, hence only hydrodynamic and gravitational forces act on the wedge. Though, the direction of motion is limited to a sliding movement along the slope.

The coordinates of the wave gauges are tabulated and illustrated in Figure 5.16. Note that all wave gauges are arranged within the refined free-surface area of the background mesh. Snapshots of the sliding wedge and the resulting free-surface profiles are depicted

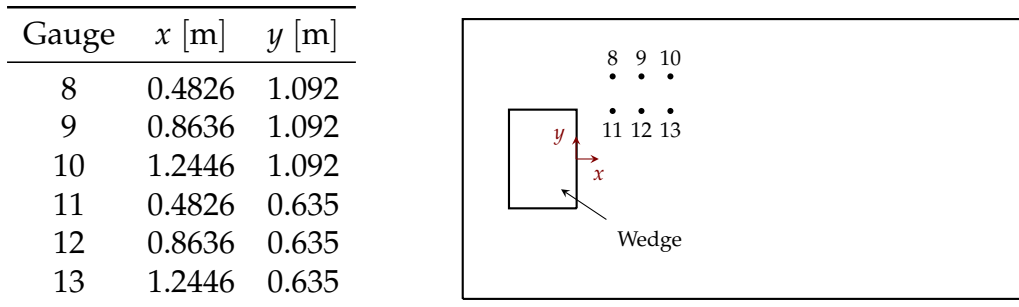


Figure 5.16: Wave gauge positions by means of their coordinates (left) and depicted in a top view of the water tank with the wedge in its initial position (right).

in Figure 5.17. The positions of the wedge and the wave patterns look similar to the results presented by Liu et al. (2005). The resulting free-surface elevations  $\eta$  at the different wave gauges are depicted in Figure 5.18. The graphs display the present computational results in comparison to Liu’s experimental and computational data. The initial wave pattern is extremely well predicted, though some slightly larger surface elevations occur in the end of the simulation time. Altogether, the results indicate a fair agreement with the data reported by Liu et al. (2005), which proves the enhanced overset-grid coupling approach for three-dimensional bodies in direct proximity.

## 5.5 Summary

The inter-grid coupling for bodies in direct proximity has been successfully proved and the method can now be used to investigate the dynamic contact of multiple bodies. The artificial boundary implementation has been verified by a comparison of the results obtained using artificial boundaries with the results obtained using the resolved geometry and shows a satisfactory final agreement between both approaches. The subsequent simulation series of two colliding circular cylinders results in consistent analytical and numerical values and proves that the collision module successfully prohibits a penetration of floating bodies. The applicability of the procedure was demonstrated by the two-dimensional simulation of an external gear pump and a three-dimensional landslide simulation. The gear pump results reveal distinctive flow rate fluctuations which can be explained by the sudden opening and closing of the

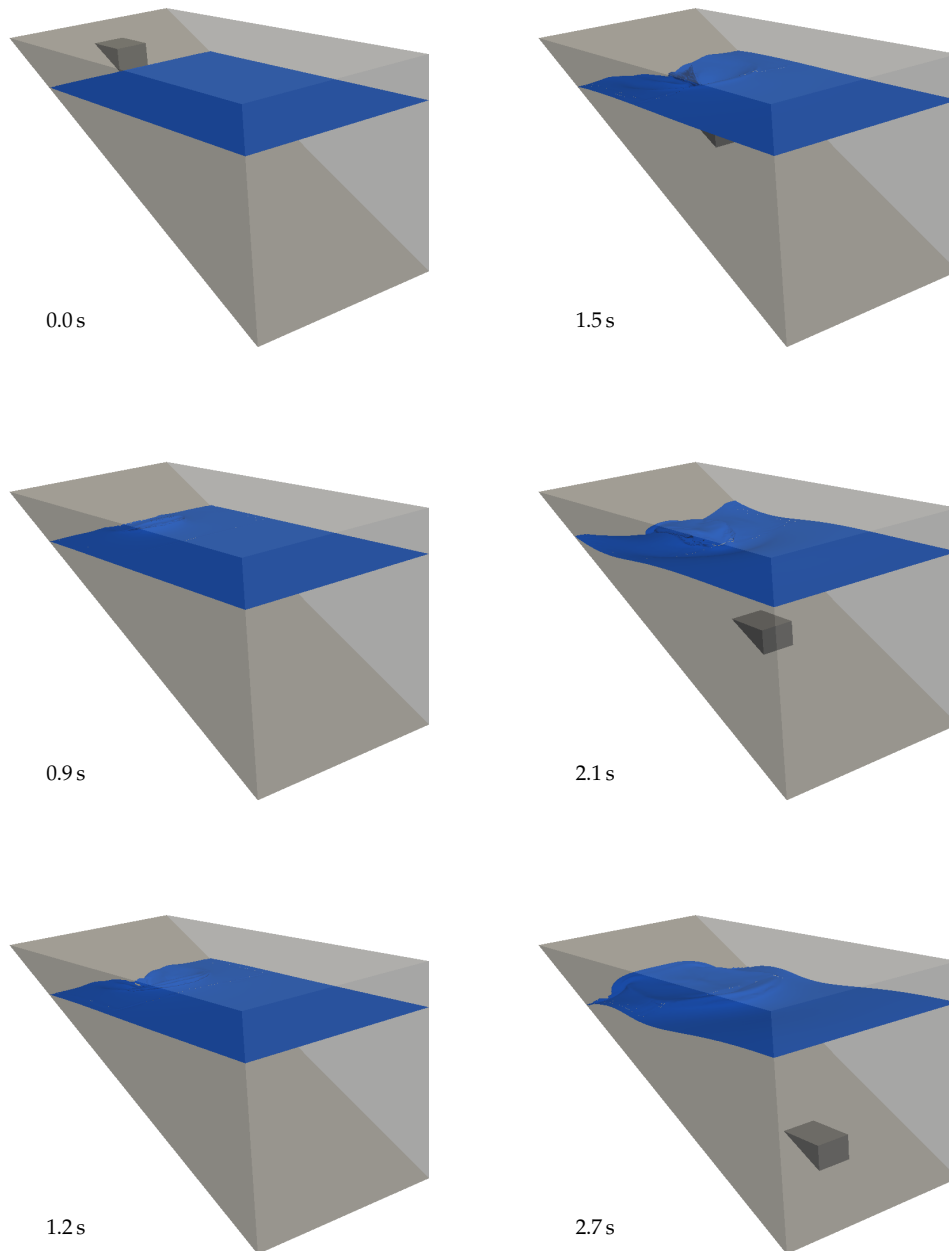


Figure 5.17: Snapshots of the sliding wedge and the free-surface elevation.

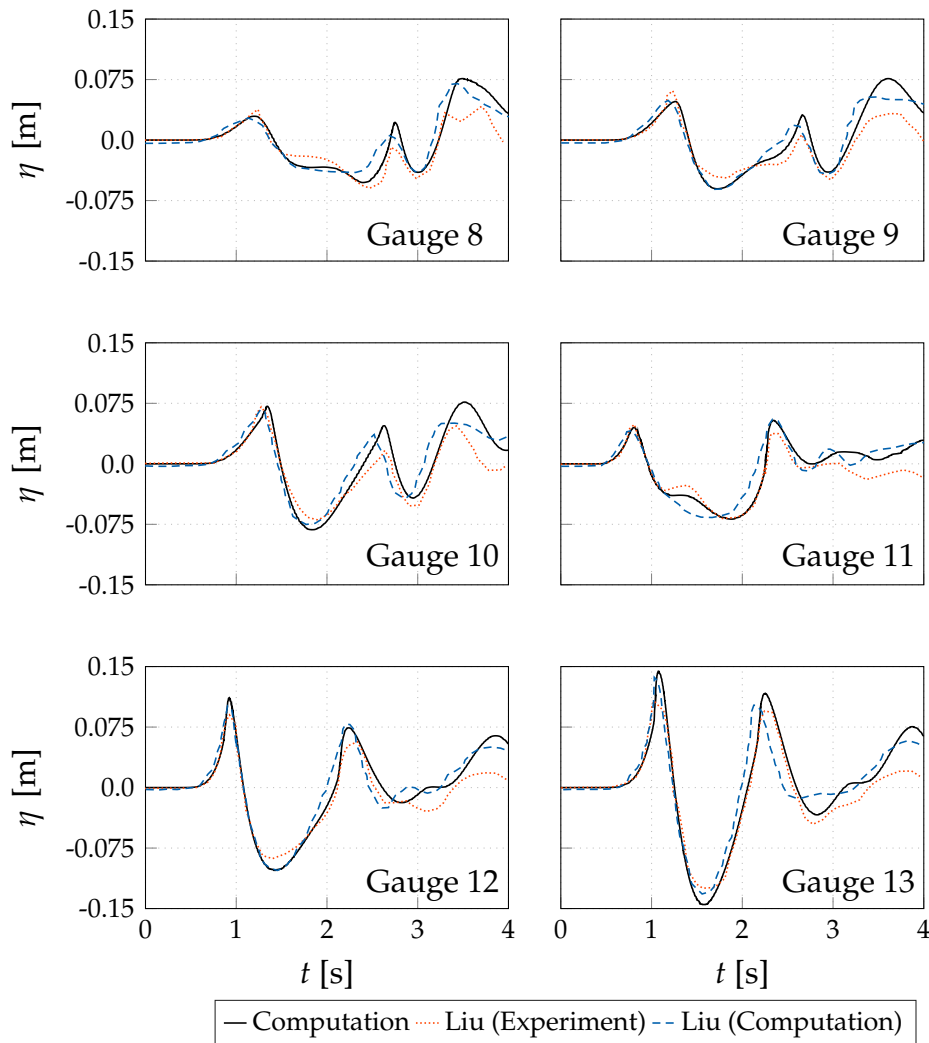


Figure 5.18: Free-surface elevation in gauge 8 to 13 in comparison with the experimental and computational data from Liu et al. (2005).

inter-teeth chambers. This effect cannot be depicted without gear contact and indicates that the contact of multiple bodies within the overset-grid procedure works. The three-dimensional landslide simulation further successfully proves the possibility of computing the flow field around two bodies (wedge and slope) which are separated by a tiny gap.

# 6 Hydrodynamic Wall-Interference Effects

This chapter employs the developed enhanced overset-grid approach from Chapter 3 to analyse hydrodynamic wall-interference effects acting on a circular cylinder and a sphere approaching a plane wall. The chapter starts with a general description of external wall influences on hydrodynamic forces, including (a) the results of related publications, (b) a link between additional resistance and inertia forces and (c) a description of the identification procedure of wall influences. Following, a preliminary study provides baseline data with respect to the forces exerted on a cylinder in unconfined flows and validates the computational approach for the determination of the additional resistance and inertia forces. The main focus of this chapter is on the analysis of proximity influences on the hydrodynamic forces for a two-dimensional circular cylinder in Section 6.4 and a three-dimensional sphere in Section 6.5 in comparison to other numerical, analytical and experimental approaches.

Convective momentum transport is always approximated using a monotonicity preserving QUICK scheme and all transient computations refer to an implicit Euler scheme for the approximation of time derivatives. Overset-grid coupling is performed by a second-order simplex interpolation along with the flux-correction approach in Equation (3.8).

## 6.1 Formulation of the Problem

This chapter investigates proximity influences on inertia and resistance forces of a cylinder and a sphere approaching a plane external wall. The numerical investigations refer to an experimental study of Chander (2015) for a buoyant sphere.

The initial arrangement of the body in a water tank ( $\rho_{\mathcal{F}} = 1\,000\text{ kg/m}^3$ ,  $\mu_{\mathcal{F}} = 10^{-3}\text{ Pa s}$ ), the characteristic dimensions and the employed coordinate system are depicted in Figure 6.1.  $R$  denotes the radius of the body, which is assigned to  $R = 0.05\text{ m}$ , and  $h$  marks the normal distance between the wall and the body centre (initially up to  $h = 5R$ ). Subsequent to the investigation of baseline data with respect to the forces exerted in unconfined flows, contact simulations are performed for a buoyancy-driven ascending two-dimensional circular cylinder and a three-dimensional sphere to extract the additional forces in comparison to unconfined flow conditions. The density ratio between the body and the fluid reads  $\rho_B/\rho_{\mathcal{F}} = 0.861$ . The body motion is described by the velocity  $v_z$  (in the range of  $0.05\text{ m/s}$  to  $0.25\text{ m/s}$ ) and the acceleration  $a_z$ , which are

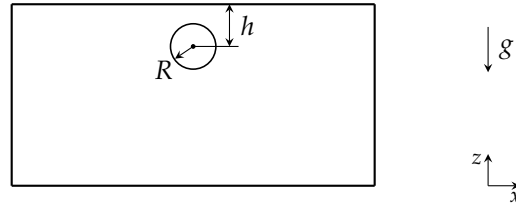


Figure 6.1: Geometry and arrangement of the examined body in a water tank.

positive towards the wall. The diameter-based Reynolds numbers of the study reach approximately up to  $Re_D = 25\,000$ .

## 6.2 Wall Influence on Hydrodynamic Forces

The total hydrodynamic force vector  $F_i$  experienced by a body can be decomposed into a hydrostatic component  $F_{H_i}$  due to buoyancy, a velocity-dependent component  $F_{V_i}$  (i.e. the resistance) and an acceleration-related part  $F_{A_i}$

$$F_i = F_{H_i} + F_{V_i} + F_{A_i}. \quad (6.1)$$

The hydrostatic component points in the positive  $x_3$ - or  $z$ -direction, i.e.  $F_{H_i} = F_H \delta_{i3}$ , and reads  $F_H = -m_{\mathcal{F}} g$ . The gravity acceleration is  $g = 9.81 \text{ m/s}^2$ , and the mass of the displaced fluid  $m_{\mathcal{F}} = \rho_{\mathcal{F}} V$  results from the product of the fluid density and the volume of the submerged body. Supplementary, the Basset (or *history*) force, which describes the development of the boundary layer of an object in transient processes and depends on the difference between the accelerations of the object and the fluid, can be considered as additional force component in Equation (6.1). The behaviour of  $F_{V_i} + F_{A_i}$  in response to nearby located walls is the central issue of this chapter, which is restricted to a negligible Basset force. Previously reported studies on proximity influences were primarily confined to suggestions for spheres and cylinders approaching plane walls. They can be investigated by potential flow and other semi-analytical methods, and allow for a validation of the present numerical procedure against analytical wall-proximity corrections. Mind that for the description of the body motion, the weight of the body  $m_B g$  is needed alongside with the hydrodynamic forces in Equation (6.1).

### 6.2.1 Acceleration Force and Added Mass

Submerged accelerated bodies experience pressure loads due to the inertia of the surrounding fluid. This acceleration-dependent fluid force is usually characterised by an *added, virtual or artificial* mass. In general, the added mass refers to a particular (translational or rotational) direction and depends on the motion in six degrees of freedom. The determination and the analysis of a  $6 \times 6$  added mass matrix for arbitrary geometries and motions are sophisticated. The problem simplifies for geometric

symmetry and a single translational motion, which is the primary reason to look at circular cylinders or spheres approaching a wall in the direction of the wall normal. In this case, one obtains a simple scalar relation

$$F_{A_z} = m_A a_z. \quad (6.2)$$

The added mass  $m_A$ , that mimics the effect of the surrounding fluid, adds to the inertia of the system in dynamic simulations. To avoid expensive fluid-structure interaction simulations, the structure dynamics is often analysed with a constant added mass that mimics the effect of the surrounding fluid (Minorsky 1960). This simple method is deemed a good estimation, e.g. for the assessment of the collision energy at the first impact of an ice mass and a floating structure (Song et al. 2016). Yu (2017) reports an increasing error of the constant added mass method for a decreasing collision angle between two ships, e.g. 22% error in the energy dissipation can be observed for the smallest considered collision angle of 35°. The confining influence of multiple bodies or a free surface is not considered within the simplified concept of a constant added mass although restrictions are frequently deemed responsible for a significant increase (Brennen 1982, Clauss et al. 1988). Therefore, corrections of the baseline value are of interest if bodies collide or operate in close proximity. While arbitrary geometries demand for simulation methods to extract  $m_A$  from Equation (6.2), an analytical potential flow analysis of the added mass modification due to interfering walls is possible for cylinders or spheres which are prime examples regarded in the literature.

The baseline added mass of a sphere in unconfined flow can be deduced from potential flow analysis and is assigned to  $m_A = m_{\mathcal{F}}/2$ . Stokes (1843) was the first to deduce the added mass correction of a sphere which moves perpendicular to an external wall by using potential flow methods as

$$m_A = \frac{m_{\mathcal{F}}}{2} \left[ 1 + \frac{3}{8} \left( \frac{R}{h} \right)^3 \right]. \quad (6.3)$$

The relation assumes that the normal distance between the wall and the body centre  $h$  is much greater than the radius of the sphere  $R$  and neglects higher-order contributions. The added mass of a cylinder in unconfined flow yields  $m_A = m_{\mathcal{F}}$  and a low-order modification in the vicinity of a wall is given by Brennen (1982):

$$m_A = m_{\mathcal{F}} \left[ 1 + \frac{1}{2} \left( \frac{R}{h} \right)^2 \right]. \quad (6.4)$$

In conjunction with spheres, Yang (2006, 2010) demonstrated that the one-term correction in Equation (6.3) provides a fairly accurate representation of the added mass up to  $h \approx 1.5 R$ . Yang also discusses a systematic derivation for a high-order formula by Milne-Thomson (1960), i.e.

$$m_A = \frac{m_{\mathcal{F}}}{2} \left[ 1 + 3 W(\delta^*) \right]. \quad (6.5)$$

The wall correction function  $W(\delta^*)$  depends on the non-dimensional interstitial gap between sphere and wall, i.e.  $\delta^* = (h - R)/R$ , and essentially covers the influence of a series of recursively defined dipoles of a potential flow analysis. Comparing the approaches in Equations (6.3) and (6.5), Yang argues that Equation (6.3) leads to 10% underestimation of the added mass increase for  $h = 1.2 R$ , while the deviation is more than 50% when the sphere reaches the wall. A more elaborate correction formula for a sphere is given by Korotkin (2008):

$$m_A = \frac{m_{\mathcal{F}}}{2} \left[ 1 + \frac{3}{2^3} \left(\frac{R}{h}\right)^3 + \frac{3}{2^6} \left(\frac{R}{h}\right)^6 + \frac{9}{2^8} \left(\frac{R}{h}\right)^8 + \frac{3}{2^9} \left(\frac{R}{h}\right)^9 + \frac{18}{2^{10}} \left(\frac{R}{h}\right)^{10} + \frac{18}{2^{11}} \left(\frac{R}{h}\right)^{11} + \frac{32}{2^{12}} \left(\frac{R}{h}\right)^{12} + \dots \right]. \quad (6.6)$$

The analogue high-order formulation for a cylinder reads (Korotkin 2008)

$$m_A = m_{\mathcal{F}} \left[ 1 + \frac{1}{2} \left(\frac{R}{h}\right)^2 + \frac{1}{8} \left(\frac{R}{h}\right)^4 + \frac{3}{32} \left(\frac{R}{h}\right)^6 + \frac{8}{128} \left(\frac{R}{h}\right)^8 + \frac{23}{512} \left(\frac{R}{h}\right)^{10} + \frac{71}{2048} \left(\frac{R}{h}\right)^{12} + \dots \right]. \quad (6.7)$$

In the course of the present study, the behaviour of a non-dimensional added mass coefficient, i.e.

$$c_A = \frac{|F_{A_z}|}{|a_z| m_{\mathcal{F}}} = \frac{m_A}{m_{\mathcal{F}}} \quad (6.8)$$

with the non-dimensional distance to the wall ( $h/R$ ) is observed for flows around spheres and cylinders.

## 6.2.2 Resistance Force and Added Resistance

In unconfined high Reynolds number flows, the velocity-dependent resistance force is commonly determined by a quadratic relation to the velocity magnitude

$$F_{V_i}^0 = -\frac{1}{2} \left( c_D \rho_{\mathcal{F}} A_p \|v_k\|^2 \right) t_i, \quad (6.9)$$

with  $t_i$  being the entries of the tangent vector of the body trajectory and  $A_p$  being the projected area of the body in the direction of the tangent.  $c_D$  marks a shape-dependent drag coefficient,  $v_k$  denotes the entries of the body velocity vector and  $\|v_k\|$  the magnitude of the velocity vector. This resistance changes in the vicinity of other objects, e.g. a plane wall at rest. The change of resistance is explained by a change of the momentum of the surrounding fluid that is pushed (displaced) by a moving object. When the object approaches a wall, the motion-induced flow needs to be redirected into the tangential wall direction, similarly to the redirection of an impinging jet or effects caused by a mirror image in ideal fluids. First investigations of wall influences

on the resistance of a sphere approaching a wall in the direction of the wall normal have been conducted by Lorentz (1907). Contrary to the present objectives, Lorentz examined creeping flow, for which he observed an increased resistance compared to the well-known Stokes law. Lorentz models the viscous force of a sphere in the vicinity of a wall by a correction factor  $\lambda$ , viz.

$$F_{V_z} = F_{V_z}^0 + \Delta F_{V_z} = -6\pi \mu_{\mathcal{F}} R v_z \lambda, \quad \text{with} \quad \lambda = 1 + \frac{9}{8} \frac{R}{h}. \quad (6.10)$$

Here,  $F_{V_z}^0 = -6\pi \mu_{\mathcal{F}} R v_z$  refers to the baseline resistance in unconfined flow with  $\mu_{\mathcal{F}}$  being the fluid viscosity. Since then, research was primarily devoted to creeping flow conditions (Brenner 1961) or small Reynolds numbers (Cox and Brenner 1967, Ambari et al. 1984). All studies examine a spherical body and mainly define more accurate formulae for  $\lambda$  with a decreasing distance to the wall. Cox and Brenner (1967) showed that an increase of the viscous force similar to Equation (6.10) also works for  $Re_D > 1$ , as long as the product of the scaled interstitial gap  $\delta^*$  and the Reynolds number is small compared to unity. Harada et al. (2001) reported that the numerical results obtained with a correction of the viscous force analogue to Equation (6.10) in combination with the high-order formula for the added mass by Milne-Thomson (1960) agree with the experimental data for Reynolds numbers up to  $Re_D = 25.8$  for a sphere. A comparison of analytical approaches and experimental data for particle trajectories in high Reynolds number flows up to  $Re_D = 95\,000$  is performed by Rostami et al. (2006). In this study, the wall influence is exclusively considered by adjusting the added mass in line with Equation (6.3) and the initial distance to the wall is limited to rather large gaps  $h/R \geq 56$ .

The influence of a diminishing distance to the wall on the resistance force can more generally be derived from the kinetic energy of the fluid that is affected by the moving object. This approach also provides an appreciated link between wall-proximity influences on resistance and inertia forces which was previously outlined by Zhang et al. (1999). Using Stokes' approach for a sphere in Equation (6.3), the kinetic energy of the involved fluid mass reads (Milne-Thomson 1960, Lamb 1932):

$$E_{\text{kin}} = \frac{m_{\mathcal{F}} v_z^2}{4} \left[ 1 + \frac{3}{8} \left( \frac{R}{h} \right)^3 \right]. \quad (6.11)$$

The time derivative of the kinetic energy in Equation (6.11) yields a power that can be factorised into the vertical velocity times a force

$$v_z F^* = v_z m_A \frac{dv_z}{dt} + \frac{v_z^2}{2} \frac{dm_A}{dt} \quad (6.12)$$

with  $m_A = m_{\mathcal{F}}/2$  for a sphere in unconfined flow. The force  $F^*$  inheres two contributions, i.e. an acceleration-related part and a second part, which occurs on the right-hand side of the momentum balance for the sphere and is supplemented by multiple forces

resulting from buoyancy, gravity, viscous or memory effects, etc. The relevant part of the momentum balance for a body with the mass  $m_B$  yields

$$(m_B + m_A) \frac{dv_z}{dt} = -\frac{v_z}{2} \frac{dm_A}{dt} + \dots \quad (6.13)$$

A similar expression follows from the Lagrangian. The term on the right-hand side of Equation (6.13) represents an additional resistance force due to the approaching wall. For a one-dimensional motion along the wall normal, i.e.  $v_z = -dh/dt$ , the derivative of the added mass with respect to time can be recast by

$$\frac{dm_A}{dt} = \frac{\partial m_A}{\partial h} \frac{dh}{dt} = -\frac{\partial m_A}{\partial h} v_z. \quad (6.14)$$

Equation (6.14) allows to express the additional resistance as a function of the temporal or the convective spatial change of the added mass. Using the right-hand side of Equation (6.14), i.e. differentiating the added mass with respect to the distance  $h$ , yields a force which is related to the wall-proximity contributions of the added mass. This additional (pressure) force depends on the displaced fluid mass, the distance to the wall and the body velocity (Zhang et al. 1999):

$$\Delta F_{V_z} = -\frac{m_{\mathcal{F}}}{2} \left[ \frac{v_z^2}{R} \frac{9}{16} \left( \frac{R}{h} \right)^4 \right]. \quad (6.15)$$

The corresponding additional resistance of a cylinder follows from

$$\Delta F_{V_z} = -\frac{m_{\mathcal{F}}}{2} \left[ \frac{v_z^2}{R} \left( \frac{R}{h} \right)^3 \right]. \quad (6.16)$$

The additional resistance can be compiled for any similarly differentiable description of the added mass. Furthermore, an integrable description of an additional resistance can be translated into an added mass change. Zhang et al. (1999) consider the additional force in Equation (6.15) to regard the collision behaviour of two elastic spheres for Reynolds numbers up a  $Re_D = 300$  and report a fair agreement with experimental results. An alternative approximation of the additional force is derived by Yang (2006) from the Milne-Thomson relation in Equation (6.5):

$$\Delta F_{V_z} = -\frac{m_{\mathcal{F}}}{2} \left[ \frac{v_k^2}{R} \frac{3}{2} \frac{dW}{d\delta^*} \right], \quad (6.17)$$

with the derivative of  $W(\delta^*)$  being approximated by

$$\begin{aligned} \frac{dW}{d\delta^*} = & 0.24 - \frac{2.3 \cdot 10^{-4}}{\sqrt{\delta^*}} - 0.31\sqrt{\delta^*} + 6.6 \cdot 10^{-2}\delta^* + 9.8 \cdot 10^{-2} \log(\delta^*) \\ & - \frac{2.06 \cdot 10^{-4} \log(\delta^*)}{\sqrt{\delta^*}} \end{aligned} \quad (6.18)$$

for  $h \leq 2R$ . Coupling this rationale for the added resistance with Korotkin's added mass formulae in Equation (6.6), the added resistance of a sphere reads

$$\Delta F_{V_z} = -\frac{m_{\mathcal{F}}}{2} \left[ \frac{v_z^2}{R} \left( \frac{9}{16} \left( \frac{R}{h} \right)^4 + \frac{9}{64} \left( \frac{R}{h} \right)^7 + \frac{9}{64} \left( \frac{R}{h} \right)^9 + \frac{27}{1024} \left( \frac{R}{h} \right)^{10} + \frac{45}{512} \left( \frac{R}{h} \right)^{11} + \frac{99}{2048} \left( \frac{R}{h} \right)^{12} + \frac{99}{2048} \left( \frac{R}{h} \right)^{13} + \dots \right) \right]. \quad (6.19)$$

Differentiating Equation (6.7) leads to a high-order formula for a two-dimensional cylinder

$$\Delta F_{V_z} = -m_{\mathcal{F}} \left[ \frac{v_z^2}{R} \left( \frac{1}{2} \left( \frac{R}{h} \right)^3 + \frac{1}{4} \left( \frac{R}{h} \right)^5 + \frac{9}{32} \left( \frac{R}{h} \right)^7 + \frac{1}{4} \left( \frac{R}{h} \right)^9 + \frac{115}{512} \left( \frac{R}{h} \right)^{11} + \frac{213}{1024} \left( \frac{R}{h} \right)^{13} + \dots \right) \right]. \quad (6.20)$$

The subsequent analysis refers to an added drag coefficient which is defined by

$$\Delta c_D = \frac{R}{m_{\mathcal{F}} v_z^2} |\Delta F_{V_z}|. \quad (6.21)$$

The development of the three added drag coefficients for a sphere in Equations (6.15), (6.17) and (6.19) is depicted in Figure 6.2 over the non-dimensional distance to the wall  $h/R$ . The comparison reveals an obvious discrepancy between the approach related to Yang (2006) and the suggestions referring to Zhang et al. (1999) and Korotkin (2008).

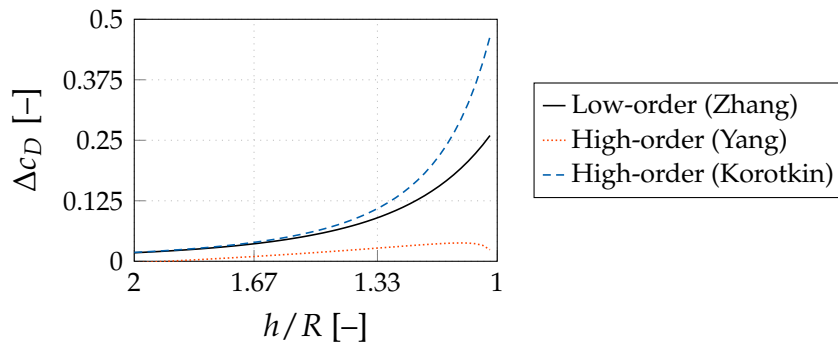


Figure 6.2: Development of the non-dimensional additional drag for a sphere over the non-dimensional distance to the wall returned by the low-order formula of Zhang (Equation (6.15)), the higher-order formula of Yang (Equation (6.17)) and the suggestion in Equation (6.19) derived from Korotkin's added mass expression.

### 6.2.3 Wall Influence Identification Procedure

The present research aims for an identification of the variation of resistance and inertia forces when reducing the distance to another body. Emphasis is put on spheres and cylinders in the vicinity of plane walls where analytical force corrections are available. To begin with, separate studies need to be performed to synthesise the resistance of a non-accelerated obstacle in the vicinity of a wall. This allows to subsequently extract an acceleration force  $F_{A_z}$  from known resistance contributions in accelerated body studies when Basset forces can be ignored, viz.

$$F_{A_z} = F_z - F_{H_z} - F_{V_z}. \quad (6.22)$$

The resistance force comprises two fractions, i.e. a baseline resistance in unconfined flows ( $F_{V_z}^0$ ) and an additional resistance due to the presence of the wall ( $\Delta F_{V_z}$ ). Once again, the wall-proximity contribution can only be extracted for a known baseline resistance in unconfined steady flows, i.e.

$$\Delta F_{V_z} = F_{V_z} - F_{V_z}^0. \quad (6.23)$$

Since simulations – as well as experiments – yield the total force, the baseline contributions in unconfined flow conditions need to be compiled prior to an identification of the additional forces due to wall interference. Constant velocity studies have to be conducted to determine at first the baseline resistance. Subsequently, the additional resistance is determined from similar studies in confined flows. Finally, the additional inertia follows from floating body motion using Equations (6.22) and (6.23). Thereby, different friction and wall models as well as varying initial distances to the wall are considered to evaluate their influence on the wall-interference effect. Figure 6.3 illustrates the elaborate procedure to identify wall influences on hydrodynamic forces. The strategy was pursued to match the buoyancy-driven experiments of Section 6.5. Note that a different strategy could also be used, which additionally performs a series of guided accelerations to replace the buoyancy-driven part of the study. This would help to prevent a singularity associated with zero effective accelerations in Equation (6.8) and offers more control over (undesired) Basset force contributions.

## 6.3 Preliminary Studies

An initial study is performed for a cylinder in unconfined flow. The study aims at two aspects: (a) to assess the credibility of the computational model and (b) to provide the baseline resistance in unconfined flows  $F_{V_z}^0$ . Since the analytical corrections discussed in Section 6.2 are derived from potential flow, the validation refers to slip wall conditions. Rather than inviscid fluids or irrotational flow, laminar flow is employed. The formation of boundary layers is suppressed by slip wall conditions. The sensitivity analysis examines influences of the domain size and the resolution to identify a credible two-

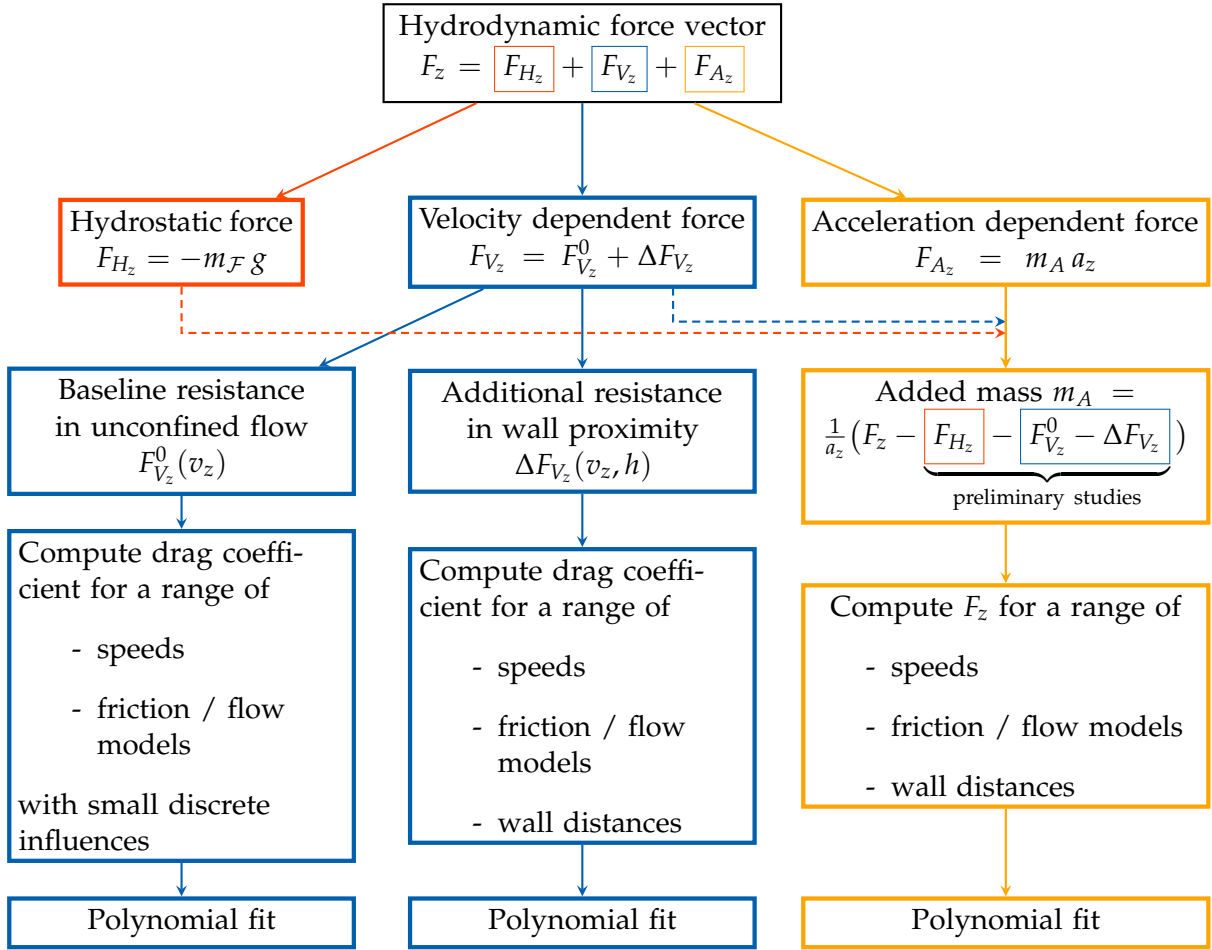


Figure 6.3: Illustration of the identification procedure.

dimensional model. Subsequently, the baseline resistance  $F_{V_z}^0$  follows from a series of simulations with different velocities  $v_z$ , assuming the general behaviour

$$F_{V_z}^0 = -(\alpha |v_z| + \beta) v_z. \quad (6.24)$$

The linear contribution is retained to better fit the lower Reynolds number data. Supplementary, an analogue simulation series is performed for a frictional cylinder wall, using the Reynolds-averaged Navier-Stokes (RANS) equations for turbulent flows.

### 6.3.1 Computational Setup

The two-dimensional simulations refer to water, i.e.  $\rho_{\mathcal{F}} = 1000 \text{ kg/m}^3$  and  $\mu_{\mathcal{F}} = 10^{-3} \text{ Pa}\cdot\text{s}$ . The examined cylinder features a radius of  $R = 0.05 \text{ m}$ . The diameter-based Reynolds numbers for the guided motion studies read  $5000 \leq Re_D \leq 25000$ . The employed domain is displayed in Figure 6.4, its height  $H$  and width  $W$  are briefly analysed in the sensitivity study. The extension in the third (lateral) direction yields

$L = 2R$ . The grid arrangement refers to two overlapping quad-cell grids, where the body is embedded in a foreground grid with an extent of  $3R \times 3R$ . The resolution of the background grid is refined to agree with the foreground grid in the overall overlapping region, i.e. all zones that are swept by the foreground grid, which follows the moving object during a simulation. In contrast to the current preliminary analysis, the investigated wall influences in Sections 6.4 and 6.5 refer to the upper boundary.

During the initial study, the background grid is operated as a channel with the cylinder being located in its centre. The upper and lower boundaries of the channel refer to inlet and outlet (with a prescribed pressure), respectively. Hydrostatic forces are neglected. The background grid features a maximum cell edge length of  $0.24R$ . The resolution of the foreground grid is homogeneous and features an edge length of approximately  $0.06R$  for the coarsest grid, which results in approximately 136 points along the circumference. A detail view of the employed coarsest oversight grids is depicted in Figure 6.4. The sensitivity study is completed by an investigation of the grid resolution.

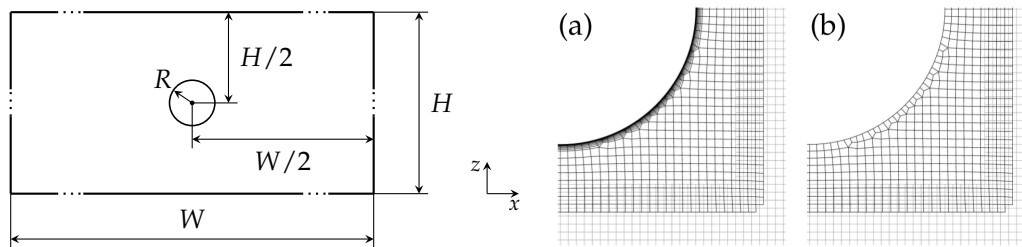


Figure 6.4: Geometry and arrangement of the examined body in the preliminary studies (left) and detail of the employed coarsest oversight grids (a) with and (b) without boundary layer refinement (right). Only active cells are displayed within the detail view of the overlapping grids (foreground grid: black; background grid: grey).

### 6.3.2 Sensitivity Study for Unconfined Flow

The sensitivity study for unconfined flows focusses on the required domain size, the resolution as well as the influence of the flow model, i.e. a frictional body wall and turbulence. The assessment of the resolution and the domain influences either employs steady simulations for a constant inflow velocity of  $u_z = -0.15 \text{ m/s}$  or transient simulations for a constant acceleration of  $a_z = 0.25 \text{ m/s}^2$  using a time step size of  $\Delta t = 10^{-7} \text{ s}$ . For validation, further acceleration values of  $a_z = 1 \text{ m/s}^2$  and  $a_z = 10 \text{ m/s}^2$  are employed.

## Domain Size

To minimise domain influences in the subsequent wall-proximity analysis, the domain is assessed for the laminar (slip wall) case on the coarse grid. Constant velocity and constant acceleration simulations are performed using  $u_z = -0.15 \text{ m/s}$  and  $a_z = 0.25 \text{ m/s}^2$  respectively. For the channel width  $W$ , a range from  $8R$  to  $80R$  is examined, while the

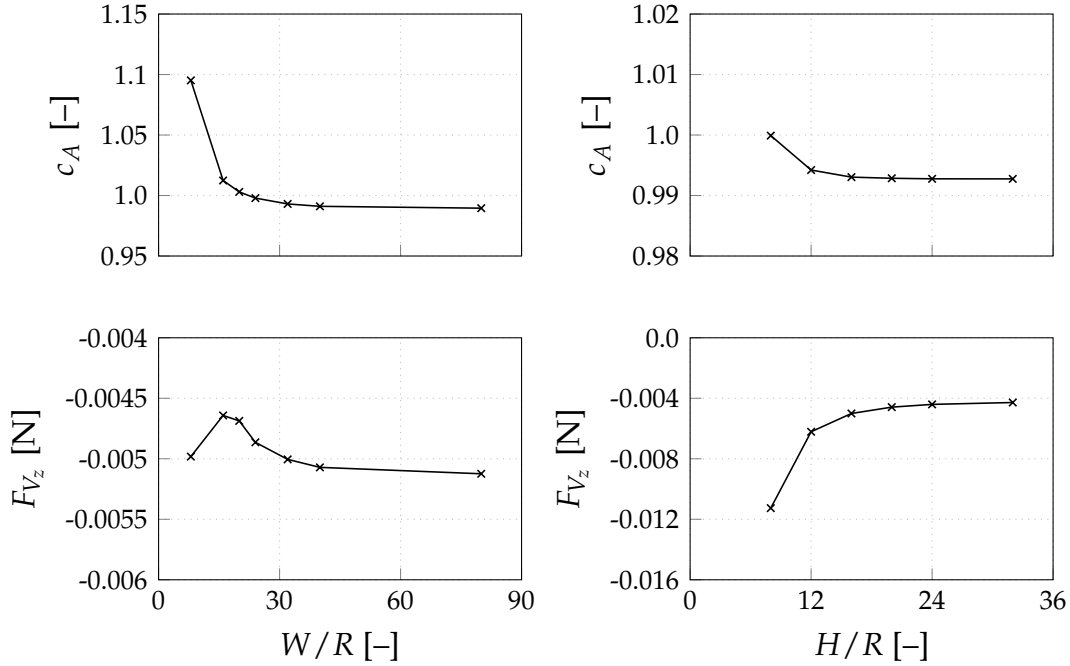


Figure 6.5: Influence of the domain width  $W$  (left; fixed  $H/R = 16$ ) and the domain height  $H$  (right; fixed  $W/R = 32$ ) on the added mass coefficient (top;  $a_z = 0.25 \text{ m/s}^2$ ) and on the baseline resistance (bottom;  $u_z = -0.15 \text{ m/s}$ ) of a cylinder with the radius  $R$  in an unconfined flow using the coarse grids.

channel height  $H$  refers to an investigated range from  $8R$  to  $32R$ . The influence of the width is determined by a constant height study ( $H = 16R$ ), while the influence of the height is determined from constant width study ( $W = 32R$ ). The results depicted in Figure 6.5 reveal that a minimum extension of  $W = 32R$  and  $H = 16R$  should serve as a reference domain in the remainder. The related blockage ratio of the reference domain refers to 6.25 %.

## Resolution

The grid refinement study is based on a refinement of the cell area  $\Delta A$  of the foreground grid and the overlapping region of the background grid. The domain agrees with the above-mentioned reference domain ( $W = 32R$ ,  $H = 16R$ ). Again, resistance tests employ a constant inflow velocity of  $u_z = -0.15 \text{ m/s}$  and added mass studies accelerate both grids with  $a_z = 0.25 \text{ m/s}^2$ . The investigated refinement factors read

$\Delta A_{\text{ref}}/\Delta A = [4, 16, 64]$  for the laminar (slip wall) case and  $\Delta A_{\text{ref}}/\Delta A = [16, 64]$  for the turbulent (frictional wall) case with boundary-layer refinement. The results displayed in Figure 6.6 show a reasonable grid convergence and indicate that the grid configuration with a refinement level of  $\Delta A_{\text{ref}}/\Delta A = 16$  and approximately 536 points along the circumference is sufficient. The following results refer to these *fine grids*, i.e.  $\Delta A_{\text{ref}}/\Delta A = 16$ , without/with boundary-layer refinement for laminar/turbulent flow.

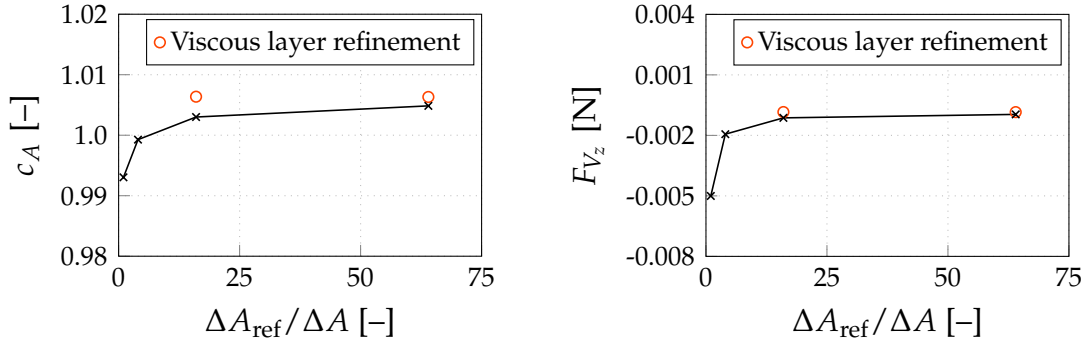


Figure 6.6: Influence of the grid refinement  $\Delta A_{\text{ref}}/\Delta A$  on the added mass coefficient of a cylinder (left;  $a_z = 0.25 \text{ m/s}^2$ ) and on the baseline resistance (right;  $u_z = -0.15 \text{ m/s}$ ) in an unconfined flow.

### Baseline Added Mass

The influences of the acceleration level, the wall model and the turbulence on the added mass coefficient are analysed using the fine grids defined above without an additional viscous layer on the reference domain. Three accelerations, i.e.  $0.25 \text{ m/s}^2$ ,  $1 \text{ m/s}^2$  and  $10 \text{ m/s}^2$ , and three different flow models, i.e. laminar with slip wall conditions, turbulent with slip wall conditions and turbulent with frictional wall conditions, are examined. All three accelerations result in an identical added mass coefficient of  $c_A = 1.003$  for laminar flow and slip wall conditions. The same added mass value is obtained when using turbulent flow in combination with either slip or frictional wall boundary conditions.

### 6.3.3 Baseline Resistance

The baseline resistance of a cylinder in unconfined flow is required to extract the related wall influence in a subsequent study. The cylinder is buoyancy-driven and accelerates to different velocities, hence the baseline resistance is investigated for a range of speeds between  $0.05 \text{ m/s}$  and  $0.25 \text{ m/s}$ . This effort is performed twice, once for laminar flow with slip cylinder walls and once for turbulent flow with frictional cylinder walls. The

simulations are executed on the reference domain ( $W = 32 R$ ,  $H = 16 R$ ) using the fine grids defined above. The polynomial fit of the resistance for slip wall conditions reads

$$F_{V_z}^{0(s)} = - (0.0342 |v_z| + 0.0024) v_z. \quad (6.25)$$

Turbulent flows are simulated with the SST  $k-\omega$  model by Menter (1994) using the fine grids defined above with a boundary layer refinement to employ a low-Reynolds wall boundary condition. The resistance reveals a periodic transient behaviour with up to  $\pm 5\%$  force variations around the mean value. A polynomial fit of the time-averaged mean reads

$$F_{V_z}^{0(t)} = - (3.8761 |v_z| + 0.4435) v_z. \quad (6.26)$$

The quadratic contribution in Equation (6.26) returns a drag coefficient of  $c_D \approx 0.775$ , which is in the range of the expected values for turbulent flow around a smooth circular cylinder (Achenbach 1971). Approximately 98% of the force can be attributed to pressure forces, which indicates flow separation and a low pressure in the aft of the cylinder. The friction force contribution reads

$$F_{V_z}^{0(t_{\text{frict}})} = - (0.0449 |v_z| + 0.0147) v_z, \quad (6.27)$$

which is of the same magnitude as Equation (6.25). The simulation results and the polynomial fits of the total forces are displayed in Figure 6.7.

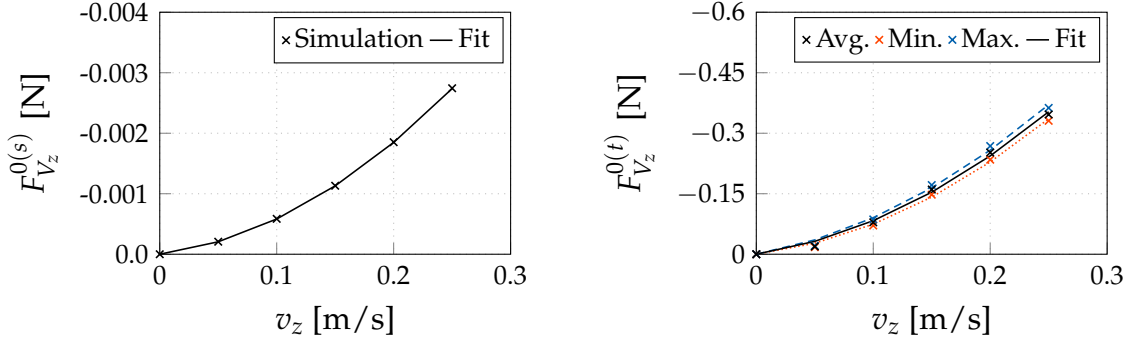


Figure 6.7: Velocity-dependent resistance forces  $F_{V_z}$  for a slip (left) and a frictional (right) cylinder wall.

## 6.4 Wall Influence on a Cylinder

This section deals with the additional resistance and inertia forces experienced by a circular cylinder due to wall-proximity influences. Contact simulations are performed for a buoyancy-driven, ascending two-dimensional circular cylinder in water. The cylinder features a radius of  $R = 0.05$  m and a density of  $\rho_B = 0.861 \rho_{\mathcal{F}}$ . Results are obtained on the reference tank domain using the fine grids defined above. The lateral

boundaries and the wall of the tank are assumed as slip walls, the lower boundary refers to a prescribed pressure. Similar to the studies reported in Section 6.3, separate simulation series are performed for slip and frictional cylinder walls using laminar and turbulent flows, respectively. Mind that the investigated cases did focus upon the one-dimensional motion against the direction of the (external) wall normal.

### 6.4.1 Additional Resistance

The additional resistance is determined by moving the cylinder and the foreground grid from an initial position with constant velocities towards the upper wall. The baseline velocity, the time step and the initial distance read  $v_z = 0.2 \text{ m/s}$ ,  $\Delta t_{\text{ref}} = 10^{-3} \text{ s}$  and  $h_{\text{init}} = 5R$ . The reference time step limits the Courant number to  $Co \leq 0.333$  and the baseline Reynolds number reads  $Re_D = 20000$ . The results are investigated for five velocities ranging from  $v_z = 0.05 \text{ m/s}$  to  $v_z = 0.25 \text{ m/s}$ , two time steps ( $\Delta t_{\text{ref}}, 0.1 \Delta t_{\text{ref}}$ ) and two initial distances ( $h_{\text{init}} = 1.7R$  and  $5R$ ). The obtained forces are median filtered according to Teoh and Ibrahim (2012) using a filter width of  $9 \Delta t_{\text{ref}}$  and are subsequently reduced by the baseline resistance  $F_{V_z}^0$  for the evaluation of the added resistance.

#### Slip Cylinder Wall

The evolution of the filtered total resistance over the non-dimensional distance to the wall is displayed in Figure 6.8 for the slip wall case with  $h_{\text{init}} = 5R$ . Results are shown for the five different velocities from  $v_z = 0.05 \text{ m/s}$  to  $v_z = 0.25 \text{ m/s}$ . Obviously, proximity to the wall and higher velocities increase the resistance force. Subtracting the baseline resistance from the total resistance reveals the evolution of

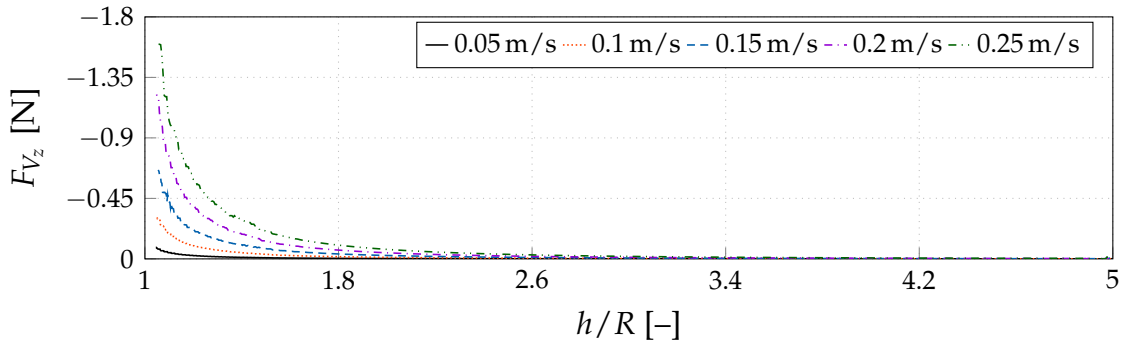


Figure 6.8: Variation of the resistance with the distance to the wall for different velocities ( $h_{\text{init}} = 5R, \Delta t_{\text{ref}} = 10^{-3} \text{ s}$ ).

the added drag coefficient  $\Delta c_D$  according to Equation (6.21). Figure 6.9 shows that all examined velocities result in the same added drag coefficient. As expected, the simulations reveal a considerable non-linear influence, and the linear relation to the velocity in Equation (6.10) is deemed inappropriate to describe the wall influence on the resistance. Figure 6.9 also provides comparisons for the two initial distances and

time steps, which reveal no influence on the added resistance. A comparison of the

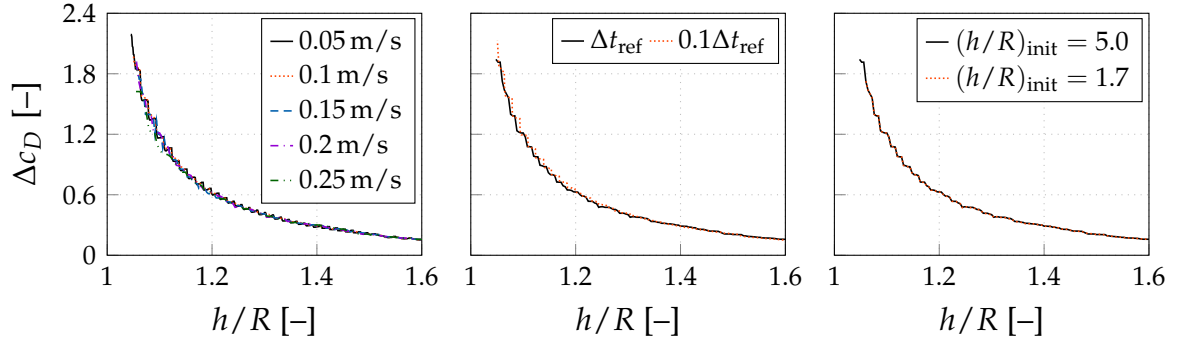


Figure 6.9: Evolution of the added drag coefficient with the non-dimensional distance to the wall (baseline setting:  $h_{\text{init}} = 5R$ ,  $v_z = 0.2 \text{ m/s}$ ,  $\Delta t_{\text{ref}} = 10^{-3} \text{ s}$ ). Comparison for different cylinder velocities  $v_z$  (left), different time steps (centre) and different initial distances (right).

computed added drag coefficient with the expression deduced from Brennen's added mass description (Equation (6.16)) and the approach deduced from Korotkin's added mass description (Equation (6.20)) is displayed in Figure 6.10 and shows a remarkable high-order influence. Figure 6.11 indicates that even the higher-order formula from Equation (6.20) fails to capture the wall influence for  $h < 1.4R$ . An exponential fit of

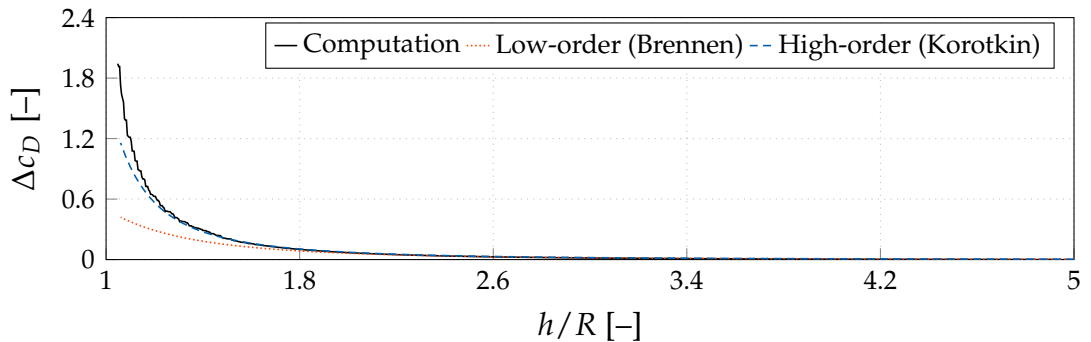


Figure 6.10: Comparison of the evolution of the added drag coefficient obtained from the present simulation with the formulae deduced from Brennen's added mass relation (Equation (6.16)) and from Korotkin's added mass relation (Equation (6.20)).

the added drag coefficient for the near-wall regime obtained from the present slip wall simulations reads

$$\Delta c_D = 21.72 \cdot 10^8 e^{-20.44(h/R)} + 38.02 e^{-3.497(h/R)} \quad (6.28)$$

and intersects with the higher-order formula in Equation (6.20) at  $h_{\text{limit}} \approx 1.454R$ . Note that an exponential function fitted the numerical data much better than a simple

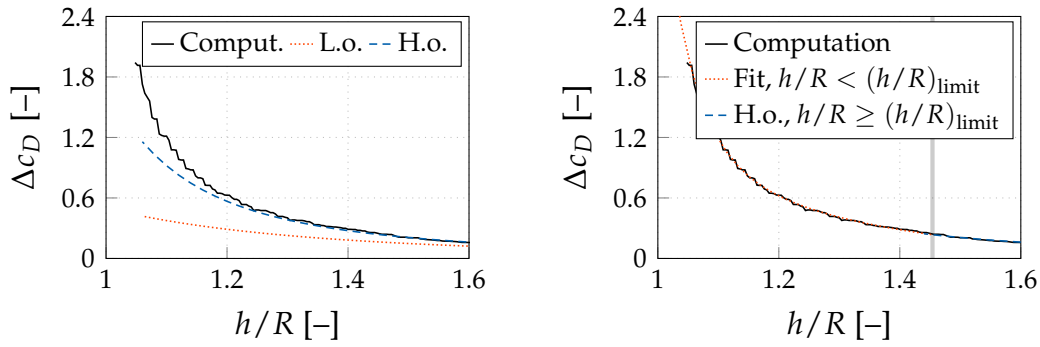


Figure 6.11: Evolution of the added drag coefficient with the distance to the wall. The left-hand side plot pictures a comparison of the simulation results with the low-order formula deduced from Brennen's added mass relation (L.o., Equation (6.16)) and the higher-order formula deduced from Korotkin's added mass relation (H.o., Equation (6.20)). The right-hand side plot shows the computed data, the exponential fit in Equation (6.28) for  $h/R < (h/R)_{\text{limit}}$  and the higher-order formula (H.o.) for  $h/R \geq (h/R)_{\text{limit}}$ . The grey vertical line marks  $(h/R)_{\text{limit}} = 1.454$ .

extension of Equation (6.20) by additional terms. A Taylor series expansion of the exponential fit in Equation (6.28) revealed that fairly high-order expansions beyond the power of 70 are required to match the numerical results in the near-wall regime ( $h/r \leq 1.4$ ), which justifies using an exponential fit.

### Frictional Cylinder Wall

Figure 6.12 shows the evolution of the added drag coefficient for the frictional cylinder wall in turbulent flow. The investigated parameters agree with the slip wall study reported in the previous section 6.4.1. Again, the added drag coefficient displays a pronounced non-linear dependence on the distance to the wall, and no significant difference can be seen for any of the velocities. Likewise, a reduction of the time step does hardly influence the results. As opposed to the slip wall study, the comparison of two initial distances depicts a different evolution of the added drag coefficient. Figure 6.13 reveals that the evolution of the added drag coefficient for the small distance of  $h_{\text{init}} = 1.7R$  approximately agrees with the slip wall results, while the larger initial distance leads to an earlier increase of the added drag coefficient.

To elucidate the issue, three flow fields obtained for a constant body velocity of  $v_z = 0.2 \text{ m/s}$  are compared at a fixed reference location of  $h = 1.4R$ . The comparison involves a turbulent no-slip wall channel flow simulation and two wall-proximity simulations, one using turbulent no-slip wall conditions and one for a slip cylinder wall in laminar flow. Moreover, the initial position is varied, hence the results refer to different runtime/initial positions, i.e. 0.075 s for  $h_{\text{init}} = 1.7R$  and 0.9 s for  $h_{\text{init}} = 5R$ . Figure 6.14 shows the pressure fields and the isolines for  $\|u_i\| = 0.1 \text{ m/s}$ . The channel

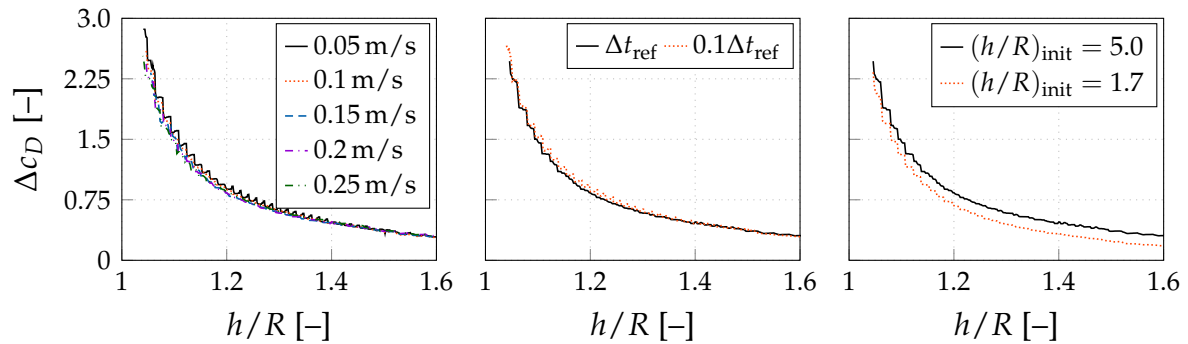


Figure 6.12: Evolution of the added drag coefficient with the distance to the wall for a frictional cylinder wall (baseline setting:  $h_{\text{init}} = 5R$ ,  $v_z = 0.2 \text{ m/s}$ ,  $\Delta t_{\text{ref}} = 10^{-3} \text{ s}$ ). Comparison for different cylinder velocities  $v_z$  (left), different time steps (centre) and different initial distances (right).

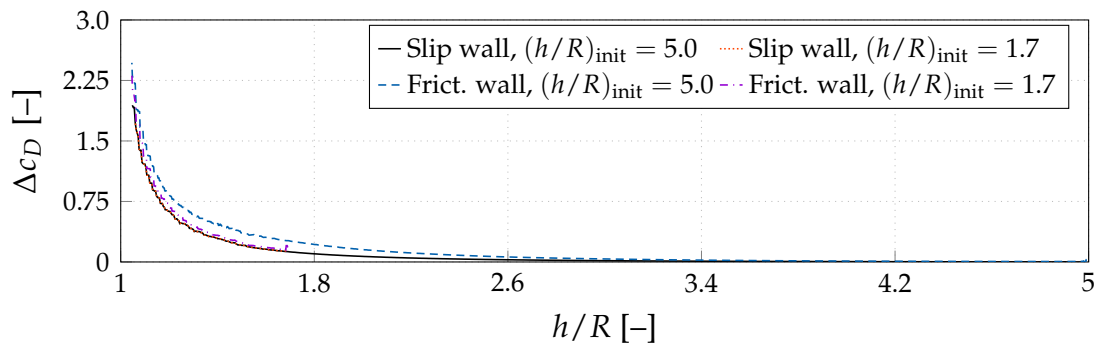


Figure 6.13: Comparison of the evolution of the added drag coefficient obtained from the simulations with a slip and a frictional cylinder wall.

flow results are shown in the left graphs, whereas the other figures refer to wall-influence studies. The images on the right-hand side picture the flow for a slip cylinder wall, and the images on the left-hand side and in the centre refer to the frictional cylinder. It is obvious that for the small initial distance (top row), slip and frictional approaches lead to identical pressure fields and velocity contours when simulating wall influence studies. In comparison to the channel flow results, an increased pressure between the cylinder and the wall as well as widened velocity isolines indicate the wall influence. For the larger initial distance to the wall (bottom row), a boundary layer occurs for both frictional cylinder wall simulations. The boundary layer separates in the aft of the cylinder and yields distinctive vortices afflicted by a low pressure zone. In terms of the wall influence, the impact of these separated vortices can be neglected since the baseline simulation shows the same effects.

The results indicate that the augmented added drag coefficient for  $h_{\text{init}} = 5R$  can be attributed to an increased fluid mass moving with the body. Hence, it is important to know the initial distance or runtime when examining no-slip walls. Note that many researchers, e.g. Harada et al. (2001) or Rostami et al. (2006), emphasised the influence

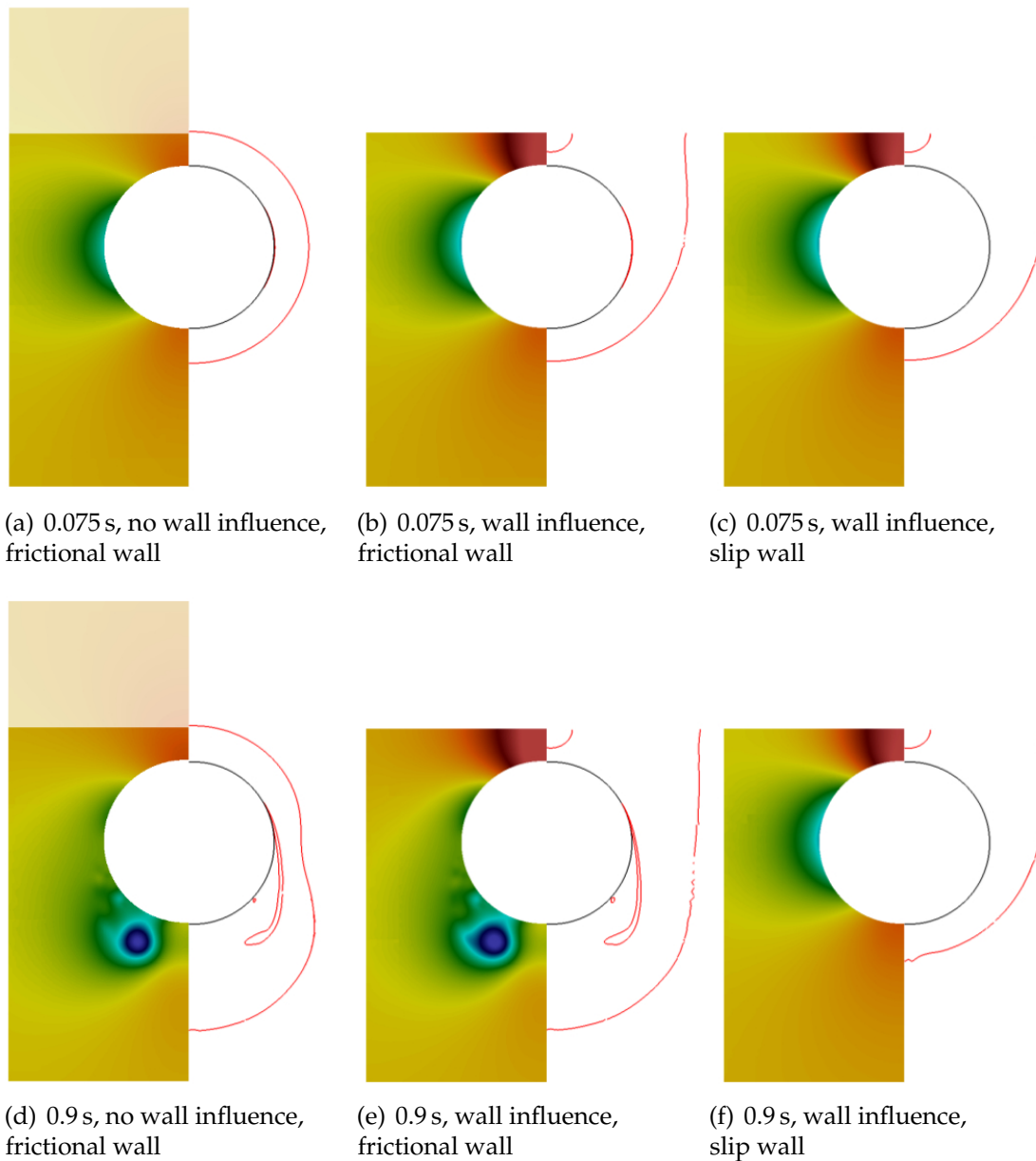


Figure 6.14: Comparison of the pressure fields and velocity contour lines at a runtime of 0.075 s (top) and 0.9 s (bottom). The reference setup without wall influence is shown on the respective left-hand side, whereas the other images refer to proximity to the wall – the blanked areas indicate the end of the computational domain. The images on the left-hand side and in the centre show the flow field around a frictional cylinder wall and the right-hand side pictures the fluid around a slip wall.

of the Basset force, which describes the development of the boundary layer of an object in transient processes. This force depends on the difference between the accelerations of the particle and the fluid. It remains unclear, which extent of the fluid field has to be considered for the Basset force of large particles with arbitrary shape. Since the results generally show the same behaviour with regard to the wall-proximity influence, this study is not extended to analyse memory aspects. The memory effects herein refer to the development of the boundary layer and turbulent structures, which are negligible for the small covered distances that are addressed here. Therefore, the detailed scope of this study is confined to small initial distances, which show a fair predictive agreement due to marginal memory effects.

The computed wall-related additional drag coefficient for a frictional cylinder wall is shown in Figure 6.15. The left graph describes the results for an initial distance of  $h_{\text{init}} = 5 R$ , and the right graph illustrates the situation for  $h_{\text{init}} = 1.7 R$ . The exponential

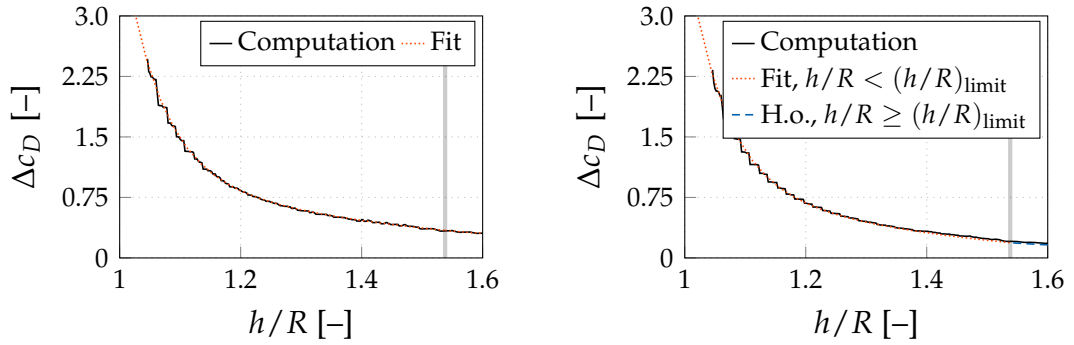


Figure 6.15: Enhanced view of the added drag coefficient for a frictional cylinder wall. The left graph pictures the numerical results for  $h_{\text{init}} = 5 R$  and the exponential fit in Equation (6.29). The right graph shows a comparison of the numerical results for  $h_{\text{init}} = 1.7 R$  with the formula deduced from Korotkin’s added mass approach (Equation (6.20)) for  $h/R \geq (h/R)_{\text{limit}}$  and the adapted exponential fit of Equation (6.29) for  $h/R < (h/R)_{\text{limit}}$ . The grey vertical lines marks  $(h/R)_{\text{limit}} = 1.538$ .

fit for  $h_{\text{init}} = 5 R$  reads

$$\Delta c_D = \begin{cases} 2.46 \cdot 10^7 e^{-15.93 (h/R)} + 9.6 e^{-2.17 (h/R)} & \text{if } h/R < (h/R)_{\text{limit}} \\ 6.38 e^{-2.11 (h/R)} + 0.35 e^{-0.88 (h/R)} & \text{if } h/R \geq (h/R)_{\text{limit}} \end{cases} \quad (6.29)$$

with  $(h/R)_{\text{limit}} = 1.538$ . The right graph outlines an interesting agreement between the predicted results for  $h_{\text{init}} = 1.7 R$ , the higher-order formula deduced from Korotkin’s added mass approach (Equation (6.20)) for  $h/R > 1.538$  and an adjusted exponential fit of Equation (6.29). As outlined by Figure 6.10, Equation (6.20) underestimates the added resistance for vanishing distances to the wall and is, therefore, not shown for  $h/R < (h/R)_{\text{limit}}$ . The exponential fit in Equation (6.29), which has been deduced for  $h_{\text{init}} = 5 R$ , is shifted downwards by an amount of 0.1525, to meet the predictions at  $(h/R)_{\text{limit}}$  when investigating the smaller initial distance to the wall, i.e.  $h_{\text{init}} = 1.7 R$ .

Again, the Taylor series expansion for the exponential function in Equation (6.29) in the near-wall regime proves to be of high order.

### 6.4.2 Added Mass

The wall influence on the added mass is analysed for the buoyancy-induced motion near the upper wall of the tank. The flow model refers to a slip cylinder wall and laminar flow. Simulations are performed on the reference domain using the fine grids defined above. The employed time step is  $\Delta t_{\text{ref}} = 10^{-4}$  s and the initial distance to the wall refers to  $h_{\text{init}} = 1.7 R$ . The coefficient of restitution agrees with the value reported from the experimental study discussed in Section 6.5, i.e.  $e = 0.42$ .

The added mass coefficient is obtained by recording the forces, the position, the velocity as well as the acceleration of the cylinder and applying the combination of Equations (6.22) and (6.8). The velocity-dependent resistance force is composed of two parts, the baseline resistance outlined in Section 6.3.3 and the wall-influence contribution described in the previous section. For the sake of clarity, results are median filtered according to Teoh and Ibrahim (2012) using a filter width of 41 time steps. The resulting evolution of the added mass coefficient over time is plotted in Figure 6.16. The initial

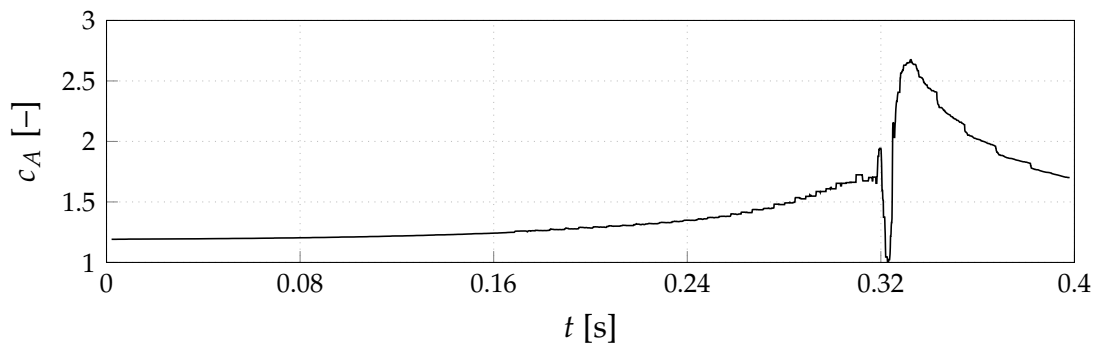


Figure 6.16: Evolution of the added mass coefficient of a buoyancy-driven two-dimensional cylinder that approaches and collides with a plane external wall ( $h_{\text{init}} = 1.7 R$ ).

added mass value slightly exceeds the analytical prediction of 1.0 and increases up to approximately 1.95 when approaching the wall. After the impact at 0.32 s, the added mass evolution shows a sudden drop, followed by a huge peak and a decrease back to the initial value. The increased initial value indicates that the cylinder experiences a wall influence from the very beginning. The post-contact peak could be explained by the surrounding water still partly moving in the direction of the wall and, thereby, decelerating the opposite motion of the body.

Figure 6.17 shows the added mass coefficient over the non-dimensional distance to the wall. The comparison involves the present predictions, the low-order formula of Brennen (Equation (6.4)) and Korotkin's higher-order formula in Equation (6.7). For the

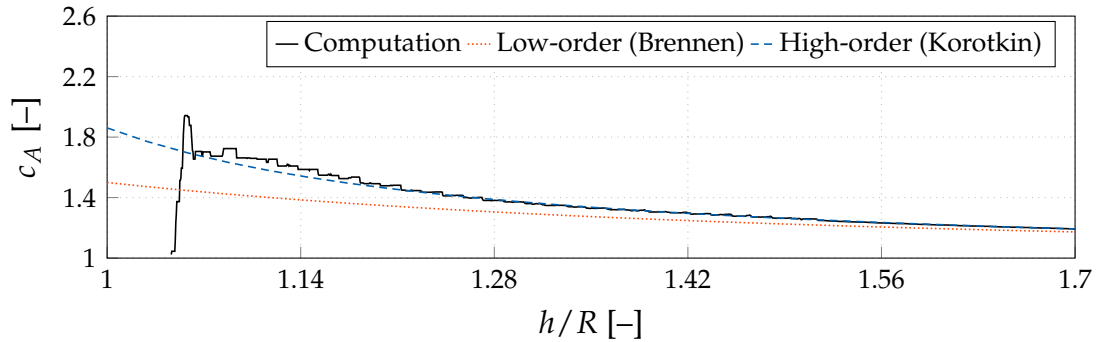


Figure 6.17: Comparison of the added mass coefficient for a cylinder that approaches a wall from an initial distance of  $h_{\text{init}} = 1.7 R$ . The depicted results are obtained from the present simulation, the low-order formula of Brennen (Equation (6.4)) and Korotkin's higher-order formula in Equation (6.7).

sake of clarity, the data are only displayed up to the contact. The comparison shows that the near-wall behaviour is characterised by significant higher-order, non-linear contributions. In line with the results for the added resistance, the comparison suggests that even more terms should be considered in the expansion of Equation (6.7). The disparity of the predictions and the analytical expressions for the added mass and the added resistance occur approximately at the same distance, but the differences for the added mass deviation remain smaller.

Figures 6.17 and 6.18 show that a contact of the cylinder with the wall (i.e.  $h/R = 1$ ) does not happen in the present simulation. This can be attributed to the implemented contact

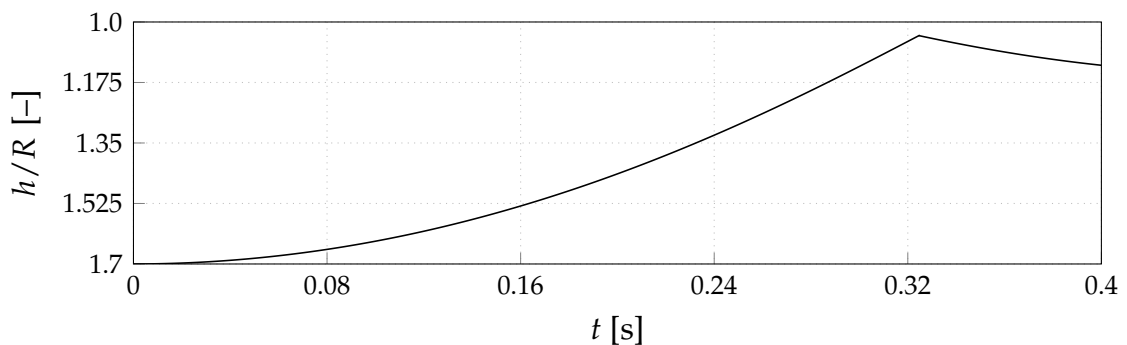


Figure 6.18: Evolution of the non-dimensional distance to the wall over time.

model, cf. Section 3.3. The contact forces are activated in case of coupling problems between the overlapping grids. Figure 6.19 shows the velocity and the pressure fields at the contact and marks coupling problems at the blanked cells between the cylinder and the wall. The minimal distance to the wall refers to three grid cells. This error decreases with an increasing resolution.

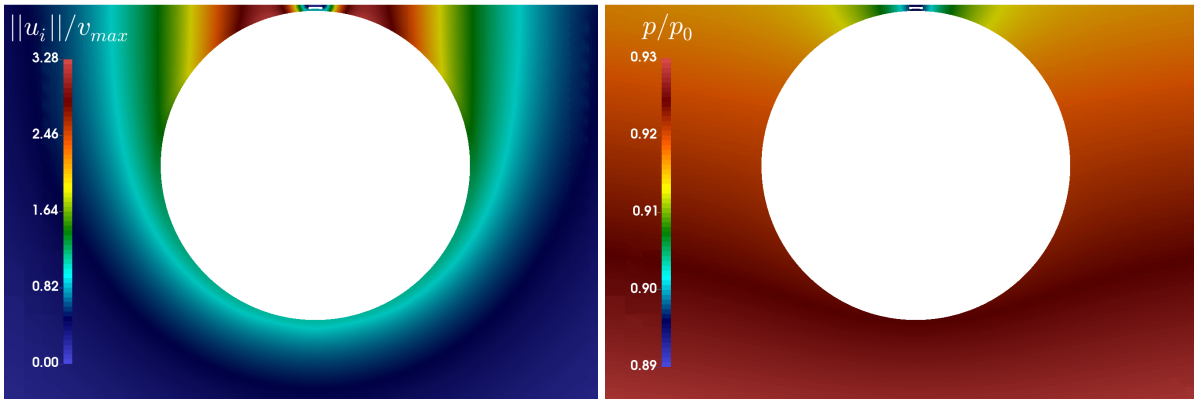


Figure 6.19: Illustration of a coupling problem between the overlapping grids which initiates a premature contact detection (left: velocity; right: pressure).

### Sensitivity Study

The influence of several simulation parameters on the behaviour of the added mass coefficient in wall proximity is analysed to assure the validity of the reported results. For the sake of clarity, only the median filtered results are displayed up to the contact. Figure 6.20 shows the influence of three different time steps ( $\Delta t_{\text{ref}} = 10^{-4}$  s,  $0.5 \Delta t_{\text{ref}}$ ,  $0.25 \Delta t_{\text{ref}}$ ; top), two different flow models (laminar/turbulent; centre) and two wall models in combination with turbulent flow (slip/frictional wall; bottom) on the predicted added mass coefficient. All simulations are performed on the reference domain using the fine grids defined above for an initial distance to the wall of  $h_{\text{init}} = 1.7 R$  that suppresses memory effects. The base configuration refers to laminar flow along a slip cylinder wall and a time step of  $\Delta t_{\text{ref}} = 10^{-4}$  s. The examined time steps, turbulence model and the employed wall model do not affect the result. The results support the conclusion, that viscous effects are of minor importance for the added mass value provided that the additional resistance  $\Delta F_{V_z}$  is accurately determined.

### Initial Distance

Following the experimental study of Chander (2015), three different initial distances to the wall, i.e.  $h_{\text{init}} = [1.4 R, 1.7 R, 2 R]$ , are assessed. Figure 6.21 reveals that the predicted added mass coefficients display a similar behaviour. However, localised oscillations are seen for an initial distance of  $h_{\text{init}} = 2 R$ , which stabilise at the end. This part of trajectory belongs to the zero passage of the acceleration, cf. Figure 6.22, where the added mass evaluation in Equation (6.8) is subjected to a singularity.

## 6.5 Wall Influence on a Sphere

The final analysis observes a buoyancy-driven sphere that approaches the wall of a tank. The tank is filled with water, i.e.  $\rho_{\mathcal{F}} = 1000 \text{ kg/m}^3$  and  $\mu_{\mathcal{F}} = 10^{-3} \text{ Pa s}$ . The radius and

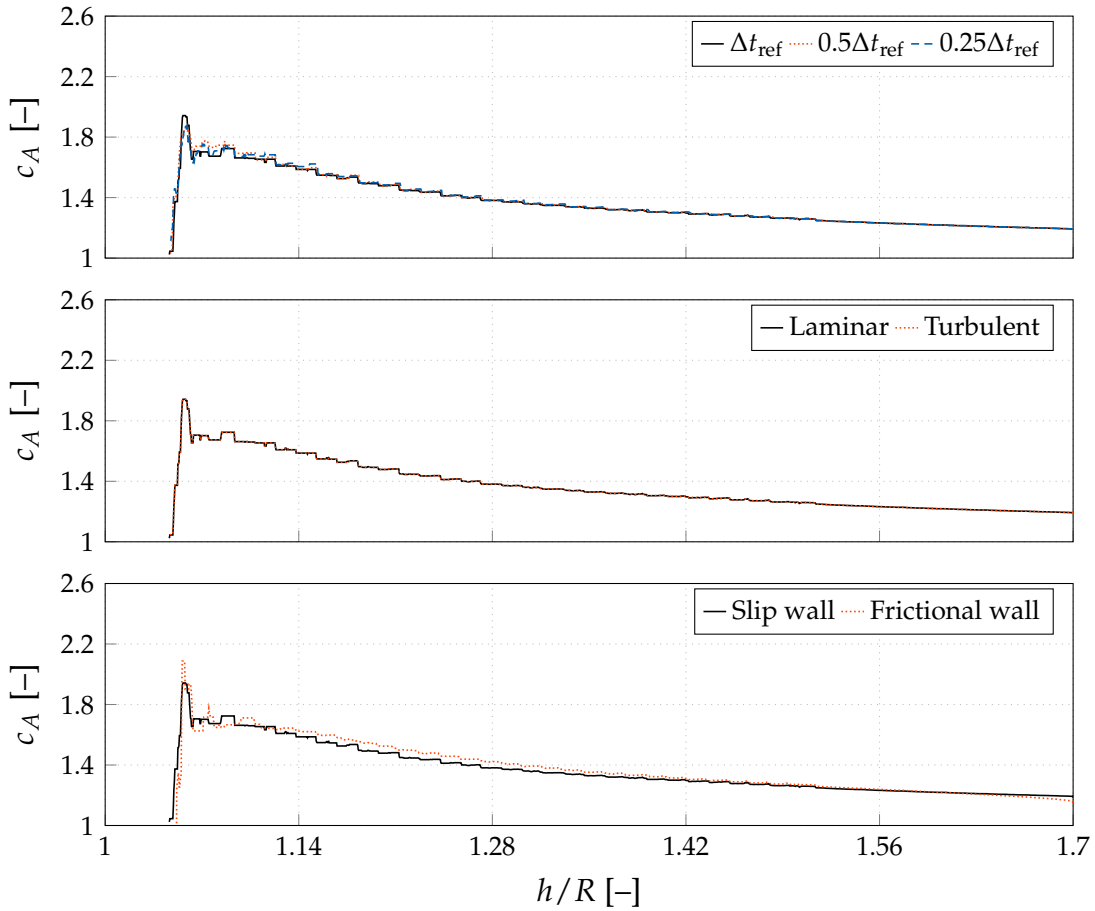


Figure 6.20: Evolution of the added mass coefficient of a cylinder ( $h_{\text{init}} = 1.7 R$ ) for different time steps (top), flow models (slip wall; centre) and cylinder wall models (turbulent flow; bottom). All data are median filtered.

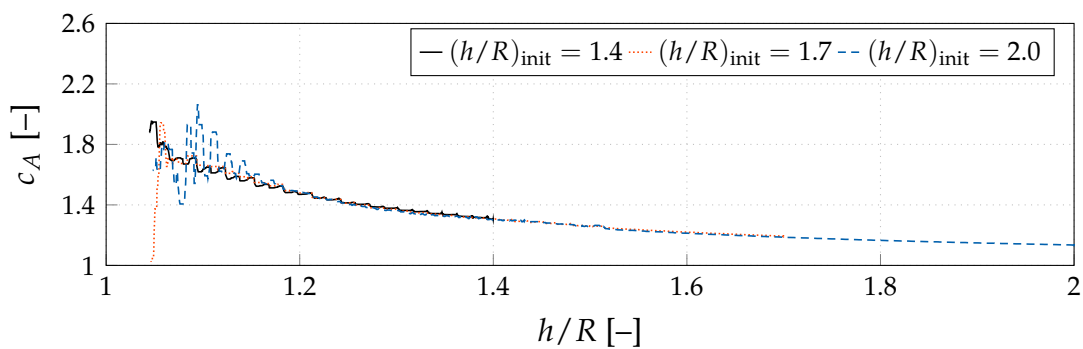


Figure 6.21: Evolution of the added mass coefficient of a cylinder with an initial distance to the wall of  $h_{\text{init}} = [1.4 R, 1.7 R, 2 R]$  over the distance to the wall. All data are median filtered.

the density of the sphere are assigned to  $R = 0.05$  m and  $\rho_B = 0.861 \rho_{\mathcal{F}}$ . All boundaries of the tank and the sphere are slip walls, except for the bottom of the tank, which refers to

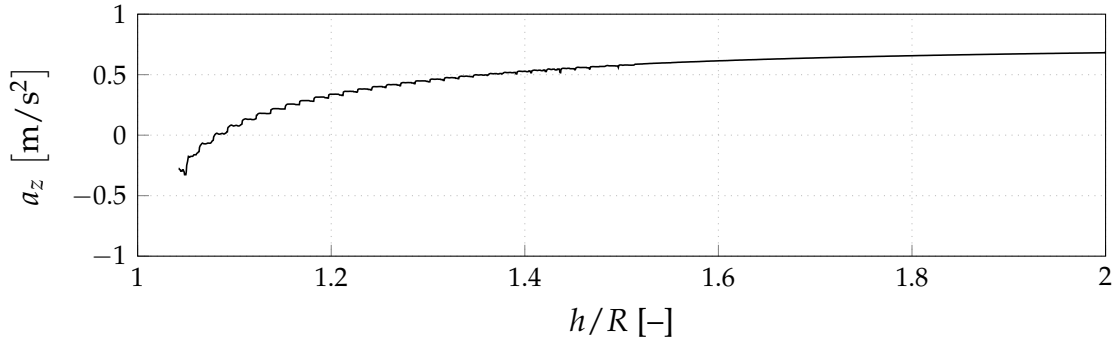


Figure 6.22: Evolution of the acceleration of a cylinder with an initial distance to the wall of  $h_{\text{init}} = 2 R$  over the distance to the wall.

an outlet with a prescribed pressure. Turbulence is neglected. The employed grids refer to the fine grid configuration described in Section 6.3 on a domain of  $32 R \times 32 R \times 16 R$ . The investigated initial distances and the corresponding coefficients of restitution are taken from Chander (2015) and read  $h_{\text{init}} = [1.4 R, 1.7 R, 2 R]$  and  $e = [0.4, 0.42, 0.52]$ , respectively.

The velocity-dependent baseline resistance in unconfined flow  $F_{V_u}^{0(s)}$  is examined in line with the procedure described in Section 6.3. Again, the upper boundary of the domain is converted to an inlet. The polynomial fit reads

$$F_{V_z}^{0(s)} = - (0.0105 |v_z| + 0.0015) v_z. \quad (6.30)$$

The remainder of this section is devoted to the wall influence. Following a comparison between the computed additional resistance and the analytical suggestions discussed in Section 6.2, several contact simulations are conducted to benchmark the predictions against the added mass corrections outlined in Section 6.2. Again, the investigated case focusses upon the one-dimensional motion against the direction of the (external) wall normal. Note that most of the theories described in Section 6.2 only describe a modification of the added mass value while no constant velocity contributions for general motion including contact with the wall are provided. It is, therefore, only possible to include the other theories in a comparison of the added resistance and added mass data with respect to the normalised distance to the wall.

### 6.5.1 Additional Resistance

Results obtained for the two-dimensional cylinder revealed that the external wall influence on the resistance can be concluded from a single velocity. The additional resistance is determined by moving the sphere with a velocity of  $v_z = 0.2 \text{ m/s}$  towards the upper wall. The initial distance of  $h_{\text{init}} = 2 R$  agrees with the maximum distance of the subsequent added mass examinations. The simulation is conducted with a time step of  $10^{-3} \text{ s}$ . The obtained forces are median filtered according to Teoh and Ibrahim (2012)

using a filter width of 9 time steps, and the baseline resistance from Equation (6.30) is subtracted to reveal the wall influence. Figure 6.23 compares the computed added drag coefficient with the low-order formula of Zhang (Equation (6.15)), the higher-order formula of Yang (Equation (6.17)) and the formula derived from Korotkin's added mass expression (Equation (6.19)). All suggestions rest on the link between the wall influences on the added mass and on the added resistance. The figure reveals remarkable

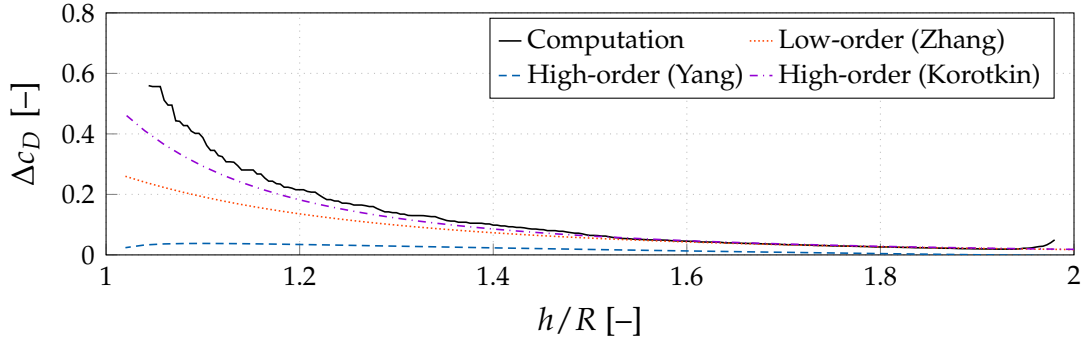


Figure 6.23: Comparison of the added drag coefficient obtained from the simulation, the low-order formula by Zhang (Equation (6.15)), the higher-order formula by Yang (Equation (6.17)) and the higher-order formula derived from Korotkin's added mass expression (Equation (6.19)).

non-linear effects for small distances and shows that the approach of Yang significantly underestimates the predicted results. Even the approach deduced from Korotkin's added mass suggestion falls below the predictions for  $h < 1.5 R$ . A near-wall description of the present results follows from

$$\Delta c_D = 1.692 \cdot 10^6 e^{-14.95(h/R)} + 10.32 e^{-3.315(h/R)}. \quad (6.31)$$

Equation (6.31) intersects with the high-order formula derived from Korotkin's added mass expression (Equation (6.19)) at  $h \approx 1.72 R$ . A Taylor series expansion with the power of 70 is required to fit the exponential results.

### 6.5.2 Added Mass

The wall influence on the added mass is analysed for the buoyancy-induced motion near the upper wall of the water tank. The added mass coefficient is obtained by recording the forces, the position, the velocity as well as the acceleration of the sphere and applying the combination of Equations (6.22) and (6.8). The employed time step is assigned to  $10^{-4}$  s and the results are median filtered according to Teoh and Ibrahim (2012) using a filter width of 61 time steps. In Figure 6.24 the predicted vertical position and the vertical velocity are compared with the experimental data of Chander (2015). The results display a fair predictive agreement, despite the fact that the contact in the simulations occurs before the sphere actually touches the wall due to the implemented contact module, cf. Section 3.3. The comparison of the position shows slightly different

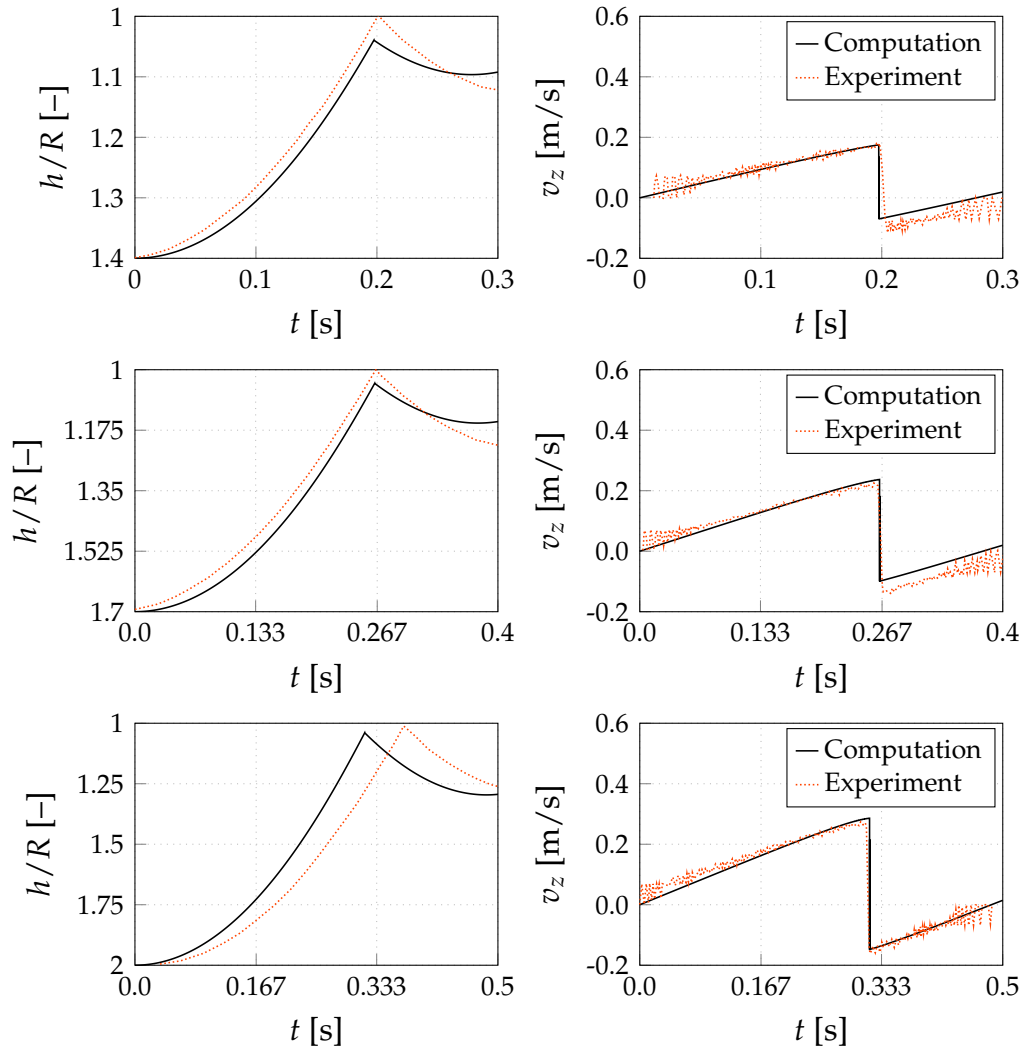


Figure 6.24: Transient evolution of the vertical position (left) and the vertical velocity (right) of a bouyant sphere with an initial distance to the wall of  $h_{\text{init}} = 1.4 R$  (top),  $h_{\text{init}} = 1.7 R$  (centre) and  $h_{\text{init}} = 2 R$  (bottom).

initial gradients and a bigger discrepancy for  $h_{\text{init}} = 2 R$ . However, the experimental data reveal a time shift between the contact events extracted from the position and the velocity for  $h_{\text{init}} = 2 R$ . It is thus expected that the difference between the computations and the experiments can be attributed to experimental inaccuracies. In general, the predicted vertical velocities agree with the experimental data until shortly before the contact, while they tend to be slightly smaller afterwards.

The variation of the predicted added mass coefficient over the distance to the wall is illustrated in Figure 6.25. The initial added mass coefficient of the sphere is slightly higher than the analytical value of 0.5 (Brennen 1982), which indicates that the sphere experiences a wall influence from the beginning. A comparison of the simulation results with the formulae outlined in Section 6.2, i.e. Equations (6.3), (6.5) and (6.6), is given in Figure 6.26 for  $h_{\text{init}} = 1.7 R$ . Analogue to the 2D study, a significant high-order influence

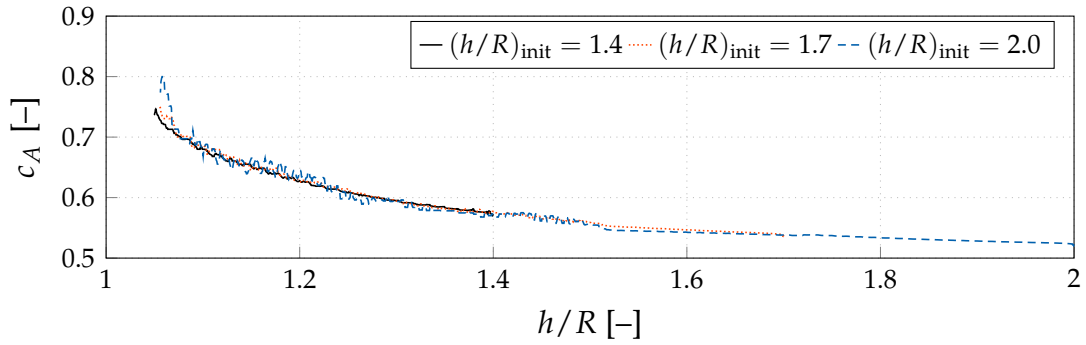


Figure 6.25: Evolution of the added mass coefficient of a wall-approaching sphere for the three different initial distances to the wall  $h_{\text{init}} = [1.4R, 1.7R, 2R]$ . All data are median filtered.

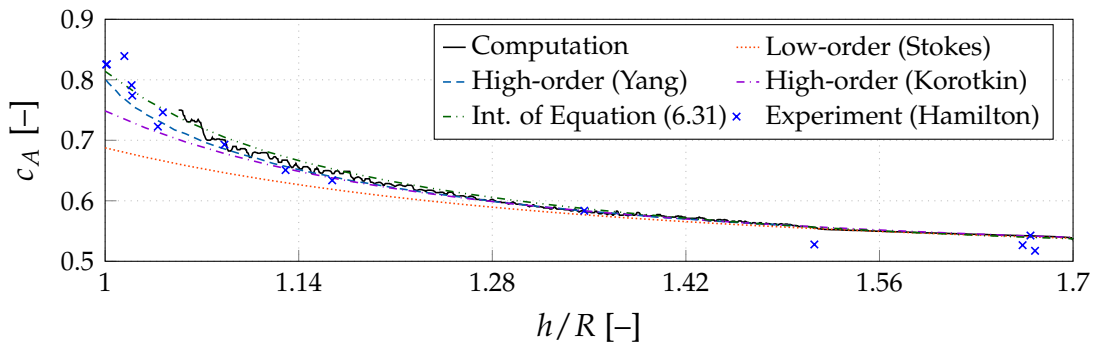


Figure 6.26: Comparison of the added mass coefficient obtained from the computation with the low-order formula by Stokes (Equation (6.3)), the higher-order formulae by Yang (Equation (6.5)) and by Korotkin (Equation (6.6)) as well as the integration of Equation (6.31) and the experimental data by Hamilton. The computational results refer to an initial distance of  $h_{\text{init}} = 1.7R$  and are median filtered.

can be observed. The peak values at  $h/R = 1$  returned by the non-linear approaches are about 20% larger than for the low-order approach by Stokes (Equation (6.3)). The higher-order formula by Yang in Equation (6.5) shows the best agreement with the present results, which is slightly surprising since a disagreement for the added resistance was obvious, cf. Figure 6.23. An integration of Equation (6.31) and repatriation via the energy-based approach leads to an added mass coefficient of  $c_A = 0.814$  at  $h/R = 1$ . Peak values of the added mass coefficient predicted by the formulae of Korotkin (Equation (6.6)) and Stokes (Equation (6.3)) are approximately 8% and 15% smaller than the present result, i.e.  $c_A = 0.75$  and  $c_A = 0.69$ . The present peak value is fairly close to results reported by Hicks (1880) for an image flow approach, which yields  $c_A = 0.8031$ . An interesting study of Hamilton and Courtney (1977) compares theoretical and experimental added mass values for a sphere accelerating away from a wall. Theoretical values are calculated assuming irrotational flow. They agree with the

results of Yang (Equation (6.5)) and slightly underestimate the experiments which were all conducted at a low Reynolds number. As pointed out in Section 6.4.2, viscous and Reynolds number effects should not influence the added mass coefficient significantly. The experimental data gathered by Hamilton and Courtney (1977) is thus added to the comparison displayed in Figure 6.26. The experimentally observed peak reads  $c_A \approx 0.83$  and agrees best with the formula derived from the present computations that is labelled *Int. of Equation (6.31)*.

Experiments of Chander specify added mass values between 1.5 and 2.5. The large added mass values, as well as their large variation, could be attributed to a missing added resistance contribution, which can be quantified by estimates of

$$\frac{|\Delta F_{V_z}|}{|F_{A_z}|} = \left( \frac{v_z^2}{R |a_z|} \right) \frac{\Delta c_D}{c_A}. \quad (6.32)$$

This leads to a definition for a modified added mass coefficient  $c_A^*$  which inheres the added resistance part, i.e.

$$c_A^* = c_A \left[ 1 + \frac{|\Delta F_{V_z}|}{|F_{A_z}|} \right] = c_A \left[ 1 + \frac{v_z^2}{R |a_z|} \left( \frac{\Delta c_D}{c_A} \right) \right], \quad (6.33)$$

where analytical descriptions of the added drag coefficient  $\Delta c_D$  and added mass value  $c_A$  can be computed from Equation (6.31), Equations (6.3) and (6.15), or Equations (6.6) and (6.19) etc. Equation (6.33) returns different modified added mass coefficients for the three cases displayed in Figure 6.24 due to the different accelerations and velocities. Estimating the magnitudes of the acceleration and the velocity from the experimental velocities close to the contact point depicted in Figure 6.24, modified added mass values in the range from 1.4 to 2.5 are obtained from the present computational results, which agrees much better with the experimental observations. The respective ranges of the modified added mass values for the Korotkin and the low-order method read  $[1.05, 1.75]$  and  $[0.85, 1.2]$ , respectively.

It can be summarised that, while the available literature does not entirely capture the predicted external wall influence on the resistance force, it proved to be more accurate for the added mass coefficient.

## 6.6 Summary

Contact simulations between a circular cylinder and a sphere with a plane wall have been investigated to examine proximity influences on the hydrodynamic forces. A significant non-linear increase of the additional resistance and inertia forces has been observed when the bodies approach the external wall. The determined high-order influences can currently not be modelled completely by the suggestions available in the literature, which leads to the derivation of new high-order formulae. The study reveals that the wall influence on the added mass and on the added resistance of the investigated bodies is linked. The numerical investigation indicates that the wall

influence is not affected by the velocity or the acceleration of the body. Even memory effects, which arise from viscous physics, i.e. the wall model and turbulence, can be neglected if the initial distance to the wall does not exceed twice the radius.



## 7 Conclusions

This thesis investigates coupling techniques for overset-grid finite-volume methods and concentrates particularly on the analysis of non-conservative inter-grid coupling effects and modifications to facilitate a dynamic body contact. The expanded capabilities of the overset-grid procedure have been used to study the hydrodynamic interplay of rigid bodies in direct proximity.

The first part of the research has been devoted to the extensive analysis of non-conservative inter-grid coupling effects. While steady-state simulations of incompressible single-phase flows perform well with a non-conservative coupling of non-moving overlapping grids, mass and pressure fluctuations have been observed for transient flows and/or relatively moving grids. The mass defect arises from the direct interpolation of field values, which provokes erroneous fluxes across the overlapping grid boundaries. These imbalances cause an additional varying pressure correction for incompressible transient single-phase flows and/or relatively moving grids if no mass conservation practice is used.

In accordance with formerly reported results for compressible flows, no pressure fluctuations occur for immiscible two-phase flows with high density ratios, since a minor displacement of the free surface attenuates the mass defect entirely. A second-order simplex-based interpolation method proves the best results for single-phase flows on unstructured grids, but can still be afflicted with significant pressure fluctuations. An improvement of the resolution is beneficial - provided that the coupled grids are of similar resolution quality. The latter is a significant drawback for multiple overlapping grids with arbitrary relative grid motion. For further reduction of the mass imbalance in single-phase flows, mass conservation correction practices are examined. The introduction of flux correction practices leads to notable improvements in homogeneous as well as heterogeneous resolution conditions. The best results can be reported for the divergence-based flux correction, which considers local flow information, though the difference to the results obtained with the global flux correction practice are often marginal. Although the volume correction does not achieve the quality of the flux correction methods, it provides a simple alternative to significantly improve the pressure convergence of single-phase flows, since it suppresses the translation of spurious coupling fluxes into the pressure correction.

The insufficient overlap of multiple grids between different bodies in direct proximity has been successfully handled by a modification to the existing overset-grid approach. Critical cells are detected within the overset-grid coupling procedure by marking and deactivating interpolation cells with invalid donors. The flux-based link between

deactivated cells and active cells is replaced by artificial, temporary, no-flux boundary conditions. A simple collision procedure has been implemented to prohibit the penetration of floating bodies.

The artificial boundary implementation and the collision module have been successfully verified and the applicability of the complete procedure has been demonstrated by a two-dimensional simulation of an external gear pump and a three-dimensional landslide simulation. The landslide simulation reveals the possibility of computing the flow field around two bodies that are separated by a tiny gap. The gear pump results show distinctive flow rate fluctuations which are induced by the sudden opening and closing of the inter-teeth chambers and cannot be depicted without gear contact. This indicates that the dynamic contact of multiple bodies within the overset-grid procedure can be considered as fulfilled by the research in this thesis. The method can now be used to investigate complex marine engineering devices including multi-body hydrodynamics featuring mutual interaction and contact between floating bodies.

The enhanced overset-grid approach has been applied to perform contact studies for a cylinder and a sphere approaching a plane wall. The investigated proximity influences show a significant non-linear increase of the additional resistance and inertia forces, when reducing the distance to an external wall. The study reveals that the wall influence on the added mass and on the added resistance is linked. As expected, the respective velocity and acceleration levels of the moving body do not affect the external wall influence. The numerical results indicate that this also holds true for viscous physics, i.e. the wall model and turbulence, when investigating sufficiently small initial distances. The corresponding memory effects can be neglected if the initial wall distances do not exceed twice the radius of the investigated body. This issue should be considered for the assessment of measured data or the layout of experiments.

Previous studies in the literature have not been able to capture the observed non-linear influences. However, they should be considered when investigating bodies that interact hydrodynamically in close proximity. The derived high-order formulae provide simple corrections of the baseline value that can easily be transferred to wetted structural simulations, which apply the simplified concept of an invariant added mass. A generalisation of the analytical wall-interference correction for arbitrary shapes and encounter angles should be the subject of future research.

# Bibliography

- A. Achenbach. Influence of Surface Roughness on the Cross-Flow around a Circular Cylinder. *Journal of Fluid Mechanics*, 46(2):321–335, 1971.
- M. Al-Azawy, A. Turan, and A. Revell. Investigating the Impact of Non-Newtonian Blood Models Within a Heart Pump. *International Journal for Numerical Methods in Biomedical Engineering*, 33(1), 2017.
- A. Ambari, B. Gauthier-Manuel, and E. Guyon. Wall Effects on a Sphere Translating at Constant Velocity. *Journal of Fluid Mechanics*, 149:235–253, 1984.
- E. Atta. Component-Adaptive Grid Interfacing, AIAA Paper 81–0382. In *19th Aerospace Sciences Meeting*, St. Louis, Missouri, January 1981. doi: 10.2514/6.1981-382.
- H. Bandringa. Immersed Boundary Methods. Master’s thesis, University of Groningen, 2010.
- E. Basso and J. Azevedo. Three-Dimensional Viscous Flow Simulations over the VLS using Overset Grids. *Journal of the Brazilian Society of Mechanical Sciences and Engineering*, 26(4):438–445, 2004. doi: 10.1590/S1678-58782004000400009.
- J. Benek, J. Stegert, and F. Dougherty. A Flexible Grid Embedding Technique with Application to Euler Equations. In *6th Computational Fluid Dynamics Conference Danvers*, Danvers, Massachusetts, 1983. doi: 10.2514/6.1983-1944.
- M. Berger. On Conservation at Grid Interfaces. *SIAM Journal on Numerical Analysis*, 24(5):967–984, 1987. doi: 10.1137/0724063.
- A. Berton, F. D’Orrico, and M. Sideri. Overset Grids for Fluid Dynamics Analysis of Internal Combustion Engines. *Energy Procedia*, 126:979–986, 2017.
- C. Brennen. A Review of Added Mass and Fluid Inertial Forces. Technical Report N62583-81-MR-554, Navel Civil Engineering Laboratory, 1982.
- H. Brenner. The Slow Motion of a Sphere Through a Viscous Fluid Towards a Plane Surface. *Chemical Engineering Science*, 16(3-4):242–251, 1961.
- J. Brunswig and T. Rung. RANS Simulations using Overset Meshes. In *4th International Conference on Computational Methods in Marine Engineering - MARINE 2011*, pages 564–572, Lissabon, Portugal, 2011.
- J. Brunswig and T. Rung. Parallel Performance of Overset Grids Algorithm using Load Balancing. *5th International Conference on Computational Methods in Marine Engineering - MARINE 2013*, Hamburg, Germany, May 2013.

- P. M. Carrica, F. Ismail, M. Hyman, S. Bhushan, and F. Stern. Turn and Zigzag Maneuvers of a Surface Combatant using a URANS Approach with Dynamic Overset Grids. *Journal of Marine Science and Technology*, 18(2):166–181, 2013. doi: 10.1007/s00773-012-0196-8.
- R. Castilla, J. Wojciechowski, P. Gamez-Montero, A. Vernet, and E. Codina. Analysis of the Turbulence in the Suction Chamber of an External Gear Pump using Time Resolved Particle Image Velocimetry. *Flow Measurement and Instrumentation*, 19(6): 377–384, 2008.
- R. Castilla, P. Gamez-Montero, N. Ertürk, A. Vernet, M. Coussirat, and E. Codina. Numerical Simulation of Turbulent Flow in the Suction Chamber of a Gearpump using Deforming Mesh and Mesh Replacement. *International Journal of Mechanical Sciences*, 52(10):1334–1342, 2010.
- R. Castilla, P. Gamez-Montero, D. Del Campo, G. Raush, M. Garcia-Vilchez, and E. Codina. Three-Dimensional Numerical Simulation of an External Gear Pump with Decompression Slot and Meshing Contact Point. *Journal of Fluids Engineering*, 137(4):041105, 2015.
- S. Chander. Experimental and Numerical Hydrodynamic Study of Submerged Ice Collision. Master's thesis, Memorial University of Newfoundland, 2015.
- G. Chesshire and W. Henshaw. A Scheme for Conservative Interpolation on Overlapping Grids. *SIAM Journal on Scientific Computing*, 15(4):819–845, 1994. doi: 10.1137/0915051.
- B. Chung, P. Johnson, and A. Popel. Application of Chimera Grid to Modelling Cell Motion and Aggregation in a Narrow Tube. *International Journal for Numerical Methods in Fluids*, 53(1):105–128, 2007. doi: 10.1002/flid.1251.
- G. Clauss, E. Lehmann, and C. Ostergaard. *Meerestechnische Konstruktionen*. Springer Berlin et al., 1988.
- R. Cox and H. Brenner. The Slow Motion of a Sphere Through a Viscous Fluid Towards a Plane Surface – II Small Gap Widths, Including Inertial Effects. *Chemical Engineering Science*, 22(12):1753–1777, 1967.
- D. Del Campo, R. Castilla, G. Raush, P. Gamez Montero, and E. Codina. Numerical Analysis of External Gear Pumps Including Cavitation. *Journal of Fluids Engineering*, 134(8):081105, 2012.
- I. Demirdžić and M. Perić. Space Conservation Law in Finite Volume Calculations of Fluid Flow. *International Journal for Numerical Methods in Fluids*, 8:1037–1050, 1988. doi: 10.1002/flid.1650080906.
- R. Devendran and A. Vacca. Optimal Design of Gear Pumps for Exhaust Gas Aftertreatment Applications. *Simulation Modelling Practice and Theory*, 38:1–19, 2013.
- J. Duncan. The Breaking and Non-Breaking Wave Resistance of a Two-Dimensional Hydrofoil. *Journal of Fluid Mechanics*, 126:507–520, 1983.

- N. Ertürk. Experimental Study of the Flow in an External Gear Pump by Time Resolved Particle Image Velocimetry. Master's thesis, Department of Mechanical Engineering, Universitat Rovira I Virgili, Tarragona, Spain, 2008.
- J. Ferziger and M. Perić. *Computational Methods for Fluid Dynamics*. Springer-Verlag, 2002. ISBN 9783540420743. doi: 10.1007/978-3-642-56026-2.
- J. Ferziger and M. Perić. *Numerische Strömungsmechanik*. Springer-Verlag, 2008.
- C. Freitas and S. Runnels. Simulation of Fluid-Structure Interaction using Patched-Overset Grids. *Journal of Fluids and Structures*, 13(2):191–207, 1999. doi: 10.1006/jfls.1998.0200.
- D. Gross, W. Hauger, J. Schröder, and W. Wall. *Technische Mechanik 3: Kinetik*. Springer-Verlag, 2012.
- H. Hadžić. *Development and Application of Finite Volume Method for the Computation of Flows around Moving Bodies on Unstructured, Overlapping Grids*. PhD thesis, Technische Universität Hamburg-Harburg, 2006.
- W. Hamilton and G. Courtney. Added Mass of Sphere Starting Upward Near Floor. *ASCE J Eng Mech Div*, 103(1):79–97, 1977.
- S. Harada, T. Tanaka, and Y. Tsuji. Fluid Force Acting on a Particle Falling Toward a Wall. *JSME International Journal Series B Fluids and Thermal Engineering*, 44(4):520–525, 2001.
- A. Harten. High Resolution Schemes for Hyperbolic Conservation Laws. *Journal of Computational Physics*, 49:357 – 393, 1983.
- W. Hicks. On the Motion of Two Spheres in a Fluid. *Philosophical Transactions of the Royal Society of London*, 171:455–492, 1880.
- C. Hirt and B. Nichols. Volume of Fluid (VOF) Method for the Dynamics of Free Boundaries. *Journal of Computational Physics*, 39(1):201–225, 1981.
- G. Houzeaux and R. Codina. Numerical Simulation of Gear Pumps. Technical report, International Center for Numerical Methods in Engineering (CIMNE), 2003.
- E. Hylla. *Eine Immersed Boundary Methode zur Simulation von Strömungen in komplexen und bewegten Geometrien*. PhD thesis, Technische Universität Berlin, 2013.
- J. Ivantysyn and M. Ivantysynova. *Hydrostatische Pumpen und Motoren: Konstruktion und Berechnung*. Vogel Buchverlag, 1993.
- C. Janßen, D. Mierke, and T. Rung. On the Development of an Efficient Numerical Ice Tank for the Simulation of Fluid-Ship-Rigid-Ice Interactions on Graphics Processing Units. *Computers & Fluids*, 155:22–32, 2017.
- H. Jasak. *Error Analysis and Estimation for Finite Volume Method with Applications to Fluid Flow*. PhD thesis, University of London, 1996.

- W. Jones and B. Launder. The Prediction of Laminarization with a Two-Equation Model of Turbulence. *International Journal of Heat and Mass Transfer*, 15:301–314, 1972.
- G. Joseph, R. Zenit, M. Hunt, and A. Rosenwinkel. Particle-Wall Collisions in a Viscous Fluid. *Journal of Fluid Mechanics*, 433:329–346, 2001.
- G. Karypis and V. Kumar. *Metis-Unstructured Graph Partitioning and Sparse Matrix Ordering System, Version 2.0*, 1995.
- H. Kim, H. Marie, and S. Patil. Two-Dimensional CFD Analysis Of A Hydraulic Gear Pump. In *2007 Annual Conference & Exposition*, pages 12.1506.1–18, Honolulu, Hawaii, June 2007. ASEE Conferences. <https://peer.asee.org/1935>.
- A. Koblitz, S. Lovett, N. Nikiforakis, and W. Henshaw. Direct Numerical Simulation of Particulate Flows with an Overset Grid Method. *Journal of Computational Physics*, 343: 414–431, 2017.
- A. Korotkin. *Added Masses of Ship Structures*, volume 88. Springer Science & Business Media, 2008.
- H. Lamb. *Hydrodynamics*. Dover Publications, 6th edition, 1932.
- B. Leonard. A Stable and Accurate Convective Modelling Procedure based on Quadratic Upstream Interpolation. *Computer Methods in Applied Mechanics and Engineering*, 19: 59–98, 1979. doi: 10.1016/0045-7825(79)90034-3.
- F. Lien and M. Leschziner. A General Non-Orthogonal Collocated Finite Volume Algorithm for Turbulent Flow at All Speeds Incorporating Second-Moment Turbulence-Transport Closure, Part 1: Computational Implementation. *Computer Methods in Applied Mechanics and Engineering*, 114:123–148, 1994.
- P.-F. Liu, T.-R. Wu, F. Raichlen, C. Synolakis, and J. Borrero. Runup and Rundown Generated by Three-Dimensional Sliding Masses. *Journal of Fluid Mechanics*, 536: 107–144, 2005.
- R. Löhner. *Applied Computational Fluid Dynamics Techniques: An Introduction based on Finite Element Methods*. John Wiley & Sons, 2008. ISBN 9780470519073 9780470989746. doi: 10.1002/9780470989746.
- H. Lorentz. *Abhandlungen über theoretische Physik*. BG Teubner, 1907.
- X. Luo-Theilen and T. Rung. Computation of Mechanically Coupled Bodies in a Seaway. *Ship Technology Research*, 64:129–143, 2017. doi: 10.1080/09377255.2017.1348654.
- N. Manring and S. Kasaragadda. The Theoretical Flow Ripple of an External Gear Pump. *Journal of Dynamic Systems, Measurement, and Control*, 125(3):396–404, 2003.
- F. Menter. Two-Equation Eddy-Viscosity Turbulence Models for Engineering Applications. *AIAA Journal*, 32(8):1598–1605, 1994.
- F. Menter, M. Kuntz, and R. Langtry. Ten Years of Industrial Experience with the SST Turbulence Model. *Turbulence, Heat and Mass Transfer*, 4:625–632, 2003.

- L. Milne-Thomson. *Theoretical Hydrodynamics*. Macmillan & Co LTD, 1960.
- V. Minorsky. Eine Studie über Schiffskollisionen mit Bezug auf schiffbauliche Schutzmaßnahmen für Kernenergie-Antriebsanlagen. *Schiff und Hafen*, H. 2:163–166, 1960.
- R. Mittal and G. Iaccarino. Immersed Boundary Methods. *Annual Review of Fluid Mechanics*, 37:239–261, 2005.
- J. Mohd-Yusof. Combined Immersed Boudaries/B-splines Methods for Simulations in Complex Geometries, CTR Annual Research Briefs, NASA Ames, 1997.
- S. Muzaferija and M. Perić. Computation of Free-Surface Flows using Interface-Tracking and Interface-Capturing Methods. *Nonlinear Water Wave Interaction*, pages 59–100, 1999.
- K. Nakahashi, F. Togashi, and D. Sharov. Intergrid-Boundary Definition Method for Overset Unstructured Grid Approach. *AIAA Journal*, 38(11):2077–2084, 2000. doi: 10.2514/2.869.
- R. Noack, D. Boger, R. Kunz, and P. Carrica. Suggar++: An Improved General Overset Grid Assembly Capability. *17th AIAA Computational Fluid Dynamics Conference (AIAA 2009-3992)*, 2009.
- E. Pärt-Enander and B. Sjögren. Conservative and Non-Conservative Interpolation Between Overlapping Grids for Finite Volume Solutions of Hyperbolic Problems. *Computers & Fluids*, 23(3):551–574, 1994. doi: 10.1016/0045-7930(94)90019-1.
- C. Peskin. Flow Patterns Around Heart Valves: A Numerical Method. *Journal of Computational Physics*, 10(2):252 – 271, 1972. doi: [http://dx.doi.org/10.1016/0021-9991\(72\)90065-4](http://dx.doi.org/10.1016/0021-9991(72)90065-4).
- L. Qiu, Y. Yu, and R. Fedkiw. On Thin Gaps Between Rigid Bodies Two-Way Coupled to Incompressible Flow. *Journal of Computational Physics*, 292:1–29, 2015.
- C. Rhie and W. Chow. Numerical Study of the Turbulent Flow Past an Airfoil with Trailing Edge Separation. *AIAA Journal*, 21(11):1525–1532, 1983.
- A. Robinson-Mosher, C. Schroeder, and R. Fedkiw. A Symmetric Positive Definite Formulation for Monolithic Fluid Structure Interaction. *Journal of Computational Physics*, 230(4):1547–1566, 2011.
- M. Rostami, A. Ardeshir, G. Ahmadi, and P. Thomas. On the Motion of High-Reynolds Particles in a Quiescent Fluid. *Amirkabir Journal of Science and Technology*, 17(64-B):, 2006.
- S. Rudan and D. Volarić. Fluid Structure Interaction Analysis of a Ship Collision. In *The 7th International Conference on Collision and Grounding of Ships, ICCGS 2016, Korea*, 2016.
- T. Rung. Vorlesungsmanuskript: Statistische Turbulenzmodellierung. *Hermann-Föttinger-Institut für Strömungsmechanik, Technische Universität Berlin*, 2001.

- T. Rung. Vorlesungsmanuskript: Numerische Methoden der Thermofluidodynamik 2 (CFD2). *Institut für Fluidodynamik und Schiffstheorie, Technische Universität Hamburg-Harburg*, 2008.
- T. Rung, K. Wöckner, M. Manzke, J. Brunswig, C. Ulrich, and A. Stück. Challenges and Perspectives for Maritime CFD Applications. *Jahrbuch der Schiffbautechnischen Gesellschaft*, 103:127–39, 2009.
- M. Schäfer, S. Turek, F. Durst, E. Krause, and R. Rannacher. *Benchmark Computations of Laminar Flow around a Cylinder*, pages 547–566. Vieweg+Teubner Verlag, Wiesbaden, 1996. doi: 10.1007/978-3-322-89849-4\_39.
- M. Song, E. Kim, J. Amdahl, J. Ma, and Y. Huang. A Comparative Analysis of the Fluid-Structure Interaction Method and the Constant Added Mass Method for Ice-Structure Collisions. *Marine Structures*, 49:58–75, 2016.
- F. Stern, R. Wilson, and J. Shao. Quantitative V&V of CFD Simulations and Certification of CFD Codes. *International Journal for Numerical Methods in Fluids*, 50(11):1335–1355, 2006.
- G. Stokes. *Transactions of the Cambridge Philosophical Society (Vol. 8)*, chapter On Some Cases of Fluid Motion, pages 105–137. Cambridge University Press, London, 1843.
- W. Strasser. CFD Investigation of Gear Pump Mixing Using Deforming/Agglomerating Mesh. *Journal of Fluids Engineering*, 129(4):476–484, 2007.
- A. Stück. *Adjoint Navier-Stokes Methods for Hydrodynamic Shape Optimisation*. PhD thesis, Technische Universität Hamburg-Harburg, 2011.
- H. Tang, S. Jones, and F. Sotiropoulos. An Overset-Grid Method for 3D Unsteady Incompressible Flows. *Journal of Computational Physics*, 191(2):567–600, 2003. doi: 10.1016/S0021-9991(03)00331-0.
- S. Teoh and H. Ibrahim. Median Filtering Frameworks for Reducing Impulse Noise from Grayscale Digital Images: A Literature Survey. *International Journal of Future Computer and Communication*, 1(4):323–326, 2012.
- Y.-H. Tseng and J. Ferziger. A Ghost-Cell Immersed Boundary Method for Flow in Complex Geometry. *Journal of Computational Physics*, 192(2):593–623, 2003.
- O. Ubbink. *Numerical Prediction of Two Fluid Systems with Sharp Interfaces*. PhD thesis, Imperial College of Science, Technology & Medicine; Department of Mechanical Engineering, 1997.
- A. Vacca and M. Guidetti. Modelling and Experimental Validation of External Spur Gear Machines for Fluid Power Applications. *Simulation Modelling Practice and Theory*, 19(9):2007–2031, 2011.
- B. van Leer. Towards the Ultimate Conservative Difference Scheme: V. A Second-Order Sequel to Godunov’s Method. *Journal of Computational Physics*, 135:229–248, 1997. doi: 10.1006/jcph.1997.5704.

- J. Vande Voorde, J. Vierendeels, and E. Dick. Development of a Laplacian-Based Mesh Generator for ALE Calculations in Rotary Volumetric Pumps and Compressors. *Computer Methods in Applied Mechanics and Engineering*, 193(39):4401–4415, 2004.
- Z. Wang. A Fully Conservative Interface Algorithm for Overlapped Grids. *Journal of Computational Physics*, 122(1):96–106, 1995. doi: 10.1006/jcph.1995.1199.
- F. White. *Fluid Mechanics*. McGraw-Hill, Inc., New York, 3rd edition, 1994. ISBN 0-07-911695-7.
- D. Wilcox. Reassessment of the Scale-Determining Equation for Advanced Turbulence Models. *AIAA Journal*, 26(11):1299–1310, 1988.
- D. Wilcox. *Turbulence Modeling for CFD*, volume 3. DCW Industries, Inc., 2006.
- S. Yakubov, B. Cankurt, M. Abdel-Maksoud, and T. Rung. Hybrid MPI/OpenMP Parallelization of an Euler–Lagrange Approach to Cavitation Modelling. *Computers & Fluids*, 80:365–371, 2013. doi: 10.1016/j.compfluid.2012.01.020.
- S. Yakubov, T. Maquil, and T. Rung. Experience using Pressure-based CFD Methods for Euler–Euler Simulations of Cavitating Flows. *Computers & Fluids*, 111:91–104, 2015. doi: 10.1016/j.compfluid.2015.01.008.
- F.-L. Yang. *Interaction Law for a Collision Between Two Solid Particles in a Viscous Liquid*. PhD thesis, California Institute of Technology, 2006.
- F.-L. Yang. A Formula for the Wall-Amplified Added Mass Coefficient for a Solid Sphere in Normal Approach to a Wall and its Application for Such Motion at Low Reynolds Number. *Physics of Fluids*, 22(12):123303, 2010.
- M. Yazdani and M. Soteriou. A Novel Approach for Modeling the Multiscale Thermo-Fluids of Geared Systems. *International Journal of Heat and Mass Transfer*, 72:517–530, 2014.
- M. Yazdani, M. Soteriou, F. Sun, and Z. Chaudhry. Prediction of the Thermo-Fluids of Gearbox Systems. *International Journal of Heat and Mass Transfer*, 81:337–346, 2015.
- Y. Yoon, B.-H. Park, J. Shim, Y.-O. Han, B.-J. Hong, and S.-H. Yun. Numerical Simulation of Three-Dimensional External Gear Pump using Immersed Solid Method. *Applied Thermal Engineering*, 118:539–550, 2017.
- Z. Yu. *Hydrodynamic and Structural Aspects of Ship Collisions*. PhD thesis, Norwegian University of Science and Technology, 2017.
- J. Zhang, L.-S. Fan, C. Zhu, R. Pfeffer, and D. Qi. Dynamic Behavior of Collision of Elastic Spheres in Viscous Fluids. *Powder Technology*, 106(1):98–109, 1999.



# Lebenslauf

## Persönliche Daten

---

Name Svenja Schubert (geb. Völkner)  
Geburtsdatum 31.08.1988  
Geburtsort Hamburg, Deutschland

## Studium / Schulische Ausbildung

---

04/2011 - 11/2013 **Technische Universität Hamburg-Harburg**  
Master of Science: Schiffbau und Meerestechnik (1,2)  
10/2007 - 05/2011 **Technische Universität Hamburg-Harburg**  
Bachelor of Science: Schiffbau (1,9)  
02/2010 - 09/2013 Stipendium der Studienstiftung des deutschen Volkes  
08/1999 - 07/2007 **Gymnasium Ohmoor, Hamburg**  
Abitur (1,3)

## Berufpraktische Tätigkeiten

---

02/2014 - 07/2018 **Technische Universität Hamburg-Harburg**  
Institut für Fluidodynamik und Schiffstheorie  
Wissenschaftliche Mitarbeiterin  
10/2010 - 03/2012 **Technische Universität Hamburg-Harburg**  
09/2013 - 01/2014 Institut für Fluidodynamik und Schiffstheorie  
Wissenschaftliche Hilfskraft  
10/2012 - 12/2012 **Australian Maritime College, Launceston, Australien**  
Praktikum  
09/2009 - 10/2009 **Fr. Lürssen Werft GmbH & Co. KG, Bremen**  
Fachpraktikum  
07/2007 - 09/2007 **Bremerhavener Dock GmbH, Bremerhaven**  
Grundpraktikum

